ABSTRACT

ROY, TUHIN. Guided Wave Inversion for Arterial Stiffness Estimation. (Under the direction of Dr. Murthy N. Guddati).

Arterial stiffness relates to early onset of multiple cardiovascular diseases. There has been significant research in the past towards estimating the arterial stiffness through models such as Pulse Wave Velocity. More recently, the Acoustic Radiation Force based Shear Wave Elastography (SWE) has become a promising tool to characterize arterial stiffness. In SWE, the artery is excited with an acoustic radiation push and wave propagation along the arterial wall is measured through ultrasound transducer. The resulting SWE data is processed to estimate the arterial stiffness, using various models ranging from immersed plate idealizations that is highly approximate to finite element modeling of fully three-dimensional immersed fluid-filled tube, which is computationally expensive. Irrespective of the employed idealizations, most of the effort is directed towards estimating elastic modulus with limited work on characterizing viscoelasticity. In light of these two observations, this dissertation provides (1) an efficient yet accurate model of wave propagation in arteries, (2) an inversion framework to compute arterial stiffness including viscoelasticity. To achieve these objectives, we proceed with the following steps.

First, we build on a recent work to develop an efficient wave guide model based on semi-analytical finite element method to simulate the wave dispersion. The model considers complex 3D wave propagation, viscoelasticity as well as the interaction between the interstitial and surrounding fluid and the arterial wall. Through carefully combining analytical expansion with locking-free finite element discretization, we illustrate that the dispersion curves are accurately captured in a matter of a few milliseconds on a desktop computer, facilitating practical inversion for arterial stiffness.

In the inversion framework, we first develop a deterministic algorithm to estimate wall modulus by matching multiple modes; unlike the previous efforts that focus on matching a single mode, this is driven by recent observation that the experimentally observed dispersion curve matches with two theoretical dispersion curves in two different frequency ranges. The resulting inversion method is shown to be effective through validation with phantom SWE experiments on rubber tubes. This effort also includes preliminary investigation of inverting for wall thickness, driven by the observation that in vivo thickness measurements may not be accurate. It is observed that deterministic, simultaneous inversion of thickness and modulus is not as effective as inverting

for modulus alone, leading us to explore methods to take advantage of the information on thickness obtained from B mode images.

Towards incorporating the prior information of the thickness in the inverse model, at this time, we developed a Mixed-mode Frequentist approach, which is shown to work reasonably well with phantom experimental data. A Bayesian framework remains to be developed so that the prior information on thickness can be incorporated.

Towards the viscoelastic inversion, realizing that wave dispersion is not sensitive to the viscous terms, we propose a full wave simulation framework which gives the tube responses in space-time for an applied acoustic radiation force. Similar to dispersion analysis, full-wave simulation is built on SAFE approach. It is however different from dispersion analysis as domain of analysis is shifted from frequency-wavenumber to wavenumber-time domain. Notwithstanding this difference, the full wave simulation is also extremely efficient, taking less than 15 seconds with 7 parallel cores on a standard desktop machine for linear viscoelastic damping.

Finally, the above full-wave simulation framework is utilized to estimate the viscoelastic modulus. Given that the excitation force is not known accurately, we propose to use a correlation based objective function. Numerical examples with noise-laden synthetic data illustrate the effectiveness of the proposed approach with full viscoelastic inversion of Voigt-type materials.

Further refinement of the probabilistic framework and additional ex vivo validation of viscoelastic inversion, combined with in vivo illustrations, are expected to lead to a practical and accurate methodology to estimate arterial stiffness that would be amenable to routine clinical use.

Guided Wave Inversion for Arterial Stiffness Estimation

by
Tuhin Roy

A dissertation submitted to the Graduate Faculty of
North Carolina State University
in partial fulfillment of the
requirements for the degree of
Doctor of Philosophy

Civil Engineering

Raleigh, North Carolina
2021

APPROVED BY:

Dr. Murthy N. Guddati Committee Chair	Dr. Ralph Smith
Dr. Marie Muller	Dr. Shamim Rahman

DEDICATION

To my parents.

BIOGRAPHY

Tuhin Roy was born and brought up in Kolkata, India. He earned a bachelor's degree in Civil Engineering from Bengal Engineering and Science University, Shibpur (now known as IIEST, Shibpur), India in 2012. Upon completion of the bachelor's degree, he joined at Indian Institute of Technology (IIT), Kharagpur and obtained a master's in technology degree in Civil Engineering with specialization in Structural Engineering in 2014. He then worked at Indian Register of Shipping, Mumbai as assistant surveyor in Research & Rule Development division for about two years before joining North Carolina State University (NCSU), USA. In addition to the doctoral program in Structural Engineering & Mechanics, he acquired a master's in science degree in Applied Mathematics from NCSU in 2021. This dissertation is a result of the research conducted for the doctoral degree.

ACKNOWLEDGMENTS

I am elated to express my deep gratitude to my advisor, Dr. Murthy Guddati, for guiding me through all the challenges in my research. His valuable guidance has helped me to progress and improve as a researcher over the course of my graduate studies. I would like to specially mention that I have quite enjoyed the brainstorming and constructive discussions with him and several times these academic discussions took place beyond the normal working hours.

I would like to thank Dr. Ralph Smith, Dr. Marie Muller, and Dr. Shamim Rahman for serving as members of my advisory committee. I would like to specially thank Dr. Matthew Urban and Dr. James Greenleaf from Mayo Clinic for conducting and sharing the experimental data with us for validation. I would like to acknowledge the National Science Foundation (Grant CMMI-1635291) and the National Institute of Health (Grant 5R01HL145268 through Mayo Clinic) for supporting my research.

Many thanks to my friends Mohammad Amin Sahafipourfard, Dr. Vivek Samu, and Abdelrahman Elmeliegy for our numerous discussions which have helped me to excel in my research. I would like to thank all my friends at North Carolina State University and elsewhere who have supported me throughout my graduate studies.

I would like to thank Dipshika for her relentless love and patience to support me throughout this journey.

Finally, I would like to thank Almighty for my loving parents. They have been the strength of my life.

TABLE OF CONTENTS

LIST OF TABLES

LIST OF FIGURES

CHAPTER 1: INTRODUCTION

Arterial stiffness is an early indicator (Cheng *et al* 2002, Laurent *et al* 2000, Kingwell and Gatzka 2002, Sutton-Tyrrell *et al* 2005, Dolan *et al* 2006) for many cardio-vascular diseases such as high risk stroke (Laurent *et al* 2000), type II diabetes (COCKCROFT *et al* 2005), myocardial infarction (Hirai *et al* 1989), hypertension (Glasser *et al* 1997, Bussy *et al* 2000, Paini *et al* 2006), end stage renal disease (Guerin *et al* 2001), atherosclerosis development (Oliver and Webb 2003, Vlachopoulos *et al* 2010), and aneurysm (Boutouyrie *et al* 1992). Among several techniques to measure arterial stiffness, the gold standard technique is the use of arterial pulse wave (CARO and CG 1962, Asmar *et al* 1995, Van Bortel *et al* 2012). However, this method experiences several limitations such as inaccurate distance measurement (Mookerjee *et al* 2010), requirement of long distance for time measurement due to low resolution (Bernal *et al* 2011), the unrealistic assumptions on boundary conditions such as isolated in vacuum and inviscid fluid (Couade *et al* 2010), and the linearity assumption of the Euler fluid dynamic equation (Korteweg 1878) in spite of strong nonlinear behavior of pulse wave propagation. To account for the variation of arterial stiffness at different sites, local instantaneous quantitative measurement techniques such as Acoustic Radiation Force (ARF) based imaging has become a popular noninvasive technique to characterize tissue locally. In ARF, ultrasound wave is propagated through the tissue material and the tissue response is analyzed spatially and temporally for tissue characterization locally. There are several ARF methods based on the excitation types (details can be found in (Doherty *et al* 2013)).

Among the imaging techniques, the Shear Wave Elastography (SWE) has become a promising tool since the shear modulus has a wider range than bulk modulus for soft tissues. The SWE technique has been applied in many biomedical examinations of various organs such as kidney (Amador *et al* 2011), prostate (Mitri *et al* 2011), liver (Chen *et al* 2009), cornea (Bernal *et al* 2011, Tanter *et al* 2009, Nguyen *et al* 2012), bladder wall (Nenadic *et al* 2013), myocardium wall (Kanai 2005, Nenadic *et al* 2011, Urban *et al* 2013, Pislaru *et al* 2014, Couade *et al* 2011), Achilles tendon (Brum *et al* 2014, Yeh *et al* 2016, Helfenstein-Didier *et al* 2016), and arterial wall (Zhang *et al* 2005, Bernal *et al* 2011, Couade *et al* 2010). In case of bulk organs, the propagating shear wave does not get affected since the boundaries and interfaces are far from the region of interest. However, in case of organs with confined geometry such as artery, the shear wave becomes guided and dispersive (wave velocity changes at different frequencies). Although the

dispersive nature of wave makes the problem complicated, the different wave mode sensitivities help us to characterize the organs better (Gennisson *et al* 2010, Shcherbakova *et al* 2014).

To reduce the geometric complexities in the wave dispersion analysis for the arteries, an immersed plate model was studied (Couade *et al* 2010, Bernal *et al* 2011, Nguyen *et al* 2011, Widman *et al* 2015, Jang *et al* 2015, Widman *et al* 2016, Maksuti *et al* 2016, Li *et al* 2017a). Later, annuli waveguide (Li *et al* 2017c), hollow tube waveguide (Zhang *et al* 2005, Flamini *et al* 2015), fluid-filled tube (Flamini *et al* 2015, Lin *et al* 2015), and immersed fluid-filled 3D finite element model (Dutta *et al* 2015) are utilized. Recently, an efficient Semi-Analytical Finite Element (SAFE) based immersed and fluid-filled cylindrical waveguide model is utilized in (Astaneh *et al* 2017). Results in (Astaneh *et al* 2017) showed that the forward model can efficiently find the wave dispersions in the cylindrical waveguide model and this wave dispersion can effectively be employed to characterize the arterial wall stiffness. The schematic of the cylindrical waveguide model is presented in Figure 1.1.

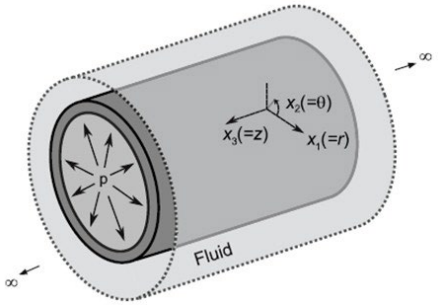

Figure 1.1 Schematic of the considered waveguide model in (Astaneh et al 2017)

While the approach mentioned in (Astaneh *et al* 2017) is efficient, further reduction in computational effort is possible by employing less expensive lower order finite elements. This is addressed in the CHAPTER 2: . To alleviate the volumetric locking of the linear finite elements in the limit of incompressibility, we consider the selective reduced integration scheme. Along with the cylindrical waveguide, we applied this proposed framework for other waveguide model including waveguides with generic cross-sections. The motivation behind considering the generic cross-section is the artery with plaque formed in which we do not have the axis-symmetric cross-section. A schematic is presented here and the formulation details along with the numerical example are available in the CHAPTER 2: .

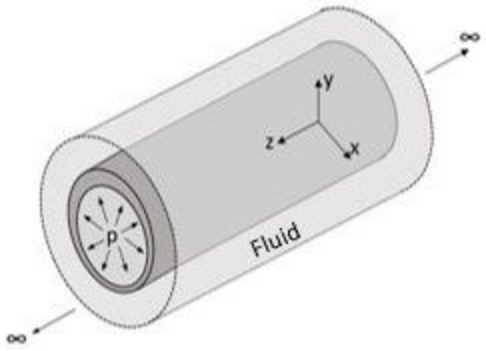

Figure 1.2 Schematic of a waveguide model with non-axis-symmetric cross-section (motivated by the artery with plaque)

In the next step, our goal is to estimate the arterial stiffness with the proposed forward model. Since our objective is towards the early detection of the cardiovascular diseases, we consider axisymmetric cylindrical waveguide model which mimics the human carotid artery (without advanced disease). In most of the earlier models, the primary goal was to back-calculate the artery material modulus (elastic) for characterizing the artery stiffness (Couade *et al* 2010, Bernal *et al* 2011, Nguyen *et al* 2011, Widman *et al* 2015, 2016, Maksuti *et al* 2016, Li *et al* 2017a). However, it has been found that the thickness also significantly contributes towards the artery stiffness (Dutta *et al* 2015) and because of the small length scale associated with it, the thickness measurement using the imaging technique (such as B-mode imaging) is also not well reliable. In the works of (Dutta *et al* 2015), geometries such as thickness, diameter and material modulus are simultaneously inverted, however, the considered group velocity based approach could not ensure the accuracy. The characteristics of artery waveguide which exhibits dispersive wave propagation, can be obtained with better accuracy in phase velocity based approach than that of the group velocity based approach (Maksuti *et al* 2016).

Motivated by this, we attempt to back-calculate both wall thickness and elastic shear modulus with the phase velocity based dispersion curve approach in the CHAPTER 3: . As suggested in the paper (Astaneh *et al* 2017), the multi-modal inversion framework in which we match the measured dispersion curve with the multiple simulated modes is explored. Specifically, we match with the two modes in two different frequency ranges (full details are in CHAPTER 3:). In addition, we improve the quality of the measured dispersion curve through applying windowing on the spatial-temporal data. We have shown that the improvements in the measured dispersion curve and the consideration of the multi-modal setting led to significant improvements

in the inversion results. Figure 1.3 shows the overall outline. For the validation of our proposed approach, we consider rubber tube phantom experiments data which was conducted by Dr. Matthew W. Urban's research group at Mayo Clinic.

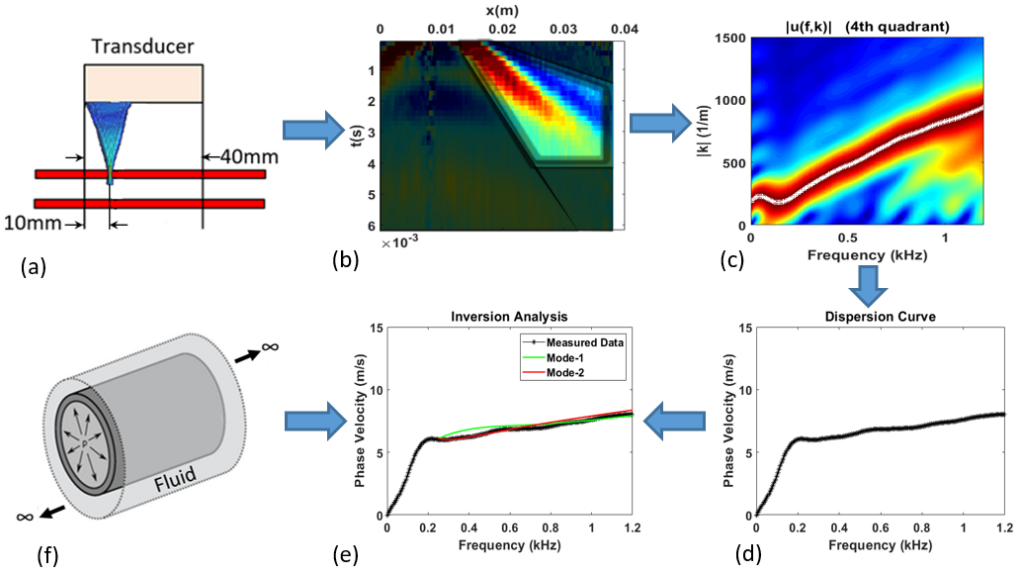

Figure 1.3 (a) Data Acquisition, (b) Data processing, (c) Frequency-wavenumber plot, (d) Measured dispersion curve, (e) Matching of measured and simulated dispersion curves to back-calculate material and geometric properties, (f) Forward model.

As mentioned earlier, the B-mode images are not reliable for thickness due to small scale, however, these images can be considered as the prior information to our inversion model. This further improves the inversion results. Motivated by this, we initiate probabilistic inversion analysis where along with the utilization of the parameter prior information, we incorporate the measurement uncertainty to the analysis. CHAPTER 4: elucidates the considered probabilistic inversion models.

Besides the wall thickness and elastic modulus, the viscoelasticity strongly influences the artery stiffness. As mentioned in (Nguyen *et al* 2011), the phase velocity dispersion curves are not influenced by the viscoelasticity. The same is also observed in our analysis. In addition, we looked at the approaches to obtain the attenuation curve such as AMUSE method (Nenadic *et al* 2017) and Two-point Frequency shift method (Kijanka and Urban 2020). Since the given wall motion data is truncated at some time and in space, we observed artifacts in the Fourier space in both approaches. Therefore, we attempt to compare the wall motion data with the simulated data in

space-time domain. So, we need the simulated response in space-time which we solve in the CHAPTER 5: .

Obtaining the tube wall response in 3D space and time is computationally challenging with the 3D finite elements. Fortunately, in our problem, we have invariant geometry and material properties along the axial and azimuthal directions. This allows us to utilize the Semi-Analytical Finite Element (SAFE) framework resulting in computationally efficient model. In addition, due to the thin walled structure, we proceed with a few initial modes in the modal analysis leading to further improvement in the computation time. We term this simulated response as the full wave response since we incorporate both propagating and evanescent wave modes in the simulation. Figure 1.4 shows the top wall excitation in axial direction and time due to an applied acoustic radiation push (with focus number of 0.75). The simulation details along with the numerical examples are presented in the CHAPTER 5: . To give the preview of the computational efficiencies, the simulation takes less than 15 seconds with 7 parallel cores on a standard desktop machine for the Voigt viscoelastic model.

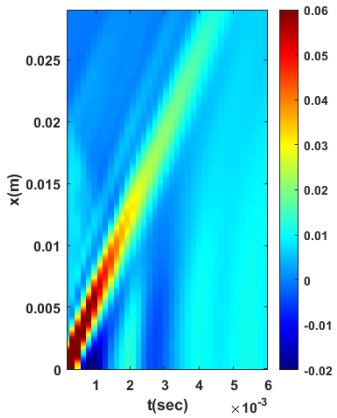

Figure 1.4 Full wave data (top wall response) in axial direction and time.

Finally, we back-calculate the viscoelastic modulus of the arterial (tube) wall through employing the full wave simulation framework along with other approaches. At this point, we verify our proposed approaches with the synthetic data that mimics the tube experiment. The details of these considered approaches are discussed in the CHAPTER 6: , which indicates that reasonable back-calculation of viscoelastic storage and loss moduli may be possible, leading to more informative biomarker than simple elastic modulus.

CHAPTER 2: SHEAR WAVE DISPERSION ANALYSIS OF INCOMPRESSIBLE WAVEGUIDES[1]

ABSTRACT

A suite of methodologies is presented to compute shear wave dispersion in incompressible waveguides encountered in biomedical imaging; plate, tube, and general prismatic waveguides, all immersed in incompressible fluid, are considered in this effort. The developed approaches are based on Semi-Analytical Finite Element Methods in the frequency domain, with a specific focus on the complexities associated with the incompressibility of the solid media as well as the simplification facilitated by the incompressibility of the surrounding fluid. The proposed techniques utilize the traditional idea of selective reduced integration for the solid medium and the more recent idea of Perfectly Matched Discrete Layers for the surrounding fluid. Also utilized is the recently developed Complex-length Finite Element Method for plate-like structures. Several numerical examples are presented to illustrate the practicality and effectiveness of the developed techniques in computing shear wave dispersion in a variety of waveguides.

INTRODUCTION

Plate and pipe like structures can often be characterized through guided wave inversion (Mitra and Gopalakrishnan 2016, Kundu 2003, Rose 2011, Su *et al* 2006, Vaziri Astaneh and Guddati 2016, Foti *et al* 2014, Rose 2014, Willberg *et al* 2015). Guided wave inversion is the process of back-calculating the unknown material and geometric parameters from the observed dispersion of waves propagating along with the plate or pipe walls. An important recent application of guided wave inversion is in biomedical imaging where the objective is to characterize the nearly incompressible soft tissue (Sarvazyan *et al* 2011, 2013, Bernal *et al* 2011, Bercoff *et al* 2004, Nguyen *et al* 2011); (Astaneh *et al* 2017), often surrounded by softer (fluid-like) tissue. Accurate computation of wave dispersion is critical to any guided wave inversion approach, and existing approaches need some modifications to treat incompressible solids, where the only waves that exist are shear waves. The focus of the chapter is to extend some traditional and some recent techniques to efficiently compute the dispersion curves for plate and tube-like structures in vacuum or immersed in an incompressible fluid.

[1] This chapter has been published in J. Acoust. Soc. Am. (2021) 149 972–82

Several analytical formulations (Thomson 1950, Haskell 1953, Knopoff L. 1964, Randall 1967, Lowe 1995, Berliner and Solecki 1996, Sato and Ogiso 2013) are developed for elastic and acousto-elastic waveguides (elastic waveguides immersed in acoustic fluid) but are limited to relatively simple geometries. Computational modeling is often necessary when the geometry is more complicated. Specifically, methods based on finite element discretization can model the waveguides with arbitrary geometry, boundary conditions, and material properties. This approach is first proposed in geotechnical earthquake engineering and geophysics, for both isotropic and anisotropic elasticity, as the *Thin Layer Method* (Kausel and Peek 1982, Tassoulas and Kausel 1983, Kausel 1986). The method is later employed in ultrasonic applications, where it is often referred to as the *Semi-Analytical Finite Element* (SAFE) method (see e.g. (Datta *et al* 1988, Gavrić 1995, Gry 1996, Han *et al* 2001, Hayashi *et al* 2003, Taweel *et al* 2000)). The underlying idea of the thin layer / SAFE method is to utilize analytical formulation in the direction of wave propagation and finite element discretization in the orthogonal direction(s), hence the name Semi-Analytical Finite Element method.

In (Vaziri Astaneh and Guddati 2017b), an efficient SAFE approach is proposed to model the acousto-elastic waveguides mainly for the immersed laminated plates, fluid-filled pipes, and composite waveguides with general cross-sections (similar approaches were developed in less-widely published literature; see (Ghibril 1992, Kokossalakis 2006)). Although this method works well for the compressible waveguides with linear and higher-order finite elements, it fails in the case of the incompressible waveguides with low-order finite elements due to volumetric locking (see e.g. (Hughes 2012)). On the other hand, the incompressibility of the surrounding fluid simplifies the governing equations, leading to more efficient computation of dispersion curves. In this chapter, to perform such computation, we adapt (a) the traditional idea of selective-reduced integration to the SAFE formulation to treat the problem of volumetric locking, (b) the more recent idea of *Perfectly Matched Discrete Layers* (PMDL) for incompressible fluids, and (c) another idea of *Complex-Length Finite Element Method* (CFEM) for plate-like structures (Note that complex-valued element lengths in CFEM are fundamentally different from complex-stretching view point of perfectly matched layers, (see, e.g. (Chew and Weedon 1994), and (Kausel and de Oliveira Barbosa 2012)). Essentially, we propose a suite of techniques that can be utilized to estimate the wave dispersion in waveguides made of soft tissue either in vacuum or immersed in fluid; all these

methods are easily implemented through minor modifications of existing SAFE codes (e.g. (Vaziri Astaneh and Guddati 2017a)).

PROBLEM STATEMENTS

We consider nearly incompressible waveguides (e.g. soft tissues) immersed in an incompressible inviscid fluid. The governing differential equation for the solid domain (Elastodynamic equation) is,

$$\mathbf{L}_\sigma^T \boldsymbol{\sigma} - \rho\omega^2 \mathbf{u} = 0 , \tag{1}$$

where, $\mathbf{u}$ is the displacement vector, $\boldsymbol{\sigma}$ is the stress tensor written in vector form, ρ is the density, and ω is the angular frequency. $\mathbf{L}_\sigma$ is the symmetric gradient operator representing the strain-displacement relation, expressed more precisely in later sections. For the fluid domain, in the limit of incompressibility, the acoustic wave equation becomes the Laplace equation,

$$\nabla^2 p = 0 , \tag{2}$$

where p is the fluid pressure. The conditions at the fluid-solid interface Γ_{FS} are the stress continuity,

$$\boldsymbol{\sigma} \cdot \mathbf{n}_s - p\mathbf{n}_F = 0, \text{ on } \Gamma_{FS} \tag{3}$$

and the continuity of displacement (thus acceleration) in the normal direction:

$$-\omega^2 \mathbf{u} \cdot \mathbf{n}_s - \frac{1}{\rho_F} \frac{\partial p}{\partial \mathbf{n}_F} = 0, \text{ on } \Gamma_{FS} , \tag{4}$$

where $\mathbf{n}_s$ and $\mathbf{n}_F$ are the unit vectors for solid and fluid domain respectively (opposite vectors), and ρ_F is the fluid density. In this chapter, we solve the above governing equations for plates, cylindrical tubes, and general prismatic waveguides. We highlight the important details in the following subsections.

Plate immersed in fluid

Figure 2.1 represents the geometry of the infinite plate in a vacuum. We consider time-harmonic plane-strain deformation in the y-z plane, i.e. $\boldsymbol{u} = \boldsymbol{u}(z, y, \omega)$, which has two components

$\boldsymbol{u} = \{u_z, u_y\}^T$. The symmetric gradient operator is defined as $\mathbf{L}_\sigma = [\partial/\partial z, 0, \partial/\partial y; 0, \partial/\partial y, \partial/\partial z]^T$. The strain is thus $\boldsymbol{\epsilon} = \{\epsilon_{zz}, \epsilon_{yy}, \gamma_{zy}\}^T = \mathbf{L}_\sigma \boldsymbol{u}$. The stress vector $\boldsymbol{\sigma} = \{\sigma_{zz}, \sigma_{yy}, \sigma_{zy}\}^T$ is related to $\boldsymbol{\epsilon}$ through the constitutive relation,

$$\boldsymbol{\sigma} = \mathbf{D}\boldsymbol{\epsilon}\ ,\ \mathbf{D} = \begin{bmatrix} D_{11} & D_{12} & D_{13} \\ D_{21} & D_{22} & D_{23} \\ D_{31} & D_{32} & D_{33} \end{bmatrix} \tag{5}$$

For isotropic materials, the elements of the constitutive matrix $\mathbf{D}$ can be written in terms of the pressure and shear wave velocities $c_{pressure}$, c_{shear} and density ρ:

$$\begin{aligned} D_{11} &= D_{22} = \rho c_{pressure}^2 \\ D_{33} &= \rho c_{shear}^2 \\ D_{12} &= \rho(c_{pressure}^2 - 2c_{shear}^2) \\ D_{13} &= D_{23} = 0 \end{aligned} \tag{6}$$

Given the plane- strain deformation, the fluid pressure is also two-dimensional, i.e. $p = p(z, y, \omega)$. The Laplacian operator is also written in 2D, i.e. $\nabla^2(\cdot) = \partial^2(\cdot)/\partial y^2 + \partial^2(\cdot)/\partial z^2$.

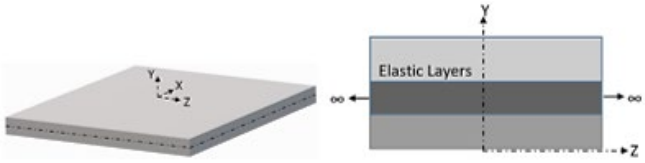

Figure 2.1 Geometry of a layered plate

Cylindrical tube immersed in fluid

Figure *2.2* shows the geometry of the immersed pipe in the fluid. In the solid domain, the primary variable is the displacement $\boldsymbol{u} = \boldsymbol{u}(r, \theta, z, \omega)$, with three components, i.e. $\boldsymbol{u} = \{u_r, u_\theta, u_z\}^T$. The strain is $\boldsymbol{\epsilon} = \mathbf{L}_\epsilon \boldsymbol{u} = \{\epsilon_{rr}, \epsilon_{\theta\theta}, \epsilon_{zz}, \epsilon_{\theta z}, \epsilon_{rz}, \epsilon_{r\theta}\}^T$. The stress is $\boldsymbol{\sigma} = \{\sigma_{rr}, \sigma_{\theta\theta}, \sigma_{zz}, \sigma_{\theta z}, \sigma_{rz}, \sigma_{r\theta}\}^T = \mathbf{D}\boldsymbol{\epsilon}$, where the elements of the constitutive matrix $\mathbf{D}$ are given by (for the isotropic elastic material),

$$
\begin{aligned}
&D_{11} = D_{22} = D_{33} = \rho c_{pressure}^2 \\
&D_{44} = D_{55} = D_{66} = \rho c_{shear}^2 \\
&D_{12} = D_{21} = D_{13} = D_{31} = D_{23} \\
&\quad = D_{32} = \rho(c_{pressure}^2 - 2c_{shear}^2)
\end{aligned} \tag{7}
$$

The 6×3 gradient operators, $\mathbf{L}_\sigma$ and $\mathbf{L}_\epsilon$ are given by,

$$
\begin{aligned}
\mathbf{L}_\sigma(\cdot) &= \mathbf{L}_r r^{-1}\partial(\cdot\times r)/\partial r + \mathbf{L}_\theta r^{-1}\partial(\cdot)/\partial\theta \\
&\quad + \mathbf{L}_z\partial(\cdot)/\partial z - \mathbf{L}_o r^{-1}, \\
\mathbf{L}_\epsilon(\cdot) &= \mathbf{L}_r\partial(\cdot)/\partial r + \mathbf{L}_\theta r^{-1}\partial(\cdot)/\partial\theta \\
&\quad + \mathbf{L}_z\partial(\cdot)/\partial z + \mathbf{L}_o r^{-1}, \\
L_r(1,1) &= L_r(5,3) = L_r(6,2) = 1, \\
L_\theta(2,2) &= L_\theta(4,3) = L_\theta(6,1) = 1, \\
L_z(3,3) &= L_z(4,2) = L_z(5,1) = 1, \\
L_o(2,1) &= -L_o(6,2) = 1
\end{aligned} \tag{8}
$$

We similarly follow cylindrical coordinate representation in the fluid domain, i.e. $p = p(r,\theta,z,\omega)$ and $\nabla^2(\cdot) = r^{-1}\partial(r\partial(\cdot)/\partial r)/\partial r + r^{-2}\partial^2(\cdot)/\partial\theta^2 + \partial^2(\cdot)/\partial z^2$.

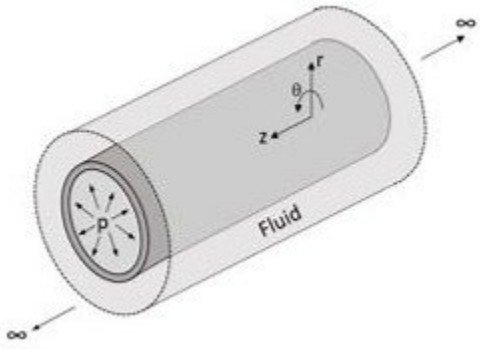

Figure 2.2 Geometry of the immersed tube

Prismatic waveguide immersed in fluid

Figure *2.3* shows the geometry of the general prismatic waveguide immersed in a fluid. The primary variable in the solid domain is the displacement $\boldsymbol{u} = \boldsymbol{u}(x,y,z,\omega)$, with three Cartesian components, i.e. $\boldsymbol{u} = \{u_x, u_y, u_z\}^T$. The strain is $\boldsymbol{\epsilon} = \mathbf{L}_\sigma\boldsymbol{u} = \{\epsilon_{xx}, \epsilon_{yy}, \epsilon_{zz}, \epsilon_{yz}, \epsilon_{xz}, \epsilon_{xy}\}^T$, where,

$$
\begin{aligned}
&\mathbf{L}_\sigma(\cdot) = \mathbf{L}_x \partial(\cdot)/\partial x + \mathbf{L}_y \partial(\cdot)/\partial y + \mathbf{L}_z \partial(\cdot)/\partial z, \\
&L_x(1,1) = L_x(5,3) = L_x(6,2) = 1, \\
&L_y(2,2) = L_y(4,3) = L_y(6,1) = 1, \\
&L_z(3,3) = L_z(4,2) = L_z(5,1) = 1.
\end{aligned} \tag{9}
$$

The stress is $\boldsymbol{\sigma} = \{\sigma_{xx}, \sigma_{yy}, \sigma_{zz}, \sigma_{yz}, \sigma_{xz}, \sigma_{xy}\}^T = \mathbf{D}\epsilon$, where the elements in the constitutive matrix $\mathbf{D}$ for isotropic elastic material are,

$$
\begin{aligned}
&D_{11} = D_{22} = D_{33} = \rho c_{pressure}^2, \\
&D_{44} = D_{55} = D_{66} = \rho c_{shear}^2, \\
&D_{12} = D_{21} = D_{13} = D_{31} = D_{23} \\
&\quad = D_{32} = \rho(c_{pressure}^2 - 2c_{shear}^2).
\end{aligned} \tag{10}
$$

We similarly use 3D Cartesian coordinates for the fluid domain, i.e. $p = p(x, y, z, \omega)$ and $\nabla^2(\cdot) = \partial^2(\cdot)/\partial x^2 + \partial^2(\cdot)/\partial y^2 + \partial^2(\cdot)/\partial z^2$.

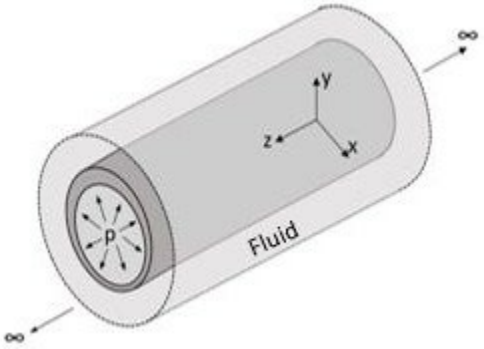

Figure 2.3 Geometry of the immersed prismatic waveguide

SAFE FORMULATION

Semi-Analytical Finite Element (SAFE) formulation considers the analytical solution in one or more directions, while finite element discretization is utilized in the remaining directions. In the problems presented in the previous section, the wave propagation is along the axial direction, therefore, the solution is considered to be in terms of complex exponentials in that direction, while the cross-section is discretized using finite element shape functions or analytical functions or a combination. The details for each of the three problems are presented in the following subsections.

Plate

In the case of a plate, the displacement takes the form, $\boldsymbol{u}(z,y,\omega)=\boldsymbol{u}(y,\omega)e^{ik_z z}$, where k_z is the wavenumber along the wave propagation direction (z). We apply finite element discretization in the *y*-direction for the solid domain. The semi-infinite fluid domain is discretized with the PMDL (see Section 0 for a summary). Assembling the solid and fluid domain with the appropriate interface conditions, we obtain the following Eigenvalue problem,

$$\left(k_z^2\begin{bmatrix}\mathbf{K}_2^S & 0\\ 0 & \kappa\mathbf{K}_2^F\end{bmatrix}+\begin{bmatrix}\mathbf{K}_0^S-\omega^2\mathbf{M}^S & -\kappa\mathbf{C}_{SF}\\ -\omega^2\mathbf{C}_{SF}^T & \kappa\mathbf{K}_0^F\end{bmatrix}\right)\begin{Bmatrix}\boldsymbol{\phi}_S\\ \boldsymbol{\phi}_F\end{Bmatrix}=\mathbf{0} \quad (11)$$

where $\boldsymbol{\phi}_S$ and $\boldsymbol{\phi}_F$ are discretized displacement vectors in solid and fluid domain respectively. Note that manipulation that is standard in the SAFE method is used to simplify the original quadratic eigenvalue problem into an effectively linear eigenvalue problem in *Equation* (11) (see e.g. (Vaziri Astaneh and Guddati 2017b)). Specifically, the degrees of freedom corresponding to the solid domain are transformed as, $\boldsymbol{\phi}_S=\{\boldsymbol{\phi}_{sz}^T, ik_z\boldsymbol{\phi}_{sy}^T\}^T$, where the subscripts represent the direction of the displacement components. $\kappa=\|\mathbf{K}_2^S\|_\infty/\|\mathbf{K}_2^F\|_\infty$ is the scale factor which is used for normalization and thus to improve the conditioning of the system. The solid domain contribution matrices, $\mathbf{K}_2^S,\mathbf{K}_0^S,\mathbf{M}^S$, the fluid domain contribution matrices $\mathbf{K}_2^F,\mathbf{K}_0^F$, and the fluid-structure interaction matrix $\mathbf{C}_{SF}$, are derived from the governing *Equations (1) - (4)*. The reader is referred to, e.g. (Vaziri Astaneh and Guddati 2017b), for further details. Some of the contribution matrices from the solid domain that are relevant to the current work are,

$$\mathbf{K}_2^S=\begin{bmatrix}\mathbf{S}_{zz}^2 & \mathbf{0}\\ -\mathbf{S}_{yz}^1 & \mathbf{S}_{yy}^2\end{bmatrix},\quad \mathbf{S}^2=\int_{y_1}^{y_2}\mathbf{N}_S^T\mathbf{D}_{zz}\mathbf{N}_S dy \qquad (12)$$

Where $\mathbf{N}_S$ is the shape function matrix and $\mathbf{D}_{zz}$ is the constitutive matrix,

$$\mathbf{D}_{zz}=\begin{bmatrix}D_{11} & 0\\ 0 & D_{33}\end{bmatrix}. \qquad (13)$$

$\mathbf{S}_{\alpha\beta}$ is the block of the stiffness matrix representing the resistance in β direction due to displacement in α direction. For the remaining terms including the $\mathbf{K}^{S1}$, the reader is referred to (Vaziri Astaneh and Guddati 2017b). To obtain the dispersion curves, *Equation (11)* is solved for k_z at different frequencies ω, and are plotted against each other. Equivalently, they can be plotted as phase velocity $c_p = \omega/k_z$ as a function of frequency ω.

Cylindrical tube

In the case of a cylindrical tube shown in Figure *2.2*, in addition to the analytical treatment in the axial direction, we consider analytical expansion along the θ direction as well, through Fourier series expansion. The resulting displacement takes the form, $\boldsymbol{u}(r,\theta,z,\omega) = \boldsymbol{u}(r,\omega)e^{im\theta}e^{ik_z^{(m)}z}$, where m is the circumferential Fourier number. Similar to the plate geometry, we use finite element discretization in the radial direction for the solid and interior fluid. PMDL is utilized for the outside fluid (note that, while the derivation of PMDL for straight boundaries is presented in the published literature, it is valid for the Laplace equation in cylindrical geometries (Guddati, 2020). Assembling the final discretized system results in an Eigenvalue problem similar to *Equation (11)*. Here, the degrees of freedom corresponding to the solid medium are written as $\boldsymbol{\phi}_S = \{ik_z\boldsymbol{\phi}_{sr}^T, ik_z\boldsymbol{\phi}_{s\theta}^T, \boldsymbol{\phi}_{sz}^T\}^T$. Like in the plate problem, the solution of the Eigenvalue problem results in the dispersion curves. The details can be found in (Vaziri Astaneh and Guddati 2017b).

Similar to the plate geometry, some of the contribution matrices relevant to the current work are,

$$\mathbf{K}_2^S = \begin{bmatrix} \mathbf{S}_{rr}^2 & 0 & -\mathbf{S}_{rz}^1 \\ 0 & \mathbf{S}_{\theta\theta}^2 & -\mathbf{S}_{\theta z}^1 \\ 0 & 0 & \mathbf{S}_{zz}^2 \end{bmatrix}, \qquad (14)$$

where, $\mathbf{S}_{\alpha\beta}$ is the block of the stiffness matrix representing the resistance in β direction due to displacement in α direction, $\mathbf{S}^2 = \mathbf{K}_{zz}^S$, and

$$\mathbf{S}^1 = \mathbf{K}_{rz}^S - \left(\mathbf{K}_{rz}^S\right)^T - \mathbf{K}_{zo}^S + \left(\mathbf{K}_{zo}^S\right)^T - i\,n\left(\mathbf{K}_{\theta z}^S + \left(\mathbf{K}_{\theta z}^S\right)^T\right)$$

$$\mathbf{K}_{rz}^S = \int_{r_1}^{r_2} \mathbf{B}_S^T \mathbf{D}_{rz} \mathbf{N}_S r dr, \qquad \mathbf{K}_{\theta z}^S = \int_{r_1}^{r_2} \mathbf{N}_S^T r^{-1} \mathbf{D}_{\theta z} \mathbf{N}_S r dr,$$

$$\mathbf{K}_{zz}^S = \int_{r_1}^{r_2} \mathbf{N}_S^T \mathbf{D}_{zz} \mathbf{N}_S r dr, \qquad \mathbf{K}_{zo}^S = \int_{r_1}^{r_2} \mathbf{N}_S^T r^{-1} \mathbf{D}_{zo} \mathbf{N}_S r dr,$$

where $\mathbf{N}_S$ and $\mathbf{B}_S$ are the shape function matrix and the gradient of the shape function matrix respectively. r_1 and r_2 are the inner and outer radii respectively. The constitutive matrices are,

$$\mathbf{D}_{rz} = \begin{bmatrix} 0 & 0 & D_{13} \\ 0 & 0 & 0 \\ D_{55} & 0 & 0 \end{bmatrix}, \quad \mathbf{D}_{\theta z} = \begin{bmatrix} 0 & 0 & 0 \\ 0 & 0 & D_{23} \\ 0 & D_{44} & 0 \end{bmatrix},$$
$$\mathbf{D}_{zz} = \begin{bmatrix} D_{55} & 0 & 0 \\ 0 & D_{44} & 0 \\ 0 & 0 & D_{33} \end{bmatrix}, \quad \mathbf{D}_{zo} = \begin{bmatrix} 0 & 0 & 0 \\ 0 & 0 & 0 \\ D_{32} & 0 & 0 \end{bmatrix}. \tag{15}$$

General prismatic waveguide

For a waveguide with a general cross-section in the x-y plane as shown in Figure *2.3*, waves propagate along the *z*-direction. Thus, using the harmonic form in the z-direction, the displacement vector is written as $\boldsymbol{u}(x, y, z, \omega) = \boldsymbol{u}(x, y, \omega) e^{ik_z z}$. Applying finite-element discretization in the *x*-*y* plane for the interior fluid and solid domains, PMDL for the outside infinite fluid domain, assembling the solid and fluid domain contribution matrices, and incorporating the interface conditions, we get an Eigenvalue problem similar to *Equation (11)*. Similar to the plate and cylinder cases, the solid domain degrees of freedom are manipulated as, $\boldsymbol{\phi}_S = \{ik_z \boldsymbol{\phi}_{sx}^T, ik_z \boldsymbol{\phi}_{sy}^T, \boldsymbol{\phi}_{sz}^T\}^T$. The contribution matrices from the solid domain relevant to the current work are,

$$\mathbf{K}_2^S = \begin{bmatrix} \mathbf{S}_{xx}^2 & 0 & -\mathbf{S}_{xz}^1 \\ 0 & \mathbf{S}_{yy}^2 & -\mathbf{S}_{yz}^1 \\ 0 & 0 & \mathbf{S}_{zz}^2 \end{bmatrix}, \tag{16}$$

where, $\mathbf{S}^2 = \int_\Omega \mathbf{N}_S^T \mathbf{D}_{zz} \mathbf{N}_S d\Omega$ and $\mathbf{S}_{\alpha\beta}$ is the block of the stiffness matrix representing the resistance in β direction due to displacement in α direction. $\mathbf{N}_S$ is the shape function matrix. The constitutive matrix relevant to the incompressibility constraint is,

$$\mathbf{D}_{zz} = \begin{bmatrix} D_{11} & 0 & 0 \\ 0 & D_{66} & 0 \\ 0 & 0 & D_{55} \end{bmatrix} \tag{17}$$

The remaining contribution matrices are defined in (Vaziri Astaneh and Guddati 2017b).

DISCRETIZATION IN THE LIMIT OF INCOMPRESSIBILITY

In the limit of incompressibility, the stiffness associated with the volumetric deformation becomes very large compared to that associated with shear deformation. Linear finite elements with regular integration are known to volumetrically lock the solution, i.e. result in an overly stiff solution that is not convergent to the right solution. To address this problem, selective reduced integration has been successfully used in the context of regular finite element discretization (see, e.g. (Hughes 2012)). We adapt the technique to the dispersion analysis of waveguides using the SAFE method. In this regard, care must be exercised to split the operator that contains the volumetric constraint and under-integrate only that portion. In Section 0, we go through the exercise and provide the details associated with evaluating the contribution matrices discussed in the previous section. In addition, for the plate geometry, the recently-developed CFEM can effectively be employed as it does not get locked in the limit of incompressibility; this method is summarized in Section 0. The exterior incompressible fluid is discretized with PMDL, which is summarized in Section 0. Finally, in Section 0, we propose to modify the normalization factor in *Equation (11)* to better condition the numerical system.

Solid discretization: linear finite elements with selective reduced integration

In the limit of incompressibility, the pressure wave velocity in the solid domain approaches infinity while the shear wave velocity remains finite. Therefore, reduced integration is performed for the contribution matrices associated with the pressure wave velocity. In contrast, full integration is utilized for the part associated with the shear wave velocity. The resulting selective reduced integration is presented below for the three waveguide problems. Naturally, only the solid

domain is considered because the incompressibility of the fluid domain is automatically incorporated through the use of the Laplace equation, which does not have any locking issues.

Plate

Given that the shape function matrix $\mathbf{N}_S$ is linear, only the integrand in $\mathbf{S}^2$ is quadratic (see *Equation (12)*); the rest of the integrands are linear. Thus, reducing the integration from the 2-point Gauss quadrature to the 1-point rule would only alter $\mathbf{S}^2$. To apply selective reduced integration, the integral is divided into two parts:

$$\mathbf{S}^2 = \int_{y_1}^{y_2} \mathbf{N}_S^T \mathbf{D}_{zz}^{(1)} \mathbf{N}_S dy + \int_{y_1}^{y_2} \mathbf{N}_S^T \mathbf{D}_{zz}^{(2)} \mathbf{N}_S dy, \qquad (18)$$

where,

$$\mathbf{D}_{zz}^{(1)} = \begin{bmatrix} D_{11} & 0 \\ 0 & 0 \end{bmatrix}, \qquad \mathbf{D}_{zz}^{(2)} = \begin{bmatrix} 0 & 0 \\ 0 & D_{33} \end{bmatrix}. \qquad (19)$$

Full integration is performed (with 2 Gauss points) for the integral in *Equation (18)* with $\mathbf{D}_{zz}^{(2)}$, and reduced integration is utilized (with 1 Gauss point) for the first integral with $\mathbf{D}_{zz}^{(1)}$, which is associated with the pressure wave velocity.

Cylindrical waveguide

For the cylindrical tube, the contribution matrices $\mathbf{K}_{rz}^S, \mathbf{K}_{\theta z}^S, \mathbf{K}_{zz}^S, \mathbf{K}_{zo}^S$ contain quadratic integrands and are affected by reducing the quadrature from 2-point scheme to 1-point scheme. To apply the selective reduced integration for these integrals, like the plate waveguide, each matrix is separated into shear and pressure wave contributions:

$$\begin{aligned}
\mathbf{K}_{rz}^S &= \int_{r_1}^{r_2} \mathbf{B}_S^T \mathbf{D}_{rz}^{(1)} \mathbf{N}_S r dr + \int_{r_1}^{r_2} \mathbf{B}_S^T \mathbf{D}_{rz}^{(2)} \mathbf{N}_S r dr, \\
\mathbf{K}_{\theta z}^S &= \int_{r_1}^{r_2} \mathbf{N}_S^T r^{-1} \mathbf{D}_{\theta z}^{(1)} \mathbf{N}_S r dr + \int_{r_1}^{r_2} \mathbf{N}_S^T r^{-1} \mathbf{D}_{\theta z}^{(2)} \mathbf{N}_S r dr, \\
\mathbf{K}_{zz}^S &= \int_{r_1}^{r_2} \mathbf{N}_S^T \mathbf{D}_{zz}^{(1)} \mathbf{N}_S r dr + \int_{r_1}^{r_2} \mathbf{N}_S^T \mathbf{D}_{zz}^{(2)} \mathbf{N}_S r dr, \\
\mathbf{K}_{zo}^S &= \int_{r_1}^{r_2} \mathbf{N}_S^T r^{-1} \mathbf{D}_{zo}^{(1)} \mathbf{N}_S r dr + \int_{r_1}^{r_2} \mathbf{N}_S^T r^{-1} \mathbf{D}_{zo}^{(2)} \mathbf{N}_S r dr,
\end{aligned} \qquad (20)$$

Where, the constitutive matrices are,

$$\mathbf{D}_{rz}^{(1)}=\begin{bmatrix}0&0&D_{13}\\0&0&0\\0&0&0\end{bmatrix},\quad \mathbf{D}_{\theta z}^{(1)}=\begin{bmatrix}0&0&0\\0&0&D_{23}\\0&0&0\end{bmatrix},\quad \mathbf{D}_{zz}^{(1)}=\begin{bmatrix}0&0&0\\0&0&0\\0&0&D_{33}\end{bmatrix},\quad \mathbf{D}_{zo}^{(1)}=\begin{bmatrix}0&0&0\\0&0&0\\D_{32}&0&0\end{bmatrix},$$
$$\mathbf{D}_{rz}^{(2)}=\begin{bmatrix}0&0&0\\0&0&0\\D_{55}&0&0\end{bmatrix},\quad \mathbf{D}_{\theta z}^{(2)}=\begin{bmatrix}0&0&0\\0&0&0\\0&D_{44}&0\end{bmatrix},\quad \mathbf{D}_{zz}^{(2)}=\begin{bmatrix}D_{55}&0&0\\0&D_{44}&0\\0&0&0\end{bmatrix},\quad \mathbf{D}_{zo}^{(2)}=\mathbf{0} \tag{21}$$

Reduced integration is used for the integrals associated with pressure wave velocity (with superscript 1), while full integration is utilized for those associated with shear wave velocity (with superscript 2).

Prismatic waveguide

Similar to the plate and tube waveguides, for general prismatic waveguides, first the solid domain contribution matrix that has quadratic and higher-order polynomials inside the integral is identified and decomposed into two parts corresponding to the pressure and shear wave velocities:

$$\mathbf{S}^2=\int_\Omega \mathbf{N}_S^T\mathbf{D}_{zz}^{(1)}\mathbf{N}_S d\Omega+\int_\Omega \mathbf{N}_S^T\mathbf{D}_{zz}^{(2)}\mathbf{N}_S d\Omega\ , \tag{22}$$

where,

$$\mathbf{D}_{zz}^{(1)}=\begin{bmatrix}D_{11}&0&0\\0&0&0\\0&0&0\end{bmatrix},\quad \mathbf{D}_{zz}^{(2)}=\begin{bmatrix}0&0&0\\0&D_{66}&0\\0&0&D_{55}\end{bmatrix} \tag{23}$$

Reduced integration (1x1 Gauss quadrature) is used for the first integral while full integration (2x2 Gauss quadrature) is utilized for the second integral.

Alternative discretization for plate: Complex Length Finite Element Method (CFEM)

CFEM utilizes linear finite elements with midpoint integration and bends the finite element mesh into the complex plane in a special way, to achieve high accuracy at the edges of the mesh (Guddati *et al* 2016). Specifically, CFEM is derived by linking midpoint integrated linear finite elements with Padé approximants, which has the appealing property of exponential convergence, i.e. the error in the solution on the mesh boundaries exponentially converge to zero with an increasing number of CFEM elements (this is in contrast with algebraic convergence of regular polynomial based finite elements). CFEM is inherently a one-dimensional method designed for PDE with constant coefficients, and thus applicable to the plate problem, where each homogeneous

layer is discretized in the y-direction using CFEM mesh. Figure *2.4* shows the example of CFEM mesh for a 3-layer plate. The details of CFEM can be found in (Guddati *et al* 2016) and application to generally layered waveguides can be found in (Vaziri Astaneh and Guddati 2016). Due to its link to spectral FEM (see (Guddati *et al* 2016)), unlike regular FEM, CFEM does not suffer issues with volumetric locking and can thus be utilized for incompressible plates without any modification. This is evident from Numerical Examples section.

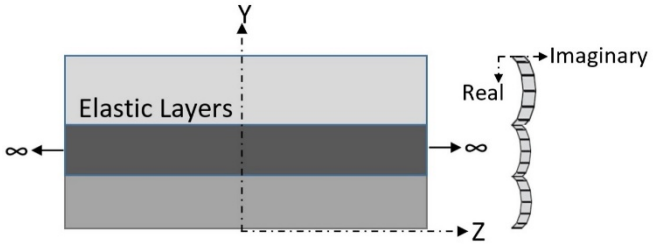

Figure 2.4 CFEM Discretization

Exterior fluid discretization: Perfectly Matched Discrete Layers (PMDL)

Perfectly Matched Discrete Layers (PMDL) is essentially a simple yet highly effective discretization of the well-known *Perfectly Matched Layers* (PML) to model unbounded domains to mitigate reflections from artificial truncation in wave propagation problems. It is shown in (Guddati and Lim 2006, Guddati *et al* 2008) that if PML is discretized using linear finite elements with midpoint integration, the discretization error that pollutes the effectiveness of PML is completely eliminated. The only error thus is the truncation error, which can be derived as,

$$R = \Pi_{j=1}^{n_p} \left| \frac{k_y - 2i/L_j}{k_y + 2i/L_j} \right|^2, \qquad (24)$$

where n_p is the number of PMDL elements, k_y is the wavenumber in the direction perpendicular to the computational boundary, L_j is j^{th} PMDL element length, n_p is the number of PMDL layers, and $i = \sqrt{-1}$. PMDL was originally developed for propagating waves where k_y is real and L_j is chosen to be imaginary or complex. In the present setting, however, since the waves are propagating in the z-direction, given that the Laplace equation is applicable for the (incompressible) fluid, the waves are completely evanescent in the y-direction. Given this

observation, we adapt the techniques in (Guddati *et al* 2008) and chose L_j to be real, and geometrically graded (see (Savadatti and Guddati 2010a)). Specifically, the lengths are chosen as $L_j = L_1 \alpha^{j-1}$, where α is the geometric ratio. A typical value of $\alpha = 2.5$ and L_1 to be the interior element size, with 9 elements are adopted here, which are shown to result in satisfactory results with engineering accuracy (Savadatti and Guddati 2010a). Further details on PMDL can be found in (Kausel 2018, Guddati and Lim 2006, Guddati *et al* 2008).

The idea of combining PML with SAFE formulations appears to be first developed in (Barbosa *et al* 2012), where the focus was on layered elastic systems resting on half-space. In (Vaziri Astaneh and Guddati 2017b), we had utilized PMDL for compressible fluids, and focus on application to incompressible fluids in the current work. Since PMDL is based on one-dimensional mesh extension, it is immediately applicable to the plate problem where the mesh extension is performed above and below the solid plate, in positive and negative y directions respectively. While PMDL is not applicable for wave propagation problems in cylindrical coordinate systems, it is applicable for Laplace and elastostatic equations (Guddati 2020). Fortunately, since the Laplace equation governs the exterior incompressible fluid, the same 1D mesh extension strategy is valid and utilized for the case of a cylindrical tube. Finally, for the general prismatic waveguides, the solid domain can be surrounded by a fluid domain to create a rectangular or a polygonal computational boundary and tensor-product PMDL discretizations can be utilized, where the PMDL consists of a product of edge and corner PMDLs (see Guddati and Lim, 2006; Savadatti and Guddati, 2010b). An example of such mesh is shown in Figure *2.11* and Figure *2.13*). A more elaborate discussion can be found in (Vaziri Astaneh and Guddati 2017b).

Interior fluid discretization

The fluid inside the cylindrical tube is discretized with linear finite elements, while the fluid inside the general prismatic waveguides is discretized with bilinear isoparametric finite elements. There is no complexity associated with incompressibility; in fact, fluid incompressibility leads to the Laplace equation, which is simpler to discretize than the acoustic wave equation for a compressible fluid.

Normalization in the limit of incompressibility

The contribution matrices from the solid and fluid domain have different orders of magnitudes, leading to ill-conditioning of the resulting coupled Eigenvalue problem. To resolve this issue, the normalization factor is utilized in the final Eigenvalue problem, as shown in the

Equation (11). In (Vaziri Astaneh and Guddati 2017b), this factor was calculated using the infinity norm of the contribution matrices from the solid and fluid domain. However, the infinity norm associated with the solid domain approaches infinity in the limit of incompressibility. To address this issue, we have updated this factor by incorporating the Poisson's ratio:

$$\kappa = (1-2\nu)\frac{\| \boldsymbol{K}_2^S \|_\infty}{\| \boldsymbol{K}_2^F \|_\infty} \tag{25}$$

In the limit of incompressibility, the norm of the solid stiffness approaches infinity, while the factor $(1-2\nu)$ approaches zero, but the normalization factor, which is the product, remains bounded. We have confirmed the effectiveness of the above normalization factor through numerical experiments.

NUMERICAL EXAMPLES

Plate in vacuum

In this section, the proposed approach is verified for the plate model. The model parameters are shear wave velocity $c_s = 10$ m/s, pressure wave velocity $c_p = 1{,}540$ m/s, density $\rho = 1{,}100$ kg/m^3, and plate thickness $h = 5$ mm. The reference solution is obtained using high-order (9-noded) finite elements, which is confirmed to be very accurate; Through convergence analysis, we observe the relative L_2 error of below 1.e-5 with 10 elements. The L_2 error is defined here as the L_2 norm of the difference between the results with two consecutive mesh refinements. We note here that an analytical reference solution could be obtained using the methodology presented in e.g. (Kumar and Naskar 2017), but is not considered here given that it is peripheral to the current effort.

Figure *2.5* presents the results from 75-element linear finite element mesh with full integration, which are clearly different from the reference solution; this difference is attributed to the volumetric locking. When the integration is modified to selective reduced integration, the results closely match the reference solution (see Figure *2.5*). Similarly, when CFEM is utilized with just nine elements, the results closely match the reference solution, also shown in Figure *2.5*. For a quantitative convergence analysis, the relative error in the dispersion relation is plotted in Figure *2.6* as a function of number of degrees of freedom for all three discretization approaches. The figure illustrates (a) the exponential convergence of CFEM, (b) acceptable algebraic convergence of linear finite elements with selective reduced integration, and (c) poor convergence of linear elements with full integration. Here, the error in dispersion relation is the L_2 norm of the

difference from the reference dispersion curve. Naturally, for the plate problems, CFEM is advocated, and when not applicable, e.g. for nonhomogeneous material properties, linear finite elements with selective reduced integration is advocated.

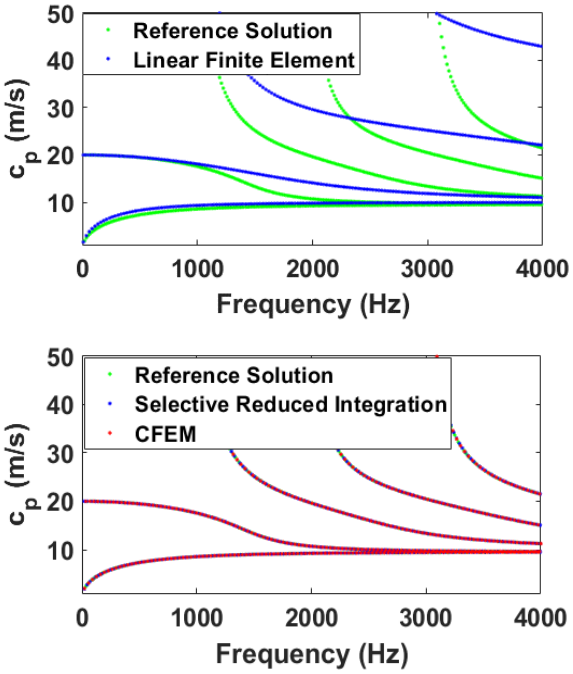

Figure 2.5. Dispersion curves for the plate in vacuum: (top) linear finite elements with full integration; (bottom) linear finite elements with selective reduced integration and CFEM

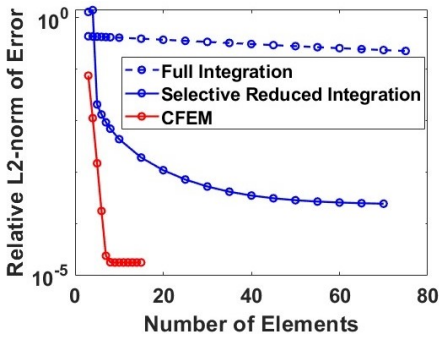

Figure 2.6. Convergence study for computing dispersion curves of the plate in a vacuum

Plate immersed in fluid

The plate considered in the previous section is now surrounded by an incompressible fluid with a density of 1,060 kg/m^3. The fluid is simulated with a geometrically graded mesh of nine PMDL elements, starting with an element length of 1.e-4 m and a gradation factor of 2.5. Figure *2.7* shows the dispersion curves using the same meshes used in the previous section for the solid

domain. This clearly illustrates the effectiveness of CFEM and linear elements with selective reduced integration.

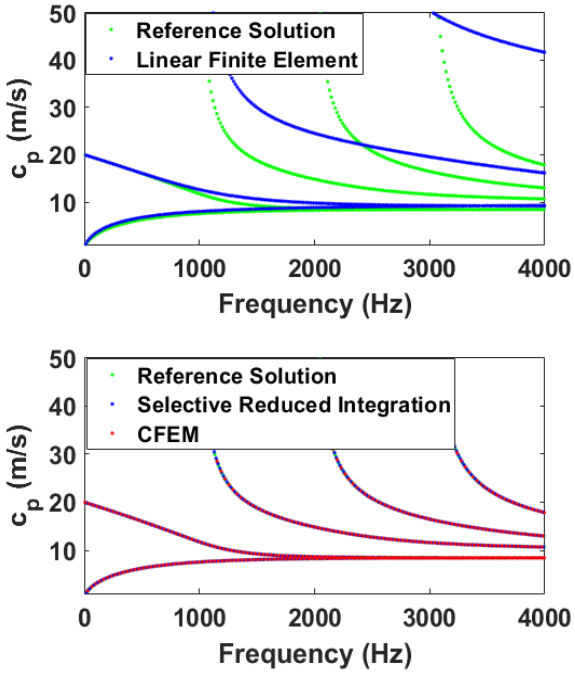

Figure 2.7. Dispersion curves for the immersed plate: linear finite elements with (top) full integration and (bottom) selective reduced integration & CFEM

Cylindrical tube in vacuum

Similar to the plate model, we obtain the reference solution using 10 high-order, 9-noded finite elements. The model parameters are inner radius $r_i = 3$ mm, wall thickness $h = 1$ mm, the shear wave velocity $c_s = 10$ m/s, and the material density $\rho = 1{,}100$ kg/m^3. Figure *2.8* compares the reference solution with the results from 75 linear finite elements with full integration, which indicates a large error. Once selective reduced integration is used, the results from linear finite elements match well with the reference solution, also as shown in Figure *2.8*.

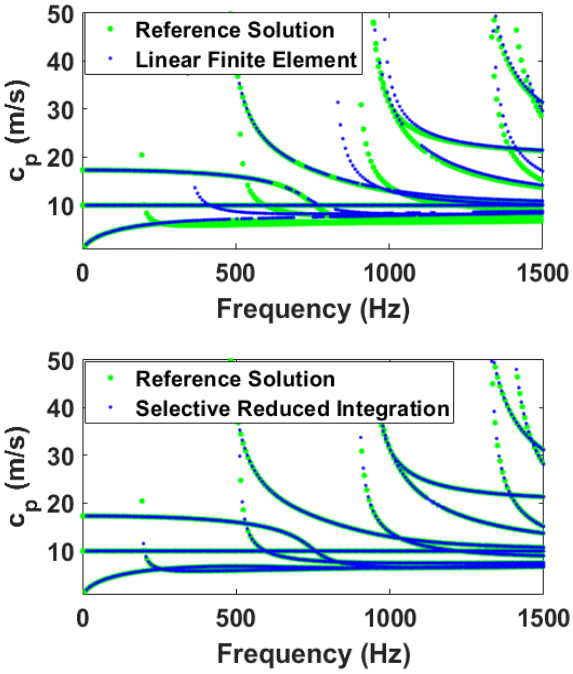

Figure 2.8. Dispersion curves for cylindrical tube: (top) linear finite elements with full integration; (bottom) linear finite elements with selective reduced integration

Cylindrical tube immersed in fluid

The cylindrical tube considered above, is now filled with and immersed in an incompressible fluid with a density of 1,060 kg/m^3. The interior fluid region is discretized with 10 elements, with the same order and length employed to discretize the solid layer. To model the (infinite) surrounding fluid, a geometrically graded mesh of nine PMDL elements is used, with the first element length of 1.e-4 m and a gradation factor of 2.5. The results from linear finite elements are compared with the reference solution in Figure *2.9*, which shows a good correlation with the reference solution. In the case of linear finite elements, selective reduced integration is performed only for the solid domain, and regular (full) integration is used for the interior fluid domain.

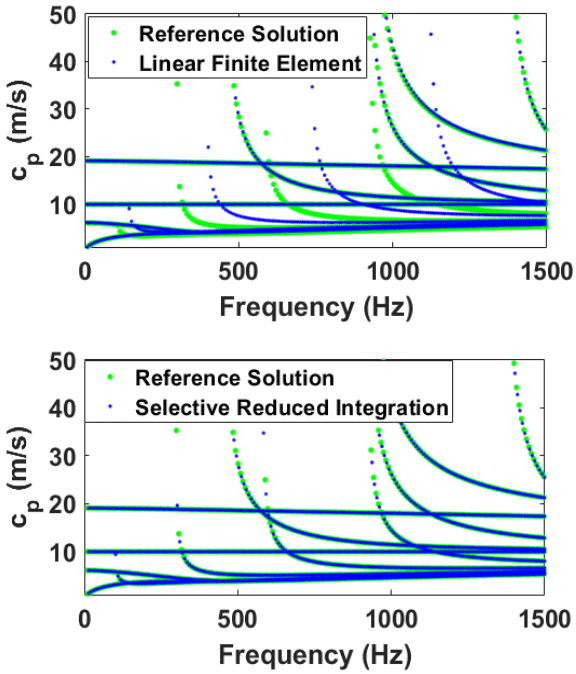

Figure 2.9. Dispersion curves for fluid-filled pipe immersed in a fluid (top) with linear FE (Full Integration) (bottom) with linear FE (Selective Reduced Integration)

Prismatic waveguide immersed in fluid

Before performing verification for general prismatic waveguides, we verify our proposed approach with the axisymmetric cylindrical waveguide, but with 2D finite element discretization of the cross-section. The reason to choose this geometry is the availability of the reference solution from the previous section. 2D meshes of the cross-section with 4- and 8-node isoparametric elements are created using ANSYS (Ansys® Academic *Research Mechanical, Release 16*.1) and are shown in Figure *2.10* (for tube in a vacuum) and Figure *2.11* (for the immersed tube). The material and geometric properties are chosen to be the same as the previous example. For PMDL around the fluid region, we consider four elements with the first element length of 1.e-2 m and the gradation factor of 16. The material properties of the surrounding fluid are the same as the inside fluid. First, the results for the tube in vacuum are presented in Figure *2.12*, followed by the results for the immersed tube in Figure *2.12*. In both Q4 and Q8, we utilize selective reduced integration for the solid domain, full integration for the interior fluid, and the midpoint integration for the PMDL elements surrounding the truncated fluid domain. Figure *2.12* indicates a good correlation between the results, especially for the lower modes. Some differences are observed for higher modes, which can be reduced by mesh refinement.

Finally, we consider a prismatic waveguide with an eccentric annular cross-section with the centers of the inside and outside circles offset by 0.5e-3 m, as shown in Figure *2.13*. All other geometric and material properties are the same as those in the axisymmetric model. The dispersion curves from the 4- and 8-noded finite element discretizations are shown in Figure *2.14*. Similar to the axisymmetric tube, good agreement is observed for lower modes, while the differences in higher modes are expected to be reduced through mesh refinement.

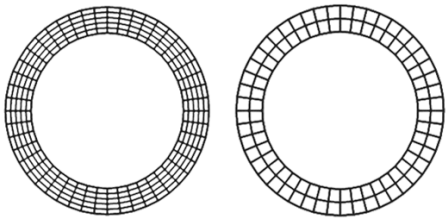

Figure 2.10. 2D discretization of the cylindrical tube

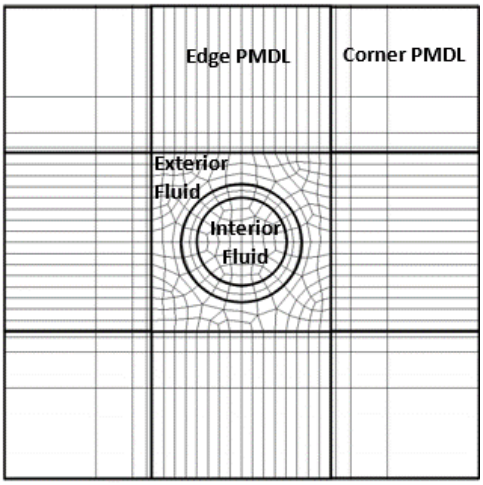

Figure 2.11 Axis-symmetric fluid-filled 2D geometry immersed in a fluid

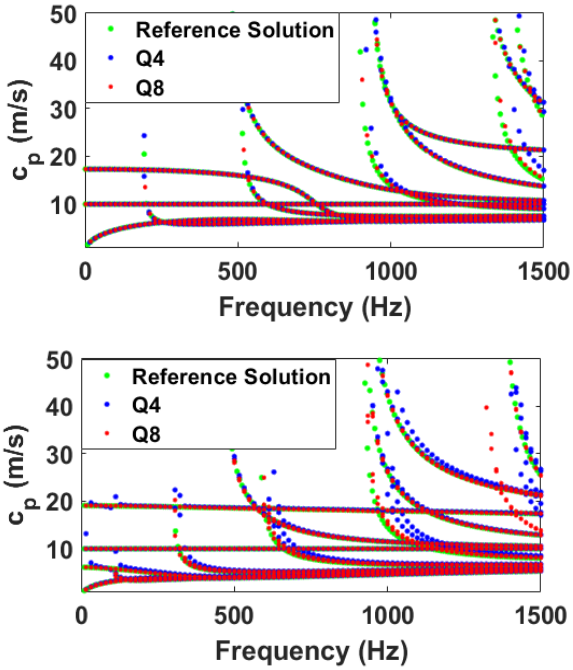

Figure 2.12 Dispersion curves from the 2D discretization of a cylindrical tube: (top) in vacuum; (bottom) immersed in fluid

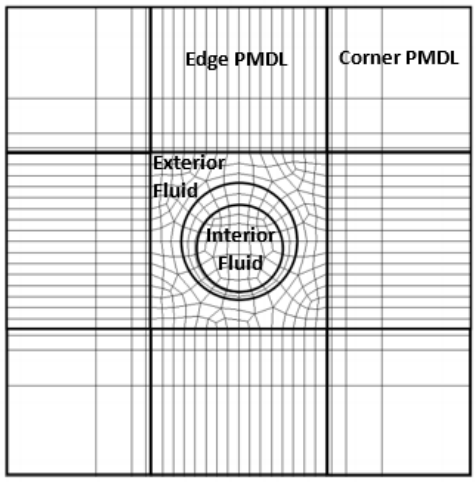

Figure 2.13 2D discretization of fluid-filled non-cylindrical tube

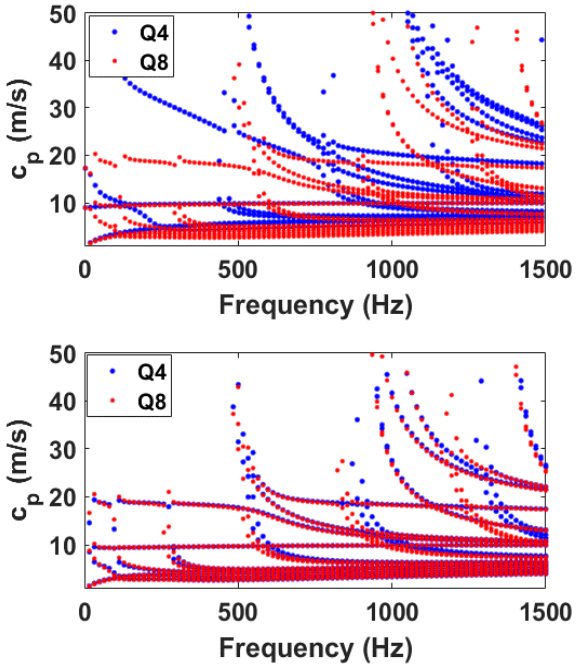

Figure 2.14 Dispersion curve (top) with full integration (with Q4 and Q8) and (bottom) with selective reduced integration (with Q4 and Q8)

CONCLUSIONS

Using *Semi-Analytical Finite Element* (SAFE) methodology, we developed a suite of practical techniques for computing dispersion curves for incompressible elastic waveguides either in vacuum or immersed in an incompressible fluid. Specifically, three different geometries are considered: plate, cylindrical tube, and general prismatic waveguide. We propose the *Complex-Length Finite Element Method* (CFEM) for layered plates, and linear finite elements with selective reduced integration for plates with material properties that are not piecewise constant. For cylindrical waveguides, we utilize linear finite elements with selective reduced integration combined with *Perfectly Matched Discrete Layers* (PMDL) for the exterior fluid. For prismatic waveguides with general cross-section, 4- or 8-node finite element mesh with selective reduced integration works well; the interior fluid is discretized with regular finite elements and the outer fluid is discretized with PMDL. Numerical examples illustrate the effectiveness of the proposed approaches. All the methods can be implemented easily through minor modifications in the existing SAFE codes (see, e.g. (Vaziri Astaneh and Guddati 2017a)).

CHAPTER 3: MULTIMODAL GUIDED WAVE INVERSION FOR ARTERIAL STIFFNESS: METHODOLOGY AND VALIDATION IN PHANTOMS[2]

ABSTRACT

Arterial stiffness is an important biomarker for many cardiovascular diseases. Shear wave elastography is a recent technique aimed at estimating local arterial stiffness using guided wave inversion (GWI), i.e. matching the computed and measured wave dispersion. This chapter develops and validates a new GWI approach by synthesizing various recent observations and algorithms: (a) refinements to signal processing to obtain more accurate experimental dispersion curves; (b) an efficient forward model to compute theoretical dispersion curves for immersed, incompressible cylindrical waveguides; (c) an optimization framework based on the recent observation that the measured dispersion curve is multimodal, i.e. it matches for not one but two different wave modes in two different frequency ranges. The resulting inversion approach is validated using extensive experimental data from rubber tube phantoms, not only for modulus estimation but also to simultaneously estimate modulus and wall thickness. The observations indicate that the modulus estimates are best performed with the information on wall thickness. The approach, which takes less than half a minute to run, is shown to be accurate, with the modulus estimated with less than 4% error for 70% of the experiments.

INTRODUCTION

Arterial stiffness is a well-known biomarker of early cardiovascular diseases (Palombo and Kozakova 2016, Chirinos *et al* 2019, Sun 2015). The pulse wave velocity (PWV) is a widely used biomarker for arterial stiffness (Laurent *et al* 2006, Chirinos *et al* 2019, McGarry *et al* 2016, Segers *et al* 2020). The PWV is currently measured by evaluating the time delay between the pressure waveforms measured using tonometry at the carotid and femoral arteries and using an estimated travel distance (Kullo and Malik 2007). However, given the approximate and average nature of the resulting PWV estimation, there is a concerted effort to estimate localized arterial stiffness, e.g. that of the carotid artery. This has been done using measurements of vessel distension with high frame rate ultrasound imaging (Luo *et al* 2009, Vappou *et al* 2010, Luo *et al* 2012, Parameswaran *et al* 2019, Marais *et al* 2019).

[2] This chapter has been published in Phys. Med. Biol. (2021) 66 115020

Shear wave elastography (SWE) of the arterial stiffness using acoustic radiation force (ARF) has shown to be a promising tool to estimate the stiffness of carotid artery (Couade *et al* 2010, Bernal *et al* 2011, Pruijssen *et al* 2020). The main idea of arterial SWE is to use ARF excitation to generate waves propagating within the arterial walls, and use the characteristics of the propagating waves to estimate the arterial stiffness.

The main approach to estimate arterial stiffness from the measured response is through inversion, i.e. iteratively changing the properties of a model to minimize the difference between simulated and measured dispersion curves that represent the variation of phase velocity as a function of frequency. These curves reflect how the time-domain waveform distorts as it propagates along the artery. The measured dispersion curve is obtained from processing the wall motion data acquired using high frame rate ultrasound imaging. The simulated dispersion curve is obtained through a forward model, i.e. analytical or computational model that can predict the wave dispersion given the arterial material and geometric properties.

Various forward models have been developed to compute wave dispersion in arteries. Early models were focused on the simplification of geometric complexities leading to analytical solutions, with later models focused on both analytical and computational techniques. Some of the existing analytical models include, plate (Couade *et al* 2010, Bernal *et al* 2011, Nguyen *et al* 2011, Widman *et al* 2015, Jang *et al* 2015, Widman *et al* 2016, Maksuti *et al* 2016, Li *et al* 2017a), hollow tube (Zhang *et al* 2005, Flamini *et al* 2015), and fluid-filled tube (Flamini *et al* 2015, Lin *et al* 2015). A more detailed three-dimensional finite element model is utilized in (Dutta *et al* 2015). In (Astaneh *et al* 2017) and (Roy and Guddati 2021), a waveguide model based on semi-analytical finite element (SAFE) methods was developed to capture the fully three-dimensional wave propagation in a fluid-filled immersed tube, but with a significantly reduced computational cost without sacrificing accuracy. Through a validation exercise in (Astaneh *et al* 2017), we found that the experimental dispersion curve matches not with a single simulated curve, but multiple curves depending on the frequency range. The goal of this chapter is to build on this observation and develop and validate inversion approaches to estimate the arterial modulus.

Most of the existing work focused on estimating the shear modulus to characterize the arterial stiffness (Couade *et al* 2010, Bernal *et al* 2011, Nguyen *et al* 2011, Widman *et al* 2015, 2016, Maksuti *et al* 2016, Li *et al* 2017a). However, it is known that thickness also significantly contributes towards artery stiffness estimation (Maksuti *et al* 2017, Astaneh *et al* 2017, Dutta *et al*

2015) . Because it is small, the thickness, which is often measured using ultrasound B-mode images, may not always be accurate. Thus, if possible, it would be desirable to estimate the thickness in addition to modulus, from the wave dispersion properties. Exploring this possibility is a secondary goal of the current study.

The outline of the chapter is as follows. After summarizing the basic idea of shear wave elastography for arteries, we describe the data acquisition and processing to obtain the experimental dispersion curve, which includes a summary of recent signal processing refinements. We then focus on the forward model to compute the simulated dispersion curves. In the following section, we discuss the necessary details related to inversion, i.e. parametrization, objective function, and optimization algorithms. The validation study is then presented followed by concluding remarks.

SHEAR WAVE ELASTOGRAPHY OF ARTERIES

Given that arterial wall modulus is much higher than the surrounding tissue, a high-frequency pulse from the acoustic radiation force generates waves that are guided along the arterial wall. The dispersion characteristics of the guided waves are used to estimate the arterial modulus and thus the stiffness (Couade *et al* 2010, Bernal *et al* 2011). The schematic of the methodology for phantom experiments is shown in Figure 3.1. The procedure involves two major steps:

(1) Data Acquisition and Signal Processing: The shear waves are generated inside the tube and the resulting wave propagation response is measured on the top surface along the axis of the tube as shown in Figure 3.1(a). The recorded spatiotemporal response (Figure 3.1(b)) is transformed into the frequency-wavenumber (*f-k*) domain through a two-dimensional Fast Fourier Transformation (2D FFT), as shown in Figure 3.1(c). The peaks in the *f-k* data are identified and plotted as a dispersion curve, i.e. plot of phase velocity $\left(c_p = 2\pi f / k\right)$ vs. f (Figure 3.1(d)).

(2) Inversion through Optimization: The last major step is to back-calculate the properties of the tube through matching the measured dispersion curve with the simulated dispersion curve by iteratively changing the properties of the tube (Figure 3.1(e)). The simulated dispersion curves are calculated using an analytical or computational forward model (Figure 3.1(f)). The back-calculation (inversion) is performed through optimization, i.e. minimizing the difference between the measured and simulated dispersion curves.

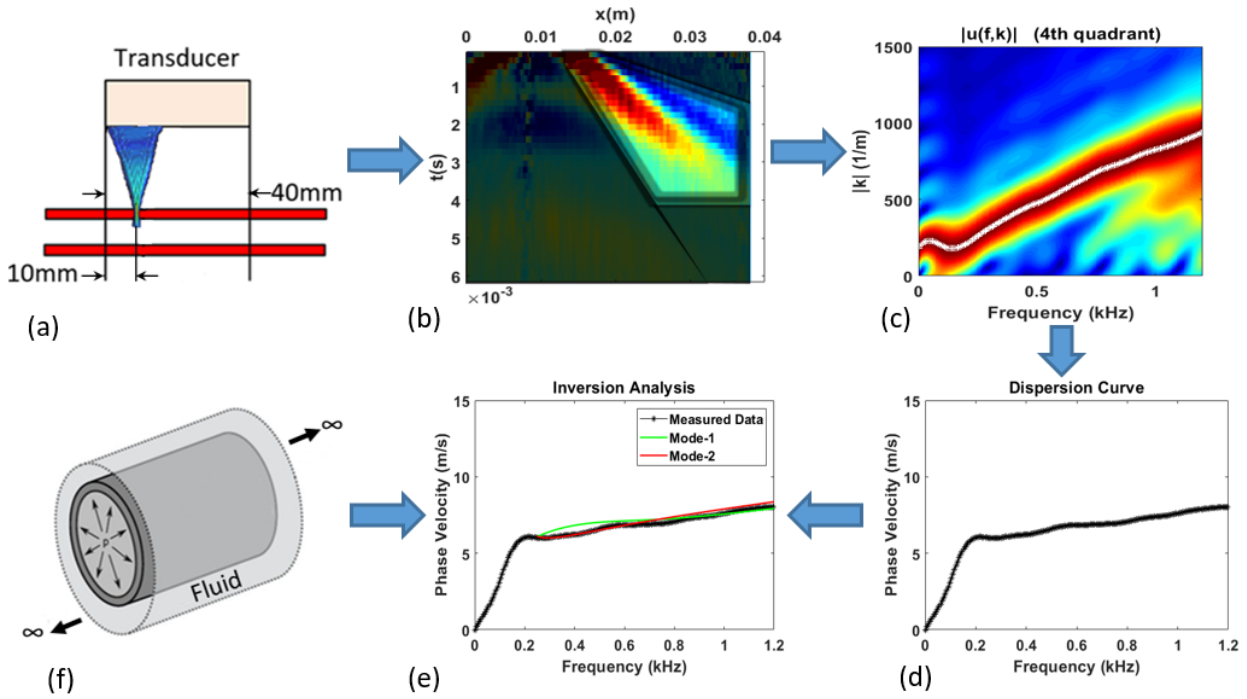

Figure 3.1. (a) Data Acquisition, (b) Data processing, (c) Frequency-wavenumber plot, (d) Measured dispersion curve, (e) Matching of measured and simulated dispersion curves to back-calculate material and geometric properties, (f) Forward model.

DATA ACQUISITION AND SIGNAL PROCESSING

Experimental set-up

Shear wave elastography experiments using Acoustic Radiation Force (ARF) were performed[3] on ten artery mimicking urethane rubber tubes (VytaFlex 10, Smooth-On, Inc., Macungie, PA). The tubes were made in a custom-made mold that could accommodate 3 tubes for a given batch of the rubber. To obtain 10 tubes, four different batches were made as two tubes were damaged in removal from the mold. The tubes are filled with and submerged in water, to simulate blood and surrounding tissue respectively. The inner radius of the tubes is 3 mm and the wall thickness is 1 mm. The schematic of the ARF experimental setup is shown in Figure 3.2. In these experiments a Verasonics V1 system (Verasonics, Inc., Kirkland, WA) was used equipped with a linear array transducer (L7-4, Philips Healthcare, Andover, MA). The 128 element transducer has elements with 0.283 mm width, 0.025 mm kerf, 7 mm height, and an elevation

[3] All the experiments were conducted by the research group of Dr. Matthew W. Urban and Mayo Clinic, and the data were provided to NCSU for further processing and algorithm development.

focus near 25 mm. An ARF push is applied at the x = 10 mm location in Figure 3.2(a), and the vertical motion of the wall is measured at the top of the tube along the axis, from x = 10-40 mm. A 400 μs toneburst at 4.09 MHz was used. The push beam used 64 elements of an ultrasound transducer and was focused at 20 mm (F-number = 1, where F-number is the ratio of the focal depth to the aperture width). Plane wave imaging with 5 MHz pulses was used at a pulse repetition period of 80 μs for a pulse repetition frequency of 12.5 kHz. The particle velocity of the wall was estimated from the acquired in-phase/quadrature (IQ) data using an autocorrelation method (Kasai *et al* 1985). To average the inhomogeneity associated with fabrication, a total of 6 configurations are tested (by performing 60° rotations around the axis). The response is obtained for 10 separate ARF excitations for each of the 6 configurations, leading to 60 data sets for each tube.

To facilitate the validation of the proposed inversion procedure, the material for each tube was tested mechanically, with of Hyper-Frequency Viscoelastic Spectroscopy (Hadj Henni *et al* 2011) (Rheospectris C500+, Rheolution, Inc., Montreal, Quebec, Canada), resulting in the storage, $G_s(\omega)$, and loss, $G_l(\omega)$, moduli for each of the tubes. The moduli were measured from 10-2000 Hz in 10 Hz increments. For each batch of rubber, three cylindrical samples for testing were created when making the tubes. The mean of 3 or 4 acquisitions for each sample were calculated for validation. These results are shown in Figure 3.3, which will be utilized later in the validation section.

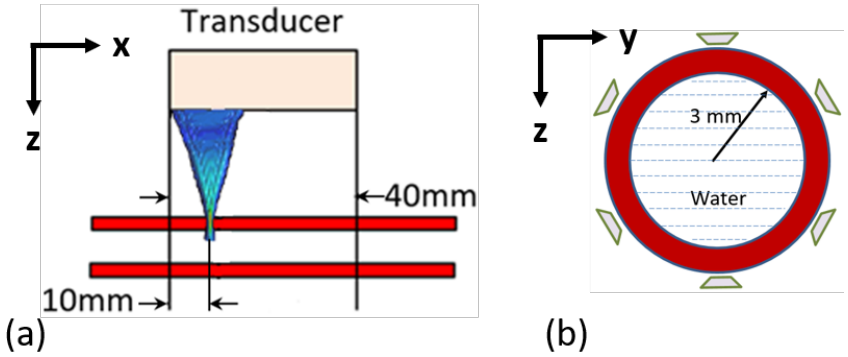

Figure 3.2 Schematic of experimental setup for measuring wall motion. (a) shows the longitudinal view of the tube and ARF transducer, while (b) shows the cross-section of the tube and the six angles used for ARF excitation and acquisition.

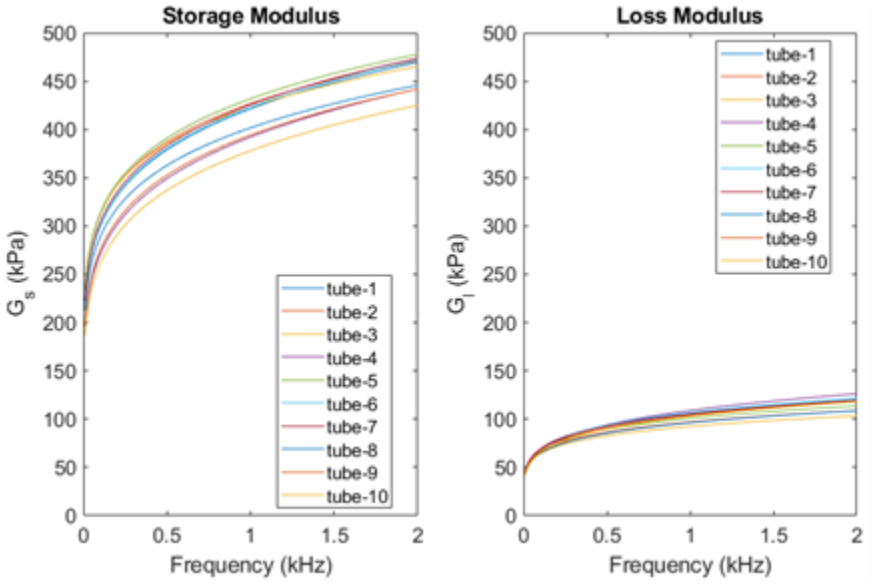

Figure 3.3 Material properties from Rheospectris experiments.

Data processing

Data processing is performed on the wall motion data first in the spatial-temporal domain. The standard approach is to isolate the right propagating wave as shown in Figure 3.4. In the proposed approach, we consider only the dominating part of the right propagating region as shown in Figure 3.5. Specifically, we added a few windowing boundaries to obtain the dispersion curves that are important for inversion. The first windowing boundary, which we call the lower-cut, sets the lower limit on the phase velocity. The second boundary is called the upper cut, as it sets the upper limit on the phase velocity. These lower and upper cuts partially remove the high frequency noise, especially farther from the load at early times, as well as addresses the low signal-to-noise ratio at later times. Finally, the signal is truncated after a maximum time (T-max) to avoid any reflections from the edges of the tube. We consider the resulting trapezoidal region after applying a gradual Gaussian windowing outside these boundaries. The smooth change in the signal amplitude to zero eliminates the spurious Gibbs ringing in the *f-k* domain. To this end, a Gaussian smoothing function of the following form is used.

$$W = e^{-\alpha^2\left(\left(\frac{x-\bar{x}}{x_{max}}\right)^2+\left(\frac{t-\bar{t}}{t_{max}}\right)^2\right)}. \qquad (26)$$

In the above, the parameter α controls the smoothing rate. The parameters x_{max} and t_{max} are the maximum values of x and t in the data, and are utilized essentially as normalization

constants. The values of $\overline{x}$ and $\overline{t}$ are determined based on the slopes of the upper and lower cuts and are given by,

$$\overline{x} = st + x_{shift}, \quad \overline{t} = \frac{x - x_{shift}}{s}, \tag{27}$$

where s is the slope of the cuts. The x_{shift} is the shift value along the x direction as shown in Figure 3.4. The resulting filter is shown in Figure 3.5(a).

The data processing parameters that describe the windowing are chosen based on the observed phase velocity ranges from the phantom experiments. We observe the phase velocity ranges between 4 to 10 m/s, therefore we choose the lower-cut slope as 3 m/s and upper-cut slope as 15 m/s. Both lower and upper cuts are originated from the starting point in the space-time domain. For the truncation time (T-max), we examine the time when the response is sufficiently attenuated, and well before any boundary reflections are observed. We also confirmed that perturbation of the signal-processing parameters has minimal effect on the dispersion curves (results are not presented for brevity). The remaining steps for either the standard or modified approach are the following: (a) applying the 2D FFT to transfer the space-time data into the wavenumber-frequency domain and (b) picking the peak values to obtain the phase-velocity dispersion with phase-velocity $c_p = 2\pi f / k$ plotted against frequency f.

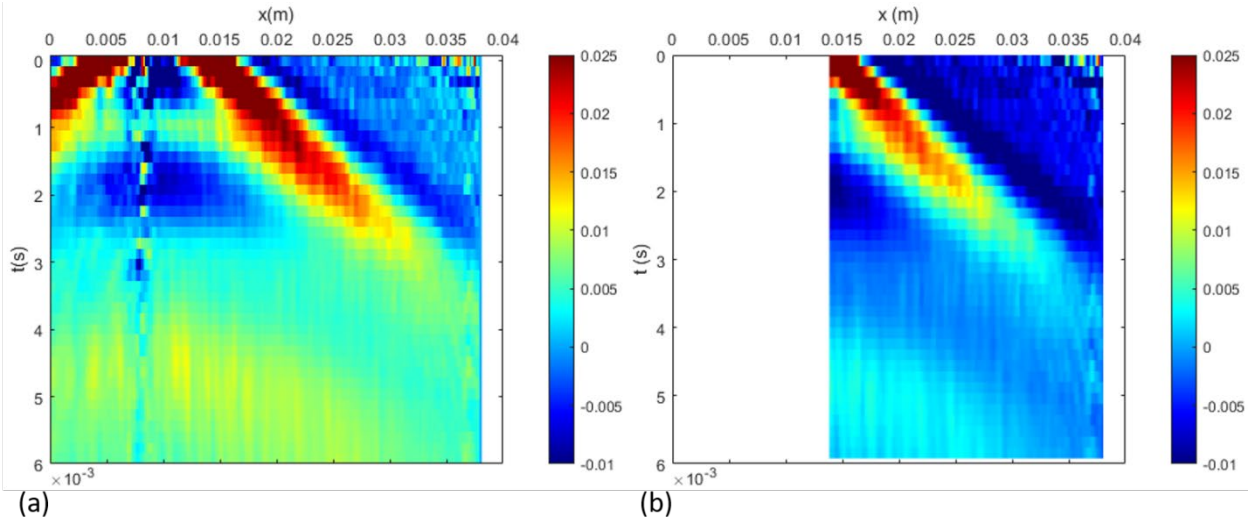

Figure 3.4. Standard approach for data processing: (a) is the actual measured data in space-time, which is curtailed on the left to focus on the right-propagating waves (b).

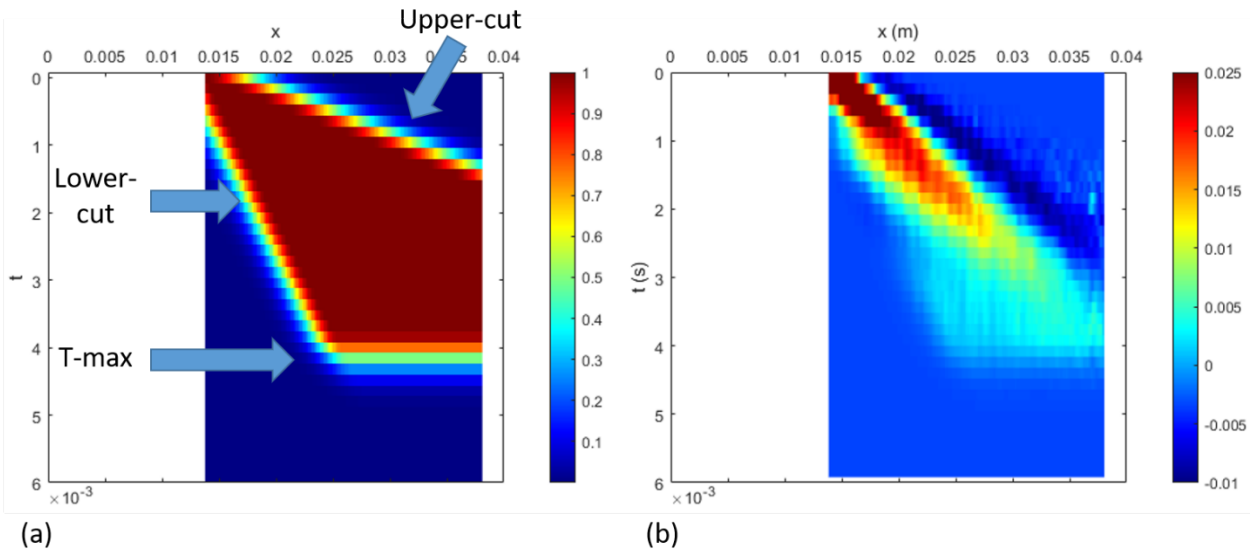

Figure 3.5 Proposed approach for data processing: In addition to the standard approach in the previous figure, additional windowing is applied to ensure that the dispersion curves are best captured within the range of expected phase velocity. The upper cut sets the upper limit to the phase velocity, the lower cut sets a lower limit, while curtailing in time ensures that the reflections from the boundary does not pollute the dispersion curves.

Figure 3.6 illustrates the effect of data processing on the dispersion curve, where the experimental dispersion curves are compared with the expected dispersion curves from the model that will be described below, using the material parameters from Rheospectris measurements (shown in Figure 3.3). Figure 3.6 compares experimental dispersion curves from both regular and modified data processing approaches. Clearly, the data processing modifications bring the experimental dispersion curves much closer to the expected dispersion curves. This improvement in the dispersion curves leads to significant change in the inverted parameters, as discussed in the Validation section.

While other, non-Fourier, methods may be more effective in separating multiple modes with higher fidelity (Tran *et al* 2014, Kijanka *et al* 2018, Kijanka and Urban 2021a, 2021b), we emphasize that the current objective is to obtain the most dominant mode in a particular frequency range. The proposed approach is sufficient to this end and alternative methods are not considered at this time; they may be explored in the future, e.g. if the inversion is performed to match multiple modes at the *same* frequency.

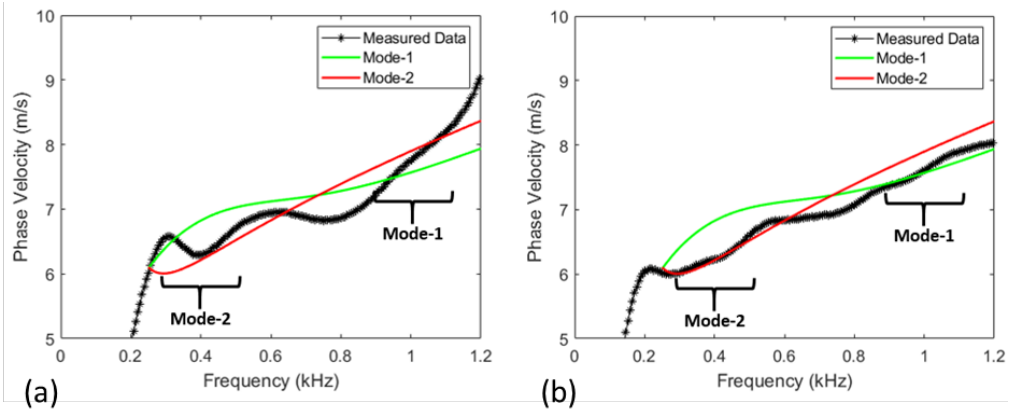

Figure 3.6. Comparison between simulated and measured dispersion curves with standard processing (a) and refined processing (b). In the two highlighted frequency ranges, the processing refinements result in a better match between measured and simulated dispersion curves.

ESTIMATION OF MODULUS AND THICKNESS

Forward model

To obtain the simulated dispersion curves, the rubber tube is modeled as a cylindrical prism made up of an incompressible elastic material, submerged in an inviscid and incompressible fluid. The idealization of incompressibility is adopted for both the arterial wall and the surrounding fluid because the pressure wave velocity is two orders of magnitude larger than the shear wave velocity; explicit inclusion of compressibility does not change the results much and can lead to unnecessary numerical complications. Further, the tube is assumed to be infinite in length because the experimental data is truncated before any reflections from the tube ends are recorded. Such an assumption facilitates the use of a Semi-Analytical Finite Element (SAFE) formulation, where the discretization is performed in the radial direction, while the analytical expansion is utilized in the axial and azimuthal directions (the reader is referred to (Rose 2014) for detailed explanation and (Nelson *et al* 1971, Kausel and Peek 1982, Datta *et al* 1988) for some early work on this topic). The schematic of the geometry is shown in Figure 3.7 (a), and the summary of the formulation is presented in the remainder of the section.

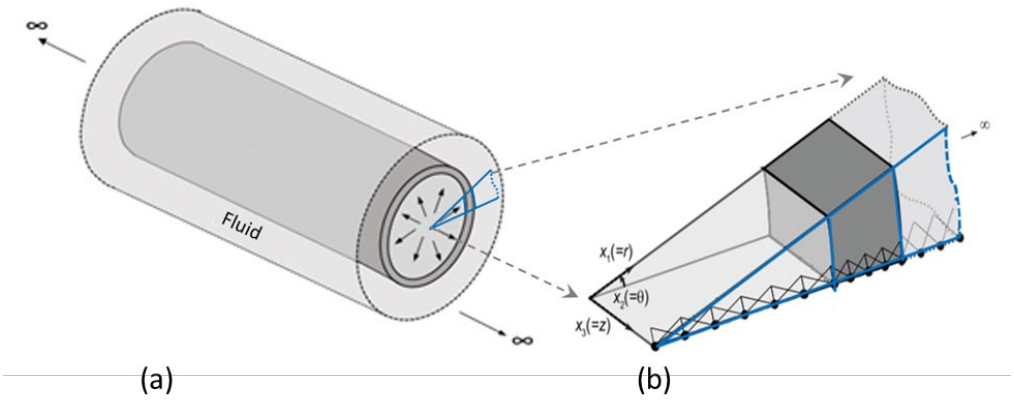

Figure 3.7. Geometry of the immersed tube (a), and finite element discretization in the radial direction (b). Fourier expansion is used in the axial (x_3) and azimuthal (x_2) directions.

The tube deformation is governed by the elastodynamic equation,

$$-\mathbf{L}_{\sigma}^{T}\boldsymbol{\sigma}+\rho_S\frac{d^2\mathbf{u}}{dt^2}=\mathbf{0},\ \text{in}\ \Omega_S\ , \tag{28}$$

where, Ω_S is the solid domain, $\boldsymbol{\sigma}$ is the stress, $\mathbf{u}$ is the displacement, and ρ_S is the density of the solid. The operator $\mathbf{L}_{\sigma}$ is a differential operator representing the symmetric gradient; the details can be found in (Astaneh *et al* 2017).

Given the incompressible and inviscid nature, the Laplace equation governs the response of the fluid

$$\nabla^2 p=0\ \ \text{in}\ \Omega_F \tag{29}$$

where Ω_F is the fluid domain that encompasses the interior and exterior fluid, p is the fluid pressure, and ρ_F is the fluid density.

The interface conditions at the solid-fluid interface Γ_{FS} that couples the solid surfaces with both inside and outside fluid regions are,

$$\boldsymbol{\sigma}\cdot\mathbf{n}_s-p\mathbf{n}_F=0,\ \text{on}\ \Gamma_{FS}\ , \tag{30}$$

$$\rho_F \frac{d^2\mathbf{u}}{dt^2} \cdot \mathbf{n}_s - \frac{\partial p}{\partial \mathbf{n}_F} = 0, \text{ on } \Gamma_{FS} \ . \quad (31)$$

Here, $\mathbf{n}_s$ and $\mathbf{n}_F$ are the unit vectors in the solid and fluid domain respectively, which are in opposite directions. By following the formulation in (Astaneh *et al* 2017), noting that the geometry and material properties are invariant in the horizontal and azimuthal directions, we consider the SAFE formulation in which the radial direction is discretized with finite elements while analytical expansion is employed for the remaining directions. Specifically, we write the solution in terms of wave modes that are harmonic in time, axial direction, *z*, and azimuthal direction, θ. Linear finite element discretization is utilized in the radial direction as shown in Figure 3.7 (b). Putting these ideas together, given the symmetry of the load and thus the response about the *r-z* plane, the solid displacement and fluid pressures can be written as,

$$\begin{aligned}
\mathbf{u}_r(r,\theta,z,t) &= \mathbf{N}_S(r) u_r(n,k_z,\omega) e^{-i\omega t + ik_z z} \cos(n\theta) \\
\mathbf{u}_\theta(r,\theta,z,t) &= \mathbf{N}_S(r) u_\theta(n,k_z,\omega) e^{-i\omega t + ik_z z} \sin(n\theta) \quad (32) \\
\mathbf{u}_z(r,\theta,z,t) &= \mathbf{N}_S(r) u_z(n,k_z,\omega) e^{-i\omega t + ik_z z} \cos(n\theta)
\end{aligned}$$

$$\mathbf{p}(r,\theta,z,t) = \mathbf{N}_F(r) p(n,k_z,\omega) e^{-i\omega t + ik_z z} \cos(n\theta) \quad (33)$$

where $\mathbf{N}_S$ and $\mathbf{N}_F$ are the finite element shape functions along the radial direction for the solid and fluid domain respectively, *n* is the index of the azimuthal harmonic, k_z is the wavenumber along the axial direction, $\omega = 2\pi f$ is the temporal frequency, and $i = \sqrt{-1}$. Substituting (32) and (33) in governing equations (28) and (29), and interface conditions (30) and (31), results in an eigenvalue problem,

$$\left(k_z^2 \begin{bmatrix} \mathbf{K}_2^S & 0 \\ 0 & \kappa \mathbf{K}_2^F \end{bmatrix} + \begin{bmatrix} \mathbf{K}_0^S - \omega^2 \mathbf{M}^S & -\kappa \mathbf{C}_{SF} \\ -\omega^2 \mathbf{C}_{SF}^T & \kappa \mathbf{K}_0^F \end{bmatrix} \right) \begin{Bmatrix} \boldsymbol{\phi}_S \\ \boldsymbol{\phi}_F \end{Bmatrix} = \begin{Bmatrix} 0 \\ 0 \end{Bmatrix} \quad (34)$$

where κ is the normalization factor to improve the conditioning of the system. The solid-domain contribution matrices, $\mathbf{K}_2^S, \mathbf{K}_0^S, \mathbf{M}^S$, the fluid-domain contribution matrices, $\mathbf{K}_2^F, \mathbf{K}_0^F$, and the fluid-structure interaction matrix, $\mathbf{C}_{SF}$ are defined in (Astaneh *et al* 2017); they depend on the geometry (inner radius and thickness) and the material properties (densities and shear modulus).

The quadratic eigenvalue problem is solved for each frequency ω, to result in the wavenumber k_z, resulting in the dispersion relationship. The dispersion curves can either be plotted in $k_z - \omega$ space, or a plot of phase velocity ($c_p = \omega/k_z$) vs. cyclic frequency ($f = \omega/2\pi$). Consistent with the convention followed in experimental data processing (Figure 3.5), we follow the latter approach.

The intricacies of the forward modeling include (a) treating incompressibility related linear finite element locking through selective reduced integration (Hughes 2012), (b) simulating the unbounded exterior with perfectly matched discrete layers (Savadatti and Guddati 2010a), and (c) normalization to improve the conditioning in the limit of incompressibility (Roy and Guddati 2021). Further details can be found in (Roy and Guddati 2021), where the results from the forward model are compared with the reference solution obtained through convergence analysis (the reference solution is obtained using discretization with highly accurate 5-noded finite elements (Astaneh *et al* 2017).

Before moving on to inversion, we emphasize that the forward model captures fully three-dimensional wave propagation in the artery. The simulation is simplified mainly due to the simplicity of the tube geometry, allowing the use of SAFE formulation to reduce the computational effort significantly, thus enabling us to use the existing in-house code (Vaziri Astaneh and Guddati 2017a) with the minor modifications for the incompressible waveguides and then the off-the-shelf iterative optimization algorithms to estimate the material properties, which is described in the next section.

Inversion through Optimization

Our main goal is to estimate the shear modulus of the artery given the radius and wall thickness. Looking ahead to *in vivo* application of methodology, we observe that the wall thickness, which is obtained from B-mode images, may not be accurately measured (because the thickness is just a few pixels wide). Given this, we add to our objective the case of simultaneous estimation of shear modulus and wall thickness for known radius of the tube. It is expected from wave physics that the phase velocity will be influenced by both the shear modulus and thickness, making this a plausible goal (we also confirmed that thickness is an influential parameter through sensitivity analysis presented later). Further, at this stage, we assume that the time/frequency dependence of viscoelasticity of the wall is known, and only the scalar measure of the shear

modulus is not known. Specifically, we express viscoelastic (complex-valued) shear modulus $G(\omega)$ as,

$$G(\omega) = G_s(\omega) + iG_l(\omega) = G_0 \times G_\omega(\omega), \qquad (35)$$

where G_s and G_l are the (real-valued) storage and loss moduli, respectively. Complex-valued $F(\omega)$ captures the frequency-dependence of $G(\omega)$, while G_0 captures the overall magnitude. Without loss of generality, we assume $G_0 = \left|G(\omega = 20\pi)\right|$, because $\omega = 20\pi$ is the first frequency point in Rheospectris data (note that this is arbitrary). In our inversion framework, we assume that G_0 is the unknown to be determined, while $F(\omega)$ is assumed to be known (obtained from the Rheospectris measurements). Inverting for frequency dependency is indeed of interest, but beyond the scope of the current study. Thus, the parameters for our inversion is the wall thickness (h) and the single shear modulus parameter (G_0).

The thickness and modulus are estimated by minimizing the difference between the experimentally measured dispersion curves and theoretical dispersion curves computed from the model. Note that there exists a single measured dispersion curve, which is obtained from a single peak in the *f-k* plot for each frequency (obtaining multiple peaks is not practical due to the low signal-to-noise ratio, especially for *in vivo* data). As highlighted in (Astaneh *et al* 2017), this measured dispersion curve does not coincide with a single mode of the simulated dispersion curve, but matches with different modes for different frequency ranges. Specifically, as discussed in (Astaneh *et al* 2017) and highlighted in Figure 3.6, the measured dispersion curve matches with flexural mode 2, F(2,1), for 300-500 Hz, while it matches with flexural mode 1, F(1,1), for 900-1200 Hz frequency range. Here, we follow the work of Gazis (Gazis 1959a, 1959b) for the mode numbers notation. In addition, we confirmed this match by comparing with the theoretical dispersion curves of other wave modes that lie in the vicinity (see Figure 3.8; note that modes with significant evanescence are filtered at low frequencies). As seen in the figure, the L(0,1) mode asymptotically merges with the F(1,1) in the higher frequency range; it is possible that this mode may contribute significantly to the measured dispersion curve for some geometries, material properties and frequency ranges. However, our focus is on frequencies below 1000 Hz, and given that the measured dispersion curve more closely matches with F(2,1) and F(1,1) in this range, we chose to invert by matching with F(2,1) and F(1,1).

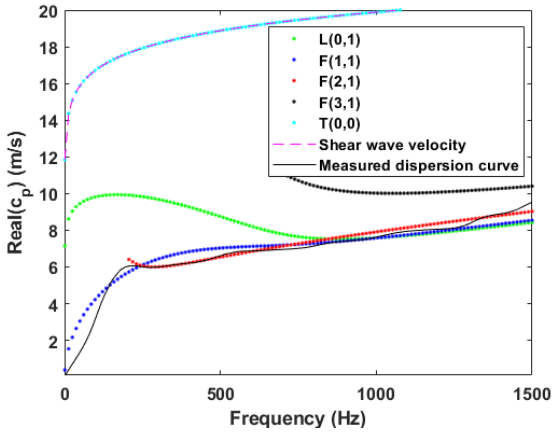

Figure 3.8 Comparison of the theoretical and measured dispersion curves for the viscoelastic tube

In the inversion analysis, we consider the 900-1000 Hz frequency band for the mode 1 due to the fact that we will not have necessary data beyond 1000 Hz for the *in vivo* case. Given this observation, we define the objective function as the relative least-squares difference between the dispersion curves:

$$F_{objective} = \frac{\sum_{f_i=f_1}^{f_2}\left(c_2^s(f_i,q)-c^m(f_i)\right)^2 + \sum_{f_i=f_3}^{f_4}\left(c_1^s(f_i,q)-c^m(f_i)\right)^2}{\sum_{f_i=f_1}^{f_2}\left(c_2^s(f_i,q)\right)^2 + \sum_{f_i=f_3}^{f_4}\left(c_1^s(f_i,q)\right)^2}, \quad q=[h,G_0] \tag{36}$$

where, c_1^s and c_2^s are the simulated phase velocities corresponding to the modes 1 and 2, respectively, and c^m is the phase velocity from the measured data. Consistent with the discussion above, $f_1 = 300\ Hz$, $f_2 = 500\ Hz$, $f_3 = 900\ Hz$, and $f_4 = 1000\ Hz$. These frequency ranges may change depending on the geometry and may need to be revisited for *in vivo* experiments. Note that in the objective function, we consider the phase velocity dispersion instead of the $k(\omega)$ dispersion. The reason is that the phase velocity is fairly constant in the considered frequency range unlike the $k(\omega)$ dispersion case; matching $k(\omega)$ curves will give higher weights to higher-frequency data which is undesirable.

The inverse problem thus involves estimating the parameters G_0 and h, given the measured dispersion curve, radius of the tube, and the viscoelastic time-dependency $F(\omega)$. This can be performed, e.g. by formulating in a robust PDE constrained optimization framework with

explicit formulation of gradient and Hessian, potential with adjoint operators. Such an approach is beneficial for a large parameter space and expensive forward models. However, given that we are inverting for just two parameters and have an extremely efficient forward model, we resort to the black-box optimization algorithms implemented in MATLAB, some of them based on finite-difference gradients.

Inversion Models

To minimize the objective function in Equation (36), we consider both local and global optimization approaches. While the local optimization gives a minimizer, global optimization removes the possibilities of obtaining a spurious local minimizer. In the local optimization framework, we consider (a) interior point method with the BFGS Hessian (Waltz *et al* 2006), (b) Nelder-Mead algorithm (Lagarias *et al* 1998), (c) Non-linear Optimization Mesh Adaptive Direct Search (NOMADS) algorithm (Currie and Wilson 2012). The global optimization algorithms that we consider include (d) Particle-Swarm (Kennedy and Eberhart 1995). Note that except the Nelder-Mead algorithm, all other considered models are constrained optimization and in these cases, we impose box constraints, limiting each parameter to be within $\pm 30\%$ of the mean value. For all the above-mentioned inversion models, we employ the MATLAB optimization toolbox except for the NOMADS algorithm for which we use the available function in (Anon n.d.).

RESULTS AND DISCUSSION

Parameter sensitivity

Before embarking on the actual inversion process, we perform formal sensitivity analysis to ensure that the modulus *and* thickness are identifiable and influential. We perform the local sensitivity analysis by forming the Fisher matrix (Smith 2014). The Fisher matrix is computed using the finite difference method with a step size of 10^{-5}. The parameters are scaled with respect to their mean values to avoid any potential numerical issues. The rank of the resulting Fisher matrix is 2 and the condition number approximately 187, indicating that both thickness h and modulus parameter G_0 are identifiable parameters. The global sensitivity study is performed using the Saltelli Sobol analysis (Saltelli *et al* 2007) with 4500 randomly generated points within a $\pm 45\%$ rectangular range in the parameter space around the mean value of each parameter h, G_0. The resulting first-order Sobol indices are [0.66, 0.27] and the total Sobol indices are [0.63, 0.50], indicating sensitivity to both parameters, with higher sensitivity to thickness.

Validation

We perform validation of the proposed inversion procedure using the experimental data in two different ways: (a) estimate the modulus with known (directly measured) thickness, and (b) simultaneous inversion of the thickness and modulus. The results are compared with the actual values to assess the effectiveness of the proposed technique. The results from one-parameter (modulus) inversion are shown in Figure 3.9(a), which indicates that the proposed inversion approach results in high accuracy, irrespective of the optimization technique used (the error is less than 4% for 70% of the cases). The computational cost is presented in Figure 3.9(b), which indicates that all the optimization algorithms converge fairly quickly. Because the interior point method with the BFGS Hessian is consistently more efficient, this method is advocated for inverting for the tube modulus. The number of function evaluations for the BFGS method is between 10 and 15. This, combined with the efficiency of the forward model, results in a highly efficient and practical inversion of the modulus, with a runtime of around 20 seconds, for the BFGS method, on a standard desktop computer (Intel® Core(TM) i7-6700 CPU, 3.40GHz with 32.0 GB RAM and 64-bit OS), as shown in Figure 3.9(b). Here, we highlight that the inversion analysis is carried out for all 60 measurements for each tube simultaneously, i.e. we minimize the total error by combining the difference between each of the 60 measured dispersion curves with a single theoretical dispersion curve. Thus, the result would be a single estimate of the modulus parameter.

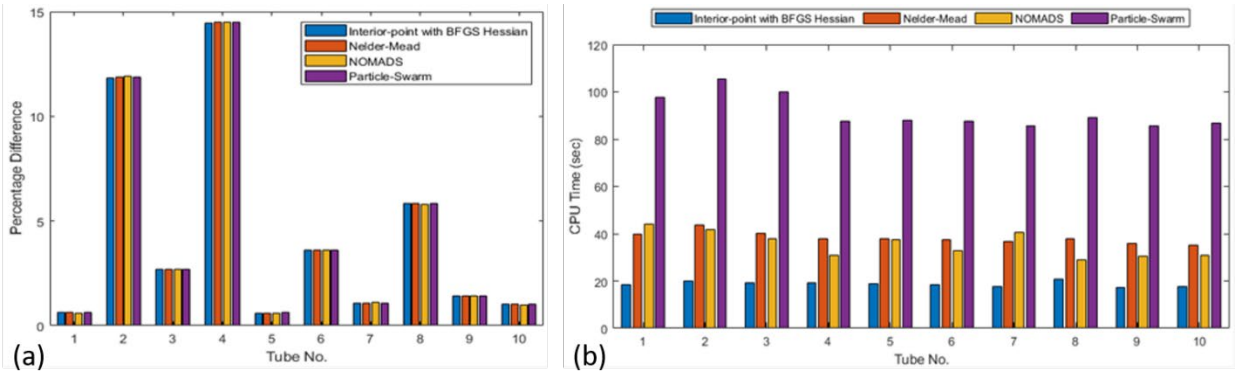

Figure 3.9. (a) Error in the inverted shear-modulus parameter, G_0; (b) CPU time for modulus inversion

The results from two-parameter inversion for modulus and thickness are shown in Figure 3.10. As expected, the results are not as accurate as those from single-parameter inversion. For only 40% of the cases, both parameters have an error of less than 10%. Based on this, at this time,

we advocate the use of single-parameter inversion by relying on the measured thickness, which may have some error for *in vivo* cases. The computational cost for two-parameter inversion is shown in Figure 3.11. Again, as expected, the convergence is not as fast as the single-parameter inversion, but the number of function evaluations is still fairly small. The interior-point method with the BFGS Hessian required 40-50 iterations with a total computational cost of around a minute on the same standard desktop computer.

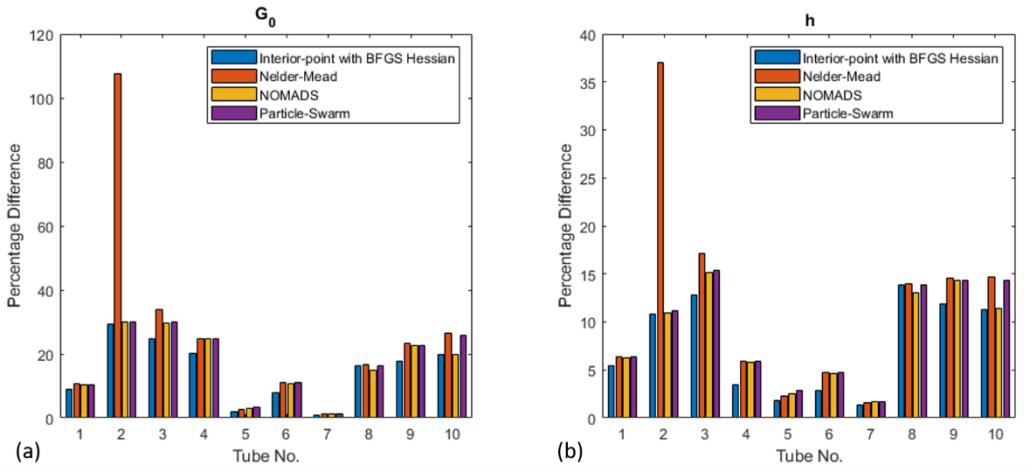

Figure 3.10. Error in the inverted shear-modulus parameter, G_0 (a) and thicknesses, h (b).

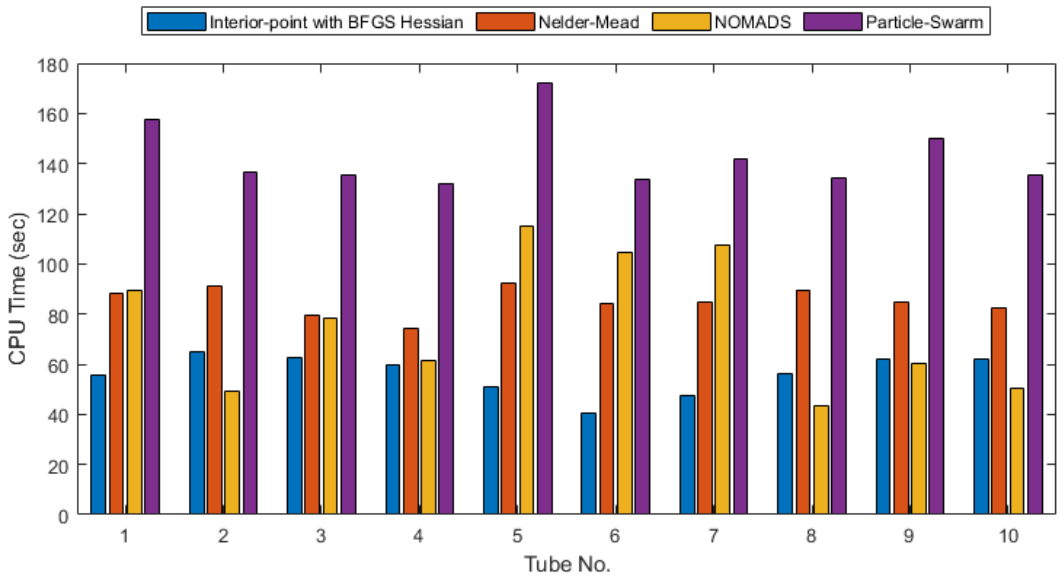

Figure 3.11. CPU time for combined inversion for modulus and thickness.

As we observe for tube 2, both inversion analyses (modulus as well as modulus-thickness inversion), the percent difference is quite high compared to the other tubes. This can be justified

by looking at the measured dispersion curves for this tube as shown in Figure 3.12 (a). Recall that we apply the acoustic radiation force individually at six angular positions and repeat the acquisition ten times for each of the six angular positions. In the case of tube 2, we notice good correlation within each set of ten acquisitions, but low correlation across the six angular cases. This indicates the tube may not be homogeneous due to imperfect fabrication. On the other hand, tube 5, which has yielded lower error in the inversion analysis, has tight correlation across all acquisitions and angular cases as presented in Figure 3.12 (b). With respect to the significantly high error for tube 2 with the Nelder-Mead algorithm (inversion for both modulus and thickness), the solution seemed to have converged to a local minima far from the solution as the underlying optimization framework does not allow any constraints. This is a reason, in addition to computational cost, that we propose to use BFGS approach as the method of choice.

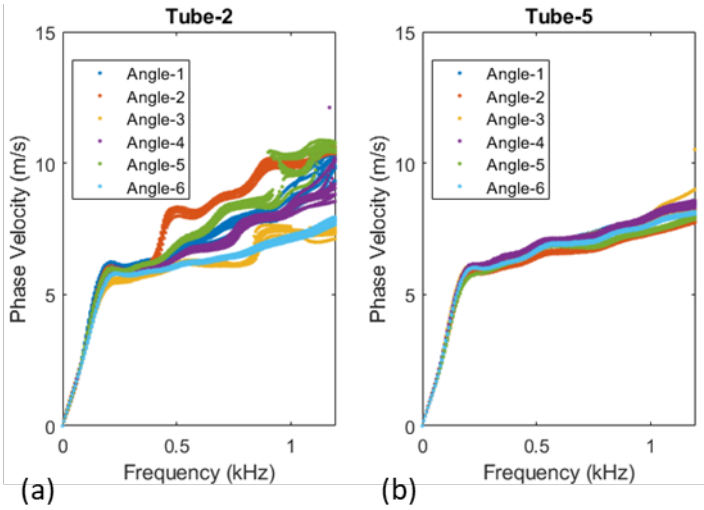

Figure 3.12 Measured dispersion curves for Tube-2 (a) and Tube-5 (b)

Effect of data processing

Earlier in the chapter, we illustrated that data processing details are critical to obtaining accurate dispersion curves. However, dispersion curves are only of intermediate interest, with the final objective being the modulus estimation. The natural question then is, what if the inversion is performed without the data processing refinements? We performed this exercise and observed that standard data processing resulted in an average modulus error of 22.4% compared to a significantly reduced error of 5% when the data processing refinements are employed.

Effect of multimodal inversion

Another important question that may arise is: how important is it to match with different simulated curves for the two frequency ranges (multi-modal inversion)? What if the inversion is performed by matching with a single, fundamental dispersion curve for both frequency ranges (single-mode inversion)? For example, when applied to tube 1, it turns out that single-mode inversion (with the first mode, $n = 1$) results in higher errors in the estimated modulus (10.6%) compared to that from multi-modal inversion (0.6%), confirming the benefit of multimodal inversion.

The proposed study is only a step towards estimation of arterial stiffness using ARF excitation. The issues that require attention before applying it to *in vivo* data from human arteries include: (a) automatic determination of signal processing parameters (they are currently determined manually); (b) estimating the frequency dependence directly from ARF measurements instead of using the information from Rheospectris measurements; (c) validation studies for differing thicknesses (we validated the model with single thickness of 1 mm as dictated by the mold and it would be useful to validate for other thicknesses); (d) optimizing the experimental setup including the number of acquisitions (the number of acquisitions and orientations are chosen arbitrarily in this chapter, erring on the conservative side), (e) validation using *ex vivo* data, e.g. using porcine aortas; and (f) examining the effect of surrounding tissues as well as physiological motion. Further research is underway in several of these directions and will be reported in the future.

CONCLUSIONS

This chapter presents a new shear wave elastography (SWE) approach to estimate the arterial stiffness from acoustic radiation force measurements. The methodology is built on various refinements in different steps of SWE: (a) signal processing refinements through simple windowing informed by physical understanding, (b) efficient forward model for incompressible viscoelastic tubes, and (c) inversion by matching the measured dispersion curve with not one, but two separate dispersion curves (multimodal inversion). Through validation studies using extensive ARF experimental data, we observed that the proposed inversion approach results in high accuracy in estimating the shear modulus (less than 4% in 70% of the cases). We also observed that not using signal processing improvements or multimodal inversion degrades the accuracy of the modulus estimates. Finally, owing to the computational efficiency of the underlying forward

model, the inversion procedure is highly efficient, taking less than 20 seconds on a regular computer.

In addition to inverting for just shear modulus, we also explored the possibility of simultaneous inversion of both shear modulus and wall thickness. The resulting accuracy is not as good as the accuracy of inverting for just shear modulus. Given this, at this time, we suggest measuring the wall thickness and then estimating the modulus from the proposed inversion framework. For *in vivo* settings, the thickness measured from ultrasound images may not be accurate, but will be close to the actual value, with some level of known error variance based on the transducer. Thus, the measured thickness can be used as prior information in a simultaneous inversion for shear modulus and thickness. On the other hand, the radius, which is not as small as the thickness, can reliably be measured through ultrasound. Moreover, the dispersion curves are not as sensitive to radius perturbations as to thickness perturbations (Astaneh *et al* 2017). To address imperfect thickness measurements, fortunately, probabilistic inversion is feasible due to the efficiency of the forward model; this is the subject of ongoing research. In the current work, we fix the time/frequency dependency of the modulus and estimated the overall magnitude of the modulus. In reality, the complex viscoelastic modulus (both the amplitude and time dependency) needs to be estimated, which is also the subject of ongoing research. Finally, our study assumes isotropic elasticity, which is valid for phantom experiments. For real arteries, further beneficial enhancements would include: tissue anisotropy (Li *et al* 2017b, Shcherbakova *et al* 2017) and non-prismatic geometry (Karageorgos *et al* 2020, Wang and Lee 2020); these are subjects of future research.

CHAPTER 4: PROBABILISTIC GUIDED WAVE INVERSION FOR ARTERIAL WALL THICKNESS AND ELASTIC MODULUS

ABSTRACT

Arterial stiffness is one of the important biomarkers for early detection of the cardiovascular diseases. Among various non-invasive approaches, shear wave elastography estimates the local arterial stiffness through guided wave inversion (GWI), specifically by matching the measured wave dispersion with the simulated dispersion. The GWI results will be more insightful if we incorporate the measurement uncertainty to the inversion analysis. Motivated by this, in this chapter, we provide a preliminary framework for probabilistic guided wave inversion that considers the measurement uncertainty in the analysis. In this work, we present a frequentist framework which is the building block for the Bayesian inference. Besides the elastic modulus parameter, the arterial wall thickness is considered an unknown inversion parameter. Owing to the small length of the wall thickness, the B-mode images for wall thickness is not reliable. This forces us to invert thickness parameter, however, in future, we will consider the B-mode images as the prior information to our model in the Bayesian setting. In this chapter, the resulting model is validated with a rubber tube phantom experiments that mimic healthy human carotid artery.

INTRODUCTION

Arterial stiffness is a well-known indicator for the early onset of multiple cardiovascular diseases (Cheng *et al* 2002, Laurent *et al* 2000, Kingwell and Gatzka 2002, Sutton-Tyrrell *et al* 2005, Dolan *et al* 2006). Among the non-invasive techniques to estimate artery stiffness, the Pulse Wave Velocity (PWV) method is widely used due to its simpler setup. However, as noted in (Couade *et al* 2010), the PWV suffers several limitations. More recent imaging techniques based on Acoustic Radiation Force (ARF) addresses some of the limitations in the PWV approach. The underlying idea in the ARF based techniques is to excite the tissue locally and record the tissue response spatially and temporally (Doherty *et al* 2013). Among the ARF based methods, the Shear Wave Elastography (SWE) is a promising tool due to its consideration of the shear wave propagation. In the case of soft tissue, the shear wave speed is in the range for the standard ultrasound transducer to detect reliably.

The SWE has been employed in several biomedical examinations of various organs which can be grouped into two – (1) bulk organs such as kidney (Amador *et al* 2011), liver (Chen *et al*

2009), and (2) boundary sensitive organs such as arterial wall (Zhang *et al* 2005, Bernal *et al* 2011, Couade *et al* 2010), cornea (Bernal *et al* 2011, Tanter *et al* 2009, Nguyen *et al* 2012), Achilles tendon (Brum *et al* 2014, Yeh *et al* 2016, Helfenstein-Didier *et al* 2016). While the bulk organs possess simpler non-dispersive wave propagation, the complexity of dispersive wave behavior in boundary sensitive organs gives rise to better characterizing of the tissue.

To address the complexity associated with the arterial waveguide model, in the earlier researches, we observe an immersed plate model (Couade *et al* 2010, Bernal *et al* 2011, Nguyen *et al* 2011, Widman *et al* 2015, Jang *et al* 2015, Widman *et al* 2016, Maksuti *et al* 2016, Li *et al* 2017a), annuli waveguide (Li *et al* 2017c), hollow tube waveguide (Zhang *et al* 2005, Flamini *et al* 2015), fluid-filled tube (Flamini *et al* 2015, Lin *et al* 2015), immersed fluid-filled 3D finite element model (Dutta *et al* 2015), immersed fluid-filled SAFE model (Astaneh *et al* 2017). The very recent time model, (Roy *et al* 2021), simplifies the model proposed by (Astaneh *et al* 2017) with linear finite elements.

Besides proposing a better representative waveguide model in (Roy *et al* 2021), we developed an inversion framework in the deterministic setting to estimate both arterial elastic modulus and wall thickness. In that work, we observed that the combined inversion of thickness and modulus parameter resulted in significantly less accuracy compared to inverting just for the modulus. This indicates that utilizing thickness prior information will improve the inversion analysis. Fortunately, the B-mode images can be employed to get the prior information for the thickness. Here note that, the B-mode image data is not fully reliable due to the small scale (a few pixels wide) of the wall thickness.

Utilization of the parameter prior information is better suited in the probabilistic setting. Motivated by this, the objective of this chapter is to develop a preliminary framework for probabilistic inversion. To do this, we start from the inversion model proposed by (Roy *et al* 2021) and extend it to the probabilistic setting. Although our final goal is to incorporate the thickness prior information which traditionally fits in the Bayesian setting, in this work, we present a Frequentist approach which is a building block towards the Bayesian setting. We validate our proposed approaches with a rubber tube phantom experiment data.

The overall approach involves three primary steps – (1) processing the ARF data to obtain the dispersion in the measured data, (2) simulating the waveguide dispersion through a computationally efficient forward model, and (3) probabilistic inversion to incorporate

measurement uncertainty while we minimize the difference between the measured and simulated wave dispersions.

DATA ACQUISITION AND MEASURED DISPERSION CURVE

SWE experiments were executed[4] on ten human carotid artery mimicking urethane rubber tubes (VytaFlex 10, Smooth-On, Inc., Macungie, PA). A customized mold was employed to obtain three tubes from a given batch of rubber. Four different batches were made, resulting in a total of twelve tubes. Finally, 10 of the 12 tubes are analyzed as two of them were damaged while removing from the mold. To simulate blood and the surrounding tissue, the tubes are filled with and immersed in water respectively. The inner radius of the tubes is 3 mm, and the wall thickness is 1 mm. Figure 4.1 shows the schematic of the experimental setup.

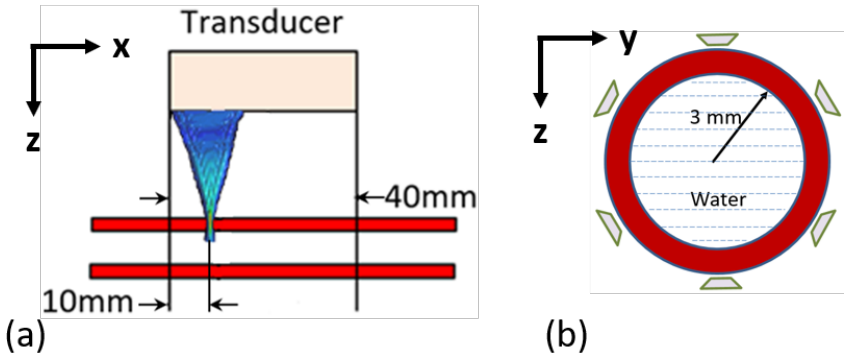

Figure 4.1 Schematic of the experimental setup for measuring wall motion. (a) shows the longitudinal view of the tube and ARF transducer, while (b) shows the cross-section of the tube and the six angles used for ARF excitation and acquisition.

ARF excitation as well as wall velocity measurements are performed using a Verasonics V1 system (Verasonics, Inc., Kirkland, WA) equipped with a 128-element linear array transducer (L7-4, Philips Healthcare, Andover, MA). As shown in Figure 4.1, an ARF push is applied at x = 10 mm location, and the radial motion of the wall is measured at the top of the tube along the axial direction from x = 10 mm to 40 mm. The details of these experiments can be found in (Roy *et al* 2021). Each tube is rotated by 60 degrees around the axis to the measurements are repeated. 10 separate ARF excitations are applied for each of the 6 angular configurations leading to a total of 60 data sets for each tube.

[4] All the experiments were conducted by the research group of Dr. Matthew W. Urban and Mayo Clinic, and the data were provided to NCSU for further processing and algorithm development.

For the validation, each tube material was tested mechanically with the hyper-frequency viscoelastic spectroscopy (Rheospectris C500+, Rheolution, Inc., Montreal, Quebec, Canada) resulting in storage and loss moduli for each tube. Here also the readers are referred to (Roy *et al* 2021) for further details of the Rheospectris measurements. Figure 4.2 shows the frequency-dependent storage and loss (shear) moduli for each of the 10 tubes.

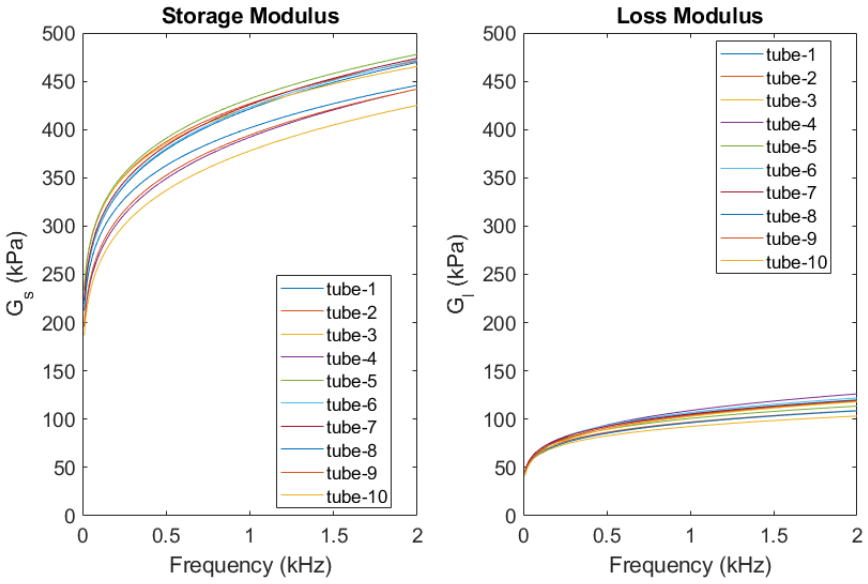

Figure 4.2 Material properties from Rheospectris experiments.

Once we have the velocity data in the spatiotemporal $(x-t)$ domain, we apply windowing to isolate the main propagating part (see Figure 4.3) to improve measured dispersion curves as detailed in (Roy *et al* 2021). In the next step, we apply the 2D Fast Fourier Transform to obtain wavenumber-frequency $(k-\omega)$ representation of the wall velocity. The $k-\omega$ data is processed through peak-picking to obtain the dispersion curve, i.e. phase-velocity $\left(c_p = \omega/k\right)$ as a function of frequency; we refer to this as the *measured* dispersion curve (Figure 4.4).

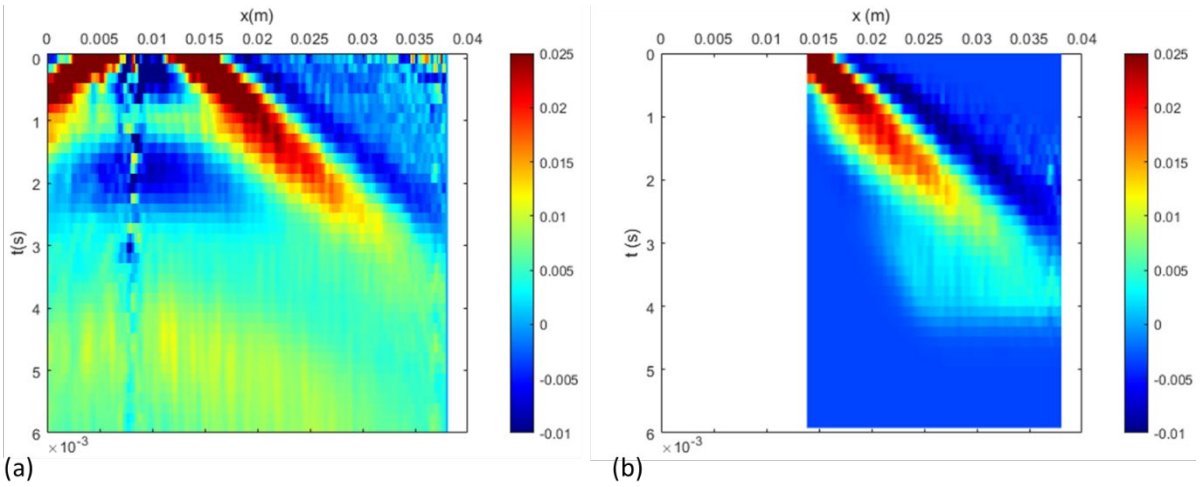

Figure 4.3 The original velocity data in the spatial-temporal domain is shown in (a). The processed data after applying the windowing boundaries is shown in (b).

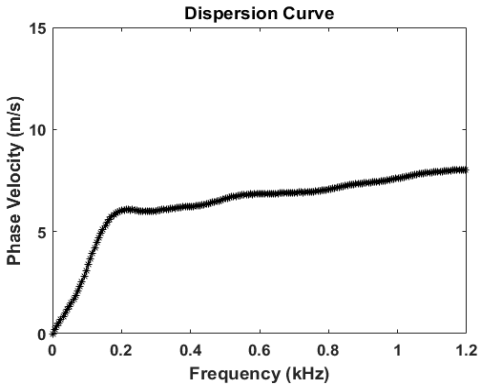

Figure 4.4 Measured phase-velocity dispersion curve

FORWARD MODEL AND SIMULATED DISPERSION CURVES

The rubber tube is simulated as an axisymmetric cylindrical waveguide made of incompressible viscoelastic material. The surrounding fluid is simulated as incompressible, inviscid fluid. The incompressibility assumption for both solid and surrounding fluid media is valid as the pressure wave velocities in solid and fluid are two orders of magnitude higher than the shear wave velocity in the solid. We assume infinite length for the tube since the measured data is truncated and does not contain any reflections from the tube end. In addition, we assume invariant material properties in the axial and azimuthal directions. All these assumptions lead us to utilize the semi-analytical finite element (SAFE) framework with harmonic solutions in the circumferential and axial direction and finite element discretization only in the radial direction. This makes the forward model extremely efficient compared to, e.g. the 3D finite element model.

The schematic of the waveguide geometry is presented in Figure 4.5, and the framework is described briefly in the remaining part of this section. For the details of the forward model, the readers are referred to (Roy and Guddati 2021).

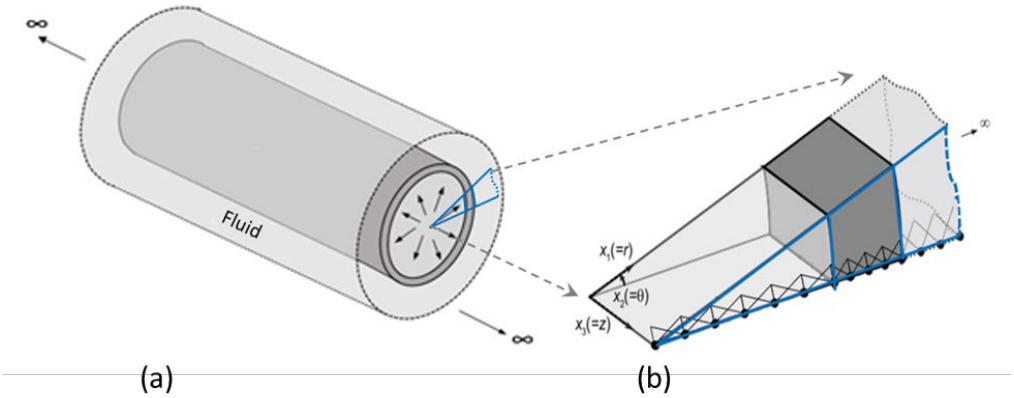

Figure 4.5 Geometry of the immersed tube (a), and finite element discretization in the radial direction (b). Fourier expansion is used in the axial (x3) and azimuthal (x2) directions.

The deformation in the solid medium is governed by the Elastodynamic equation,

$$-\mathbf{L}_{\sigma}^{T}\boldsymbol{\sigma}+\rho_S\frac{d^2\mathbf{u}}{dt^2}=\mathbf{0},\ \text{in}\ \Omega_S\,, \tag{37}$$

where, Ω_S is the solid domain, $\boldsymbol{\sigma}$ is the stress, $\mathbf{u}$ is the displacement, and ρ_S is the density of the solid. The operator $\mathbf{L}_{\sigma}$ is a differential operator representing the symmetric gradient; the details can be found in (Roy and Guddati 2021).

The pressure in the fluid medium is governed by the acoustic wave equation which leads to the Laplace equation in the limit of incompressibility,

$$\nabla^2 p=0\ \ \text{in}\ \Omega_F\,, \tag{38}$$

where Ω_F is the fluid domain that encompasses the interior and exterior fluid, p is the fluid pressure, and ρ_F is the fluid density.

The interface conditions at the solid-fluid interface Γ_{FS} are,

$$\boldsymbol{\sigma}\cdot\mathbf{n}_s-p\mathbf{n}_F=0,\ \text{on}\ \Gamma_{FS}\,, \tag{39}$$

$$\rho_F \frac{d^2\mathbf{u}}{dt^2}\cdot\mathbf{n}_s - \frac{\partial p}{\partial \mathbf{n}_F} = 0, \text{ on } \Gamma_{FS}\ , \qquad (40)$$

where, $\mathbf{n}_s$ and $\mathbf{n}_F$ are the unit vectors in the solid and fluid domain respectively, which are in opposite directions. In the SAFE framework, we consider the wave modes which are harmonic in time (t), circumferential (θ), and axial (z) directions. 1D piece-wise linear finite element discretization is utilized in the radial direction. Considering the symmetry of applied load (thus symmetric response about the r-z plane), we write the displacements in the solid domain and the pressure in the fluid domain as,

$$\begin{aligned}
\mathbf{u}_r(r,\theta,z,t) &= \mathbf{N}_S(r)u_r(n,k_z,\omega)e^{-i\omega t+ik_z z}\cos(n\theta)\\
\mathbf{u}_\theta(r,\theta,z,t) &= \mathbf{N}_S(r)u_\theta(n,k_z,\omega)e^{-i\omega t+ik_z z}\sin(n\theta) \qquad (41)\\
\mathbf{u}_z(r,\theta,z,t) &= \mathbf{N}_S(r)u_z(n,k_z,\omega)e^{-i\omega t+ik_z z}\cos(n\theta)
\end{aligned}$$

$$\mathbf{p}(r,\theta,z,t) = \mathbf{N}_F(r)p(n,k_z,\omega)e^{-i\omega t+ik_z z}\cos(n\theta) \qquad (42)$$

where $\mathbf{N}_S$ and $\mathbf{N}_F$ are the finite element shape functions along the radial direction for the solid and fluid domain respectively, n is the index of the azimuthal harmonic, k_z is the wavenumber along the axial direction, $\omega = 2\pi f$ is the temporal frequency, and $i = \sqrt{-1}$. Substituting (41) and (42) in the governing equations (37) to (40), results in an Eigenvalue problem,

$$\left(k_z^2\begin{bmatrix}\mathbf{K}_2^S & 0\\ 0 & \kappa\mathbf{K}_2^F\end{bmatrix}+\begin{bmatrix}\mathbf{K}_0^S-\omega^2\mathbf{M}^S & -\kappa\mathbf{C}_{SF}\\ -\omega^2\mathbf{C}_{SF}^T & \kappa\mathbf{K}_0^F\end{bmatrix}\right)\begin{Bmatrix}\boldsymbol{\phi}_S\\ \boldsymbol{\phi}_F\end{Bmatrix}=\begin{Bmatrix}0\\0\end{Bmatrix} \qquad (43)$$

where κ is the normalization factor to improve the conditioning of the system. The expression for κ can be found in (Roy and Guddati 2021). The solid-domain contribution matrices, $\mathbf{K}_2^S, \mathbf{K}_0^S, \mathbf{M}^S$, the fluid-domain contribution matrices, $\mathbf{K}_2^F, \mathbf{K}_0^F$, and the fluid-structure interaction matrix, $\mathbf{C}_{SF}$ are defined in (Vaziri Astaneh and Guddati 2017b). These contribution matrices depend on the geometry (inner radius and thickness) and the material properties (densities and shear modulus). The quadratic eigenvalue problem (43) is solved for each frequency ω, to result in the wavenumber k_z, resulting in the dispersion relationship. Consistent with the measured

dispersion curves (see Figure 4.4), the simulated dispersion curves are plotted as phase velocity ($c_p = \omega/k_z$) as a function of cyclic frequency ($f = \omega/2\pi$).

The special features of the forward model include (a) applying linear regular finite element with the selective reduced integration scheme to address the volumetric locking in the limit of incompressibility (Hughes 2012), (b) simulating the unbounded exterior fluid with perfectly matched discrete layers (Savadatti and Guddati 2010a). Note that the forward model still captures the full 3D wave propagation; the computational efficiency is facilitated by geometric features without sacrificing any accuracy (further details can be found in (Roy and Guddati 2021)).

PROBABILISTIC INVERSION

Our goal is to estimate not only the artery stiffness, also the associated uncertainty given the uncertainty in the measurement. Therefore the probabilistic inversion is best suited to address this goal. In the deterministic analysis (Roy *et al* 2021), we observed two parameters namely wall shear-modulus and thickness which are influential with the phase-velocity dispersions. The motivation behind including the wall thickness as parameter is because it is hard to measure reliably *in vivo* from the B-mode images due to the small length scale (a few pixels wide). The modulus is parametrized using a Spring-pot (viscoelastic) model, where the parameters are the fractional power (α) and modulus factor (G_0):

$$G = G_0(i\omega)^{\alpha} \tag{44}$$

The above parametrization is motivated by the Rheospectris measurements in Figure 4.2, where the model fits the experimental data very well. Of the two material parameters, the fractional power is assumed to be known, leading to two parameter inversion, i.e. (1) the modulus factor (G_0) and (2) wall thickness (h).

Further, since both are positive quantities, we parametrize using log functions. This leads us to the log-normal distribution of the original parameters, $q = [G_0, h]$. In addition to the uncertainty that propagates from the parameter uncertainty, the measured dispersion curve is assumed to have Gaussian noise. Thus, the probabilistic model for the dispersion relation takes the form,

$$\left(c_p\right)_i = c_p^s(\omega_i, q) + \epsilon_i, \text{ where } \epsilon \sim \mathrm{N}(\mu = 0, \sigma^2),\ i = 1, ..., n_\omega \tag{45}$$

Where ϵ is independent and identically distributed (iid) across various frequencies. c_p^s and c_p are simulated and measured phase-velocity dispersions respectively. n_ω is the number of (discrete) frequencies, and i is the frequency index.

In addition, we have data sets across several acquisitions and angular configurations. These data sets are independent to each other. In addition, in our experimental data, we observe higher variability across different angular configurations compared to variability across different frequencies within each data set. This violates the identically distributed assumption, leading us to proposed two different approaches to estimate the parameter uncertainty.

In the first approach, we first obtain the deterministic inversion results and then fit a kernel density using the parameter points obtained from the deterministic analysis. Here, we do not assume any distribution for the variability across different angular configurations. However, note that there is an unknown bandwidth parameter in the kernel density function. In this work, we employ the MATLAB *ksdensity* function with the default settings which consider the optimal bandwidth parameter for Gaussian distribution. With respect to the deterministic inversion analysis, we apply only the Interior point method with the BFGS Hessian model (Waltz *et al* 2006). We employ the MATLAB optimization *fmincon* function for this. With respect to the constraints in the optimization, we apply $\pm 30\%$ of the parameters' mean value as the simple bounds. To compute the gradient, the forward finite difference scheme is considered. The objective function used for deterministic inversion is,

$$F_{error} = \frac{\sum_{f_i=f_1}^{f_2}\left(c_2^s(f_i,q)-c^m(f_i)\right)^2 + \sum_{f_i=f_3}^{f_4}\left(c_1^s(f_i,q)-c^m(f_i)\right)^2}{\sum_{f_i=f_1}^{f_2}\left(c^m(f_i)\right)^2 + \sum_{f_i=f_3}^{f_4}\left(c^m(f_i)\right)^2}, \quad (46)$$

where, c_1^s and c_2^s are the simulated phase velocities corresponding to the modes 1 and 2, respectively, and c^m is the phase velocity from the measured data. As mentioned in (Roy *et al* 2021), $f_1 = 300$ *Hz,* $f_2 = 500$ *Hz,* $f_3 = 900$ *Hz,* and $f_4 = 1000$ *Hz.* These frequency windows are specific to phantom experiments; we may need to revisit them for *in vivo* experiments, as they may change depending on the geometry and material properties.

As an alternative, we apply a Frequentist Mixed Effect model (Demidenko 2013) where we consider two different Gaussian distributions, one to represent the noise across different frequencies within a given acquisition, and another to represent the variation across different acquisitions and angular configurations:

$$\begin{aligned} &c_{p,ij} = c_p^s(\omega_i, q_j) + \epsilon_{ij},\ \epsilon_{ij} \sim \mathrm{N}(0, \sigma_j^{\,2});\quad i = 1,...,n_\omega,\ j = 1,...,n_g \\ &q_j = \beta + b_j,\ b_j \sim \mathrm{N}(0, \Psi); \end{aligned} \tag{47}$$

Where, β is the fixed effect and b is the random effect of the inversion parameter q. Here, we employ the MATLAB *nlmefit* function to fit the mixed effect model. In the RESULTS AND DISCUSSIONS section, we present the results from both Mixed Effect and the kernel density approaches.

RESULTS AND DISCUSSIONS

One parameter case

In the single parameter case, we consider $q = [G_0]$ as the parameter. In addition, in the Mixed Effect model, we consider number of groups, $n_g = 60$,corresponding to 10 acquisitions for each of the 6 angular positions The results are shown in Figure 4.6 for the tube-1 and tube-7 data sets; both fixed and random effects are considered in Figure 4.6. In addition, the 95% confidence interval is also computed, and the corresponding results are presented in Figure 4.7 along with the measured data points. The reason we picked these two tubes is that we have observed typical patterns in the tube-1 whereas the tube-7 supports our assumption of homogeneity better than all other tubes. The compact dispersion curves for the tube-7 across different groups is visible in Figure 4.7. In both cases, the Kernel density approach resulted in bimodal results with peak probabilities at two different modulus values. After closer examination of the experimental specimens, we noted that there exists a mild crease associated with the mold, affecting the estimated modulus for some of the angles; we postulate this to be the reason for the bimodal distribution and do not expect similar feature when the approach is extended to future in vivo experiments. The mixed effect model is necessarily Gaussian, owing to the underlying assumption. While necessarily deficient in capturing the bimodal distribution, it is consistent with the Kernel density results, and it is expected that mixed effect model would be more consistent with Kernel density approach when extended to in vivo settings.

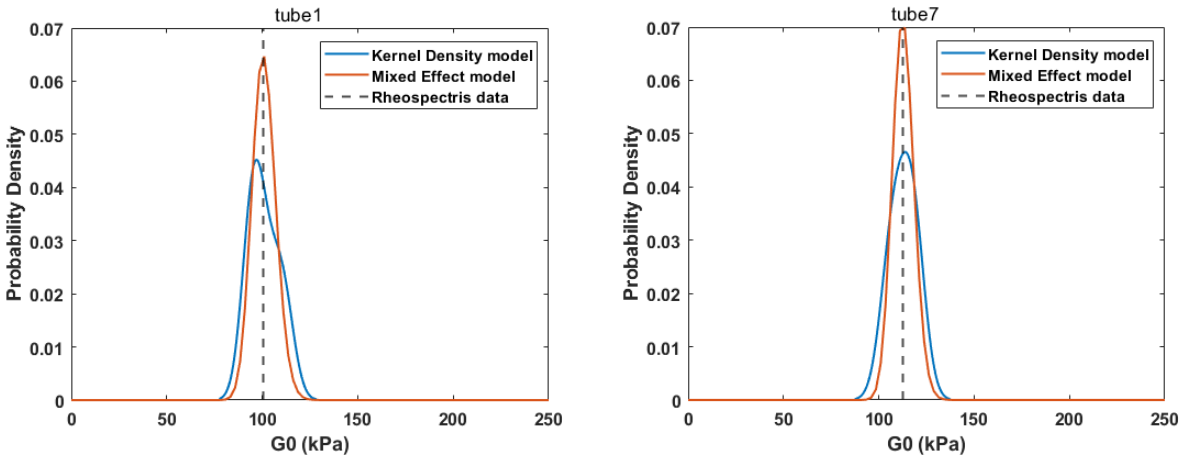

Figure 4.6 One parameter case: result for the tube-1 (left) and tube-7 (right) data sets.

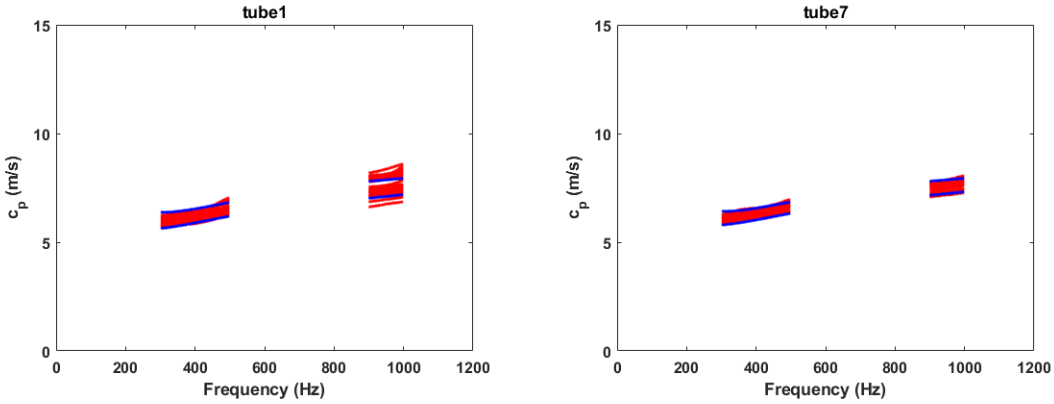

Figure 4.7 95% confidence intervals considering the parameter distribution in Figure 4.6 for the tube-1 (left) and tube-7 (right) data sets.

Two parameter cases

In the two parameter cases, we have the parameters to be thickness and modulus, $q = [h, G_0]$. The number of groups again is 60 (10 acquisitions for 6 angles). The results are shown in Figure 4.8 and Figure 4.9 for the tube-1 and tube-7 data sets respectively. Here also, both fixed and random effects are considered in Figure 4.8 and Figure 4.9. Note that with the thickness being an additional unknown, the uncertainty in the modulus parameter increases significantly. At this point, we have applied the Frequentist framework for both parameters. The Bayesian framework would be explored in the future, which would allow incorporating prior information on thickness from B mode images. We believe that incorporation of prior information on thickness, and the expected reduction in uncertainty is necessary to have a clinically meaningful modulus information.

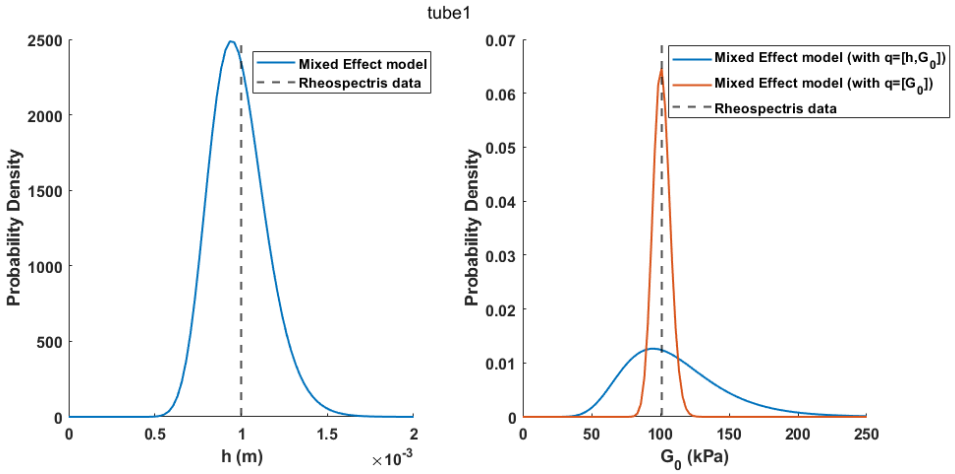

Figure 4.8 Two parameter case: result for the tube-1 data set.

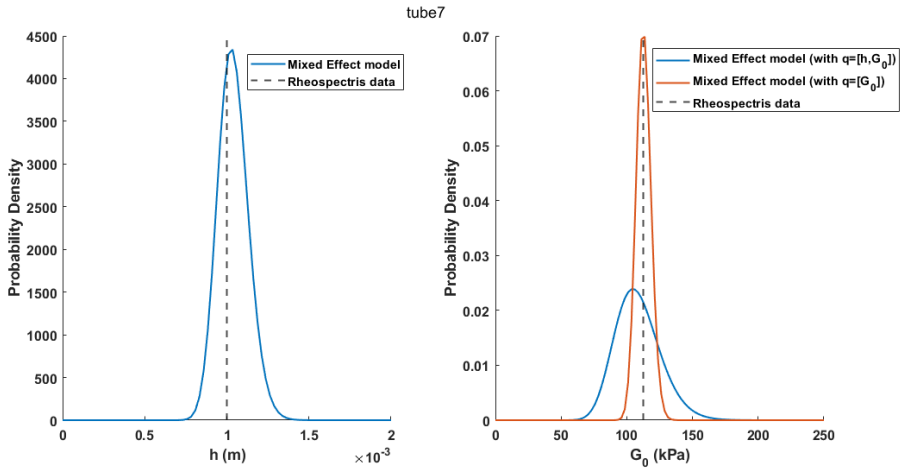

Figure 4.9 Two parameter cases result for the tube-7 data set.

CONCLUSIONS AND NEXT STEP

In this chapter, we present a preliminary probabilistic framework for the arterial modulus inversion. The proposed models are the extension of our earlier work on the deterministic inversion. At this time, we suggest utilizing the Mixed Effect model in the Frequentist framework for the probabilistic inversion for modulus alone. Although the Frequentist approach is computationally efficient, it suffers from its inability to easily incorporate prior probabilities, which is available for thickness (in vivo setting, the thickness is not known precisely, but good prior distribution can be obtained from B-mode images). To incorporate this prior distribution, a Bayesian mixed effect framework would be explored in the future.

CHAPTER 5: FULL WAVE SIMULATION OF ARTERIAL RESPONSE UNDER ACOUSTIC RADIATION FORCE

ABSTRACT

In biomedical imaging, the responses of an incompressible hollow cylindrical waveguide can be utilized to characterize the material properties of tube-shaped organs such as carotid artery. To do so in a computationally efficient manner, this chapter provides a methodology which synthesizes a few existing approaches such as modal analysis with recent techniques such as Semi-Analytical Finite Element method. The resulting model returns the full wave (tube) responses in 3D space and time for the given excitation, geometric and material properties. The proposed approach can consider any viscoelastic model, but for illustration purposes, two representative viscoelastic models for arterial waveguide are considered, namely Voigt model (linear viscoelastic damping) and Spring-pot model. To verify the full wave model, convergence analysis is performed which shows a few wave modes are sufficient to capture the dynamics of the problem with engineering accuracy.

INTRODUCTION

Guided wave inversion is often used to characterize the tube-like structures (Rose 2014). It is the process where the material and geometric properties of the tube can be back-calculated either from the wave dispersion in the wavenumber-frequency domain or from the wall motion in space-time domain. An important recent application of guided wave inversion is in the biomedical imaging where the goal is to characterize the nearly incompressible soft tissue surrounded by softer fluid-like tissue (Astaneh *et al* 2017). With the motivation of increasing the practicality of guided wave inversion with space-time data, we develop a methodology to compute the tube wall motion in space-time for the given excitation, geometry, and material properties. This can certainly be addressed through the 3D finite element formulation, but would be computationally very expensive. Instead, we attain computational efficiency through utilizing some traditional and some recent techniques for tube like structures immersed in an incompressible fluid. Our work is particularly focused on modeling wave propagation from acoustic radiation force (ARF) excitation on human carotid artery, but the methodology is general and useful to similar settings in other applications.

Several analytical formulations (Thomson 1950, Haskell 1953, Knopoff L. 1964, Randall 1967, Lowe 1995, Berliner and Solecki 1996, Sato and Ogiso 2013) are available for elastic and

acoustoelastic waveguides (elastic waveguides immersed in acoustic fluid) but they are limited to simple geometries. Computational simulation is often necessary when the geometry, boundary conditions or the material properties are more complicated. Among the variants of the finite element methods, we consider the *Semi-Analytical Finite Element* (SAFE) method (see e.g. (Datta *et al* 1988, Gavrić 1995, Gry 1996, Han *et al* 2001, Hayashi *et al* 2003, Taweel *et al* 2000, Kausel 1986)). The idea of SAFE method is to utilize analytical formulation in a few direction(s) while the finite element discretization in the remaining direction(s), hence the name Semi-Analytical Finite Element method. SAFE method can be utilized effectively to model wave propagation in carotid artery, where the material properties along the axial and azimuthal directions can be assumed to be homogeneous. Essentially, we employ Fourier expansion in axial and azimuthal directions, and finite element discretization is used only in the radial direction. This makes the waveguide model extremely efficient compared to traditional 3D finite element models.

For finite element discretization in the radial discretization, we adapt (1) the classical idea of linear elements with selective reduced integration for the incompressible solid medium, (2) regular linear elements for the inner incompressible fluid, (3) Perfectly Matched Discrete Layers (PMDL) for incompressible outer fluid.

The discrete dynamical systems resulting from SAFE discretization is solved using modal superposition where a few modes are shown to be sufficient to capture the dynamics of the system. For simpler Voigt model, we can solve the resulting single-degree-of-freedom (SDOF) problem using convolution with impulse response function (Green's function in the time domain), resulting in an extremely efficient simulation methodology. For more complicated fractional viscoelastic models, we solve the problem using the frequency response function formalism, which tends to be more expensive, but still practical.

In the remainder of the chapter, we first present the governing differential equations, interface and boundary conditions that represent the physics of the problem. Next, the proposed methodology is described. In the following section, numerical examples are presented to examine the convergence of the methodology, leading to recommended discretization parameters for the carotid artery problem. Finally, we close the chapter with some concluding remarks on the proposed methodology and future work.

PROBLEM STATEMENT

The carotid artery is made of biological tissue with pressure wave velocity is two orders of magnitude larger than the shear wave velocity, and the contrast is even higher for the surrounding tissue and blood, where the shear wave velocity is much smaller. Given this, the artery can be approximated as an incompressible cylindrical waveguide filled with and immersed in incompressible inviscid fluids. The schematic of the model is shown in Figure.5.1. The governing differential equation for the solid medium is the Elastodynamic equation, written here in the frequency domain:

$$\mathbf{L}_{\sigma}^{T}\boldsymbol{\sigma} + \rho\frac{\partial^2 \mathbf{u}}{\partial t^2} = \mathbf{f}, \text{ in } \Omega_S \ , \tag{48}$$

where the primary variable in the solid domain (Ω_S) is the displacement vector, $\boldsymbol{u} = \boldsymbol{u}(r,\theta,z,t)$ with 3 components, i.e. $\boldsymbol{u} = \{u_r, u_\theta, u_z\}^T$. $\boldsymbol{\sigma} = \lambda * \text{tr}(\boldsymbol{\epsilon})I + 2G * \boldsymbol{\epsilon}$ is the stress tensor, where, $\boldsymbol{\epsilon}$ is the strain tensor (written in vector form), and $\boldsymbol{\epsilon} = \mathbf{L}_{\epsilon}\boldsymbol{u} = \{\epsilon_{rr}, \epsilon_{\theta\theta}, \epsilon_{zz}, \epsilon_{\theta z}, \epsilon_{rz}, \epsilon_{r\theta}\}^T$. The symbol $*$ denotes the convolution operator. In the limit of incompressibility, the Lamé parameter, λ approaches infinity, but the shear modulus operator G is finite. This time dependent shear modulus depends on the choice of the viscoelastic model. For the Voigt model, the modulus can be written in the operator form as,

$$G(t) = G_0\left(1 + \beta\frac{\partial}{\partial t}\right), \tag{49}$$

where G_0 is the elastic modulus and β is the Rayleigh damping coefficient. For fractional model such as spring-pot model, this can be formally written as,

$$G(t) = G_0\left(\frac{\partial^{\alpha}}{\partial t^{\alpha}}\right), \tag{50}$$

where α is the fractional order and G_0 is modulus factor. The 6×3 gradient operators, $\mathbf{L}_{\sigma}$ and $\mathbf{L}_{\epsilon}$, are,

$$\mathbf{L}_{\epsilon} = \mathbf{L}_r \frac{\partial}{\partial r} + \mathbf{L}_\theta \frac{1}{r}\frac{\partial}{\partial \theta} + \frac{1}{r}\mathbf{L}_0 + \mathbf{L}_z \frac{\partial}{\partial z},$$
$$\mathbf{L}_{\sigma} = \mathbf{L}_r \frac{1}{r}\frac{\partial(.\times r)}{\partial r} + \mathbf{L}_\theta \frac{1}{r}\frac{\partial(.)}{\partial \theta} + \mathbf{L}_z \frac{\partial(.)}{\partial z} - \mathbf{L}_0 \frac{1}{r}. \quad (51)$$

The operators $\mathbf{L}_r, \mathbf{L}_\theta, \mathbf{L}_z,$ and $\mathbf{L}_0$ are given in (Roy and Guddati 2021). The acoustic radiation force vector is $\mathbf{f} = \mathbf{f}(r,\theta,z,t)$. The density of the solid medium is ρ.

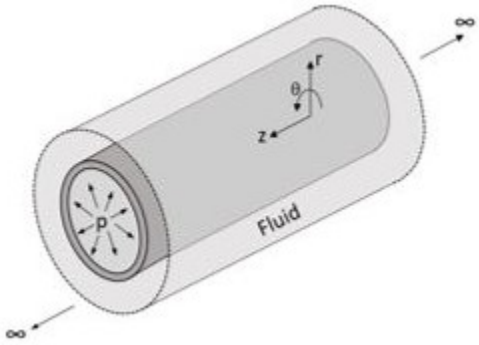

Figure.5.1 Geometry of the immersed tube

For the fluid domain, in the limit of incompressibility, the acoustic wave equation becomes the Laplace equation,

$$\nabla^2 p = 0 \text{ in } \Omega_F \ , \quad (52)$$

where the primary variable in the fluid domain (Ω_F) is the pressure, $p = p(r,\theta,z,\omega)$. The Laplace operator in cylindrical coordinate systems is, $\nabla^2(\cdot) = r^{-1}\partial(r\partial(\cdot)/\partial r)/\partial r + r^{-2}\partial^2(\cdot)/\partial\theta^2 + \partial^2(\cdot)/\partial z^2$. The conditions at the solid-fluid interfaces Γ_{SF} are the stress continuity:

$$\boldsymbol{\sigma}\cdot\mathbf{n}_s - p\mathbf{n}_F = 0, \text{ on } \Gamma_{SF} \ , \quad (53)$$

and the continuity of the normal displacement, equivalently acceleration:

$$\frac{\partial^2 \mathbf{u}}{\partial t^2}\cdot\mathbf{n}_s - \frac{1}{\rho_F}\frac{\partial p}{\partial \mathbf{n}_F} = 0, \text{ on } \Gamma_{SF}. \quad (54)$$

$\mathbf{n}_s$ and $\mathbf{n}_F = -\mathbf{n}_S$ are the unit vectors for solid and fluid domains respectively. ρ_F is the fluid density.

Given the tube geometry, applied loading, and material properties of the tube and inside and outside fluids, our objective is to compute the tube wall velocity in the spatiotemporal domain. The proposed steps are detailed in the following section.

METHODOLOGY

We solve the above problem in 4 steps: (1) initial decoupling and discretization of the differential equation using the Semi-Analytical Finite Element (SAFE) method and Perfectly Matched Discrete Layers (PMDL), (2) further decoupling into single-degree-of-freedom systems through modal analysis, (3) finding the temporal response for each mode, and (4) computing the final response in space-time by superimposing all the modal responses. The details of each steps are presented in the following subsections.

SAFE and PMDL framework

Owing to the invariant geometry and material properties along the axial and azimuthal direction of the tube, we utilize Fourier expansion in these two directions and employ finite element discretization in the radial direction. This leads us to the utilization of the Semi-Analytical Finite Element (SAFE) method (Kausel and Peek 1982, Tassoulas and Kausel 1983, Kausel 1986). For the surrounding unbounded fluid, we consider Perfectly Matched Discrete Layers (PMDL, (Guddati and Lim 2006, Guddati *et al* 2008).

Facilitated by the Fourier expansions in the axial and azimuthal directions, the resulting discretized displacement takes the form,

$$\mathbf{u}(r,\theta,z,t) = \mathbf{N}_S(r)\begin{bmatrix} \overline{u_r}(t)\cos(m\theta) \\ \overline{u_\theta}(t)\sin(m\theta) \\ \overline{u_z}(t)\cos(m\theta) \end{bmatrix} e^{-ik_{nm}z} \quad . \qquad (55)$$

In the fluid medium, the discretized pressure variable becomes,

$$p(r,\theta,z,t) = \mathbf{N}_F(r)\overline{p}(t)cos(m\theta)e^{-ik_{nm}z}, \qquad (56)$$

where m is the circumferential Fourier number, k is the wavenumber along the axial direction (z). $\mathbf{N}_S$ and $\mathbf{N}_F$ are the finite element shape functions in the solid and fluid domain, respectively. For the solid medium, the discretized form of the Elastodynamic equation (48) is,

$$\int_\Omega \mathbf{B}^T \mathbf{D}\mathbf{B} r dr d\theta - \int_\Gamma \mathbf{N}_S{}^T \left(\mathbf{D}\mathbf{L}_\epsilon \mathbf{N}_S\right).r_\Gamma d\theta = \int_\Omega \mathbf{N}_S{}^T \mathbf{f} r dr d\theta \quad ,(57)$$

where $\mathbf{D}$ is constitutive matrix, i.e. $\boldsymbol{\sigma} = \mathbf{D}\boldsymbol{\epsilon}$. The matrix $\mathbf{B}$ is,

$$\mathbf{B} = \mathbf{L}_r \frac{\partial \mathbf{N}_S}{\partial r} + \tilde{\mathbf{L}}_\theta \frac{\mathbf{N}_S}{r} + \frac{\mathbf{N}_S}{r}\mathbf{L}_0 + \mathbf{L}_z \mathbf{N}_S \left(-ik_{nm}\right) \quad (58)$$

Where the matrix, $\tilde{\mathbf{L}}_\theta = \mathbf{L}_\theta m \begin{bmatrix} -\sin(m\theta) & 0 & 0 \\ 0 & \cos(m\theta) & 0 \\ 0 & 0 & -\sin(m\theta) \end{bmatrix}$. Equation (58) is rewritten as,

$$\mathbf{B} = \mathbf{B}_r + \mathbf{B}_\theta + ik_{nm}\mathbf{B}_z \ , \quad (59)$$

where $\mathbf{B}_r = \mathbf{L}_r \frac{\partial \mathbf{N}_S}{\partial r}$, $\mathbf{B}_\theta = \tilde{\mathbf{L}}_\theta \frac{\mathbf{N}_S}{r} + \frac{\mathbf{N}_S}{r}\mathbf{L}_0$, and $\mathbf{B}_z = -\mathbf{L}_z \mathbf{N}_S$. Therefore, the first term (stiffness matrix) in equation (57) becomes,

$$\begin{aligned} \mathbf{K} &= \int_\Omega \left(\left(\mathbf{B}_r + \mathbf{B}_\theta\right) + ik_{nm}\mathbf{B}_z\right)^T \mathbf{D}\left(\left(\mathbf{B}_r + \mathbf{B}_\theta\right) + ik_{nm}\mathbf{B}_z\right) r dr d\theta \\ &= \int_\Omega \left(\mathbf{B}_r + \mathbf{B}_\theta\right)^T \mathbf{D}\left(\mathbf{B}_r + \mathbf{B}_\theta\right) r dr d\theta \\ &\quad + ik_{nm}\left(\int_\Omega \left(\mathbf{B}_r + \mathbf{B}_\theta\right)^T \mathbf{D}\mathbf{B}_z r dr d\theta - \int_\Omega \mathbf{B}_z^T \mathbf{D}\left(\mathbf{B}_r + \mathbf{B}_\theta\right) r dr d\theta\right) \quad (60) \\ &\quad + k_{nm}^2\left(\int_\Omega \mathbf{B}_z^T \mathbf{D}\mathbf{B}_z r dr d\theta\right) \\ &= \mathbf{A} + ik_{nm}\mathbf{B} + k_{nm}^2 \mathbf{C} \end{aligned}$$

The interface term, i.e. second term in Equation (57) can be rewritten as,

$$\int_\Gamma \mathbf{N}_S{}^T \left(\mathbf{D}\mathbf{L}_\epsilon \mathbf{N}_S\right).r_\Gamma d\theta = \int_\Gamma \mathbf{N}_S{}^T \mathbf{N}_F \mathbf{n}_F r_\Gamma d\theta \, . \quad (61)$$

The discretized form of Equation (54) (Laplace equation) after incorporating the interface condition is,

$$\int_{\Omega} \mathbf{B}_F{}^T \mathbf{B}_F r dr d\theta - \int_{\Gamma} \mathbf{N}_F^T \cos(m\theta) \rho_F \mathbf{N}_S \frac{\partial^2}{\partial t^2} \cdot \mathbf{n}_s r_\Gamma d\theta = 0 \quad , (62)$$

where $\mathbf{B}_F = \left[\cos(m\theta), \sin(m\theta), \cos(m\theta)\right] \left[\frac{\partial \mathbf{N}_F}{\partial r}, -m\frac{\mathbf{N}_F}{r}, -ik_{nm}\mathbf{N}_F \right]^T$.

Since $\int_\theta \cos(m\theta)\sin(m\theta) d\theta = 0$, the off-diagonal terms in the first term of the equation (62) are zero. Therefore, the stiffness matrix from the first term of equation (62) is,

$$\begin{bmatrix} \int_r \left(\frac{\partial \mathbf{N}_F}{\partial r}\right)^T \left(\frac{\partial \mathbf{N}_F}{\partial r}\right) r dr & 0 & 0 \\ 0 & m^2 \int_r \frac{1}{r^2} \mathbf{N}_F^T \mathbf{N}_F r dr & 0 \\ 0 & 0 & -k_{nm}^2 \int_r \mathbf{N}_F^T \mathbf{N}_F r dr \end{bmatrix} \quad (63)$$

Modal Analysis

We start with the system of evolution equations resulting from the above SAFE framework,

$$\left(\mathbf{K} + \mathbf{M} \frac{\partial^2}{\partial t^2} \right) \mathbf{u}(r,k,m,t) = \mathbf{f}(r,k,m,t), \quad (64)$$

where $\mathbf{K}$ and $\mathbf{M}$ are the stiffness and mass matrices respectively. m is the circumferential Fourier number and k is the wavenumber of the axial direction z as described in the previous section. Given the applied excitation $\mathbf{f}(r,k,m,t)$, our objective is to compute the displacement $\mathbf{u}(r,k,m,t)$. Among the existing approaches to solve the above dynamical system, we choose the modal analysis we hypothesize, and later confirm that a few modes are sufficient to simulate this thin wall problem. The modes are computed from the associated Eigenvalue problem:

$$\left(\mathbf{K} + \mathbf{M} \frac{\partial^2}{\partial t^2} \right) \mathbf{\Phi}(r,k,m) = 0, \quad (65)$$

where $\mathbf{\Phi}$ is the matrix containing mode shapes. The resulting deformation $\mathbf{u}$ can be computed through superimposing all the modal responses:

$$\mathbf{u}(r,k,m,t) = \Phi\Gamma = \sum_{i=1}^{N} \gamma_i(t)\boldsymbol{\phi}_i(r,k,m)\,, \tag{66}$$

where N is the total number of the normal modes. Substituting Equation (66) into the Equation (64), and utilizing orthogonality property of the modes, we obtain the governing equation for the i^{th} modal participation factor γ_i:

$$k_i\gamma_i + m_i\frac{\partial^2\gamma_i}{\partial t^2} = \boldsymbol{\phi}_i^T\mathbf{f}\ , \tag{67}$$

where, $k_i = \boldsymbol{\phi}_i^T\mathbf{K}\boldsymbol{\phi}_i$, and $m_i = \boldsymbol{\phi}_i^T\mathbf{M}\boldsymbol{\phi}_i$ are the modal stiffness and mass respectively.

Temporal response

In the case of Voigt model, we can directly apply convolution of impulse response (Green's) function with the modal force, to result in the time history for each modal participation factor. The impulse response function for the SDOF displacement and velocity are,

$$\begin{aligned} IRF_u(t) &= \frac{1}{m\omega_d}\sin(\omega_d t)e^{\omega_n t}, \\ IRF_v(t) &= \frac{1}{m\omega_d}\left(\cos(\omega_d t) + \omega_n\sin(\omega_d t)\right)e^{\omega_n t}, \end{aligned} \tag{68}$$

Where, ω_n is the natural frequency obtained after solving the Eigenvalue problem in Equation (65). ω_d is the damped natural frequency,

$$\omega_d = \omega_n\sqrt{1-\xi^2}\ . \tag{69}$$

Responses due to an arbitrary applied force is,

$$\begin{aligned} u(t) &= \int_0^t f_t(\tau)IRF_u(t-\tau)d\tau, \\ v(t) &= \int_0^t f_t(\tau)IRF_v(t-\tau)d\tau, \end{aligned} \tag{70}$$

where f_t is the modal force.

In contrast with the Voigt model, for the general viscoelastic model such as Spring-pot model, due to the absence of analytic impulse response function, we utilize the frequency response

function (FRF) framework to obtain the responses. Essentially, the force is Fourier transformed into frequency domain and multiplied by the FRF (inverse of the dynamic stiffness) to obtain response as a function of frequency. Inverse Fourier transform is the utilized to obtain the time-domain response.

Final space-time response

The wavenumber-time (k-t) representation of the wall response is first obtained by superposition of the temporal response of all the modes:

$$\mathbf{u}(r,k,t)=\sum_{m=0}^{M}\sum_{i=1}^{N} v_{im}(t)(\boldsymbol{\phi}_{im}{}^{T}\mathbf{f}_{km})\,\boldsymbol{\phi}_{im}\left[\cos(m\theta),\sin(m\theta),\cos(m\theta)\right]^{T} \quad .(71)$$

We then apply the Inverse Fourier transform in the axial direction to obtain the final space-time response.

CONVERENCE STUDY AND RECOMMENDATIONS

To mimic ARF excitation that is sharp in the axial direction and somewhat spread out in the azimuthal direction ((Doherty *et al* 2013)), we consider the excitation force to vary in (Z,θ) as Gaussian,

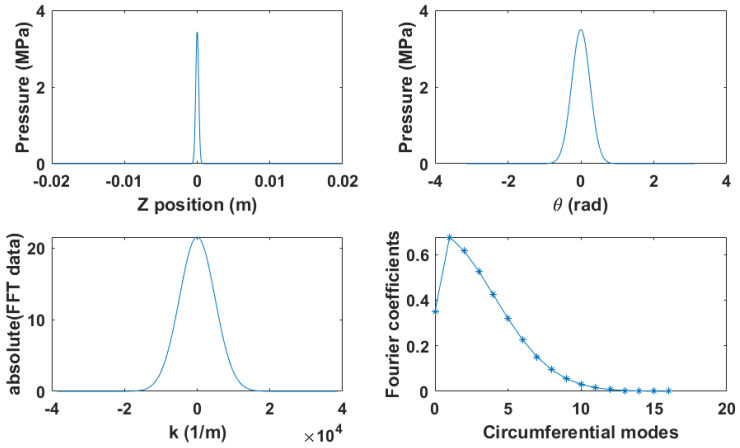

Figure.5.2 Applied excitation force (pressure) in the axial direction (Z) is shown in (left-top); the corresponding Fourier transformed data is presented in (left-bottom); the excitation force in circumferential (θ) direction pressure is shown in (right-top) and the corresponding Fourier coefficients are presented in (right-bottom).

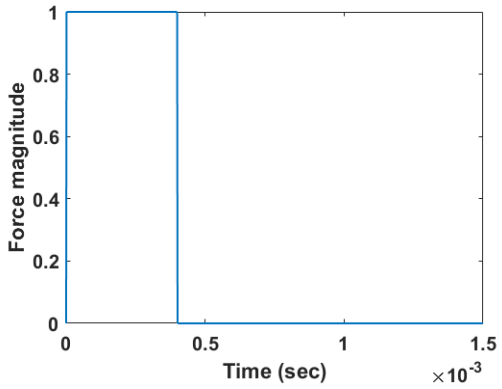

Figure.5.3 Acoustic Radiation Force history

Which is plotted in Figure.5.2. Again, consistent with the ARF excitation, the temporal variation is assumed to be rectangular, as shown in Figure.5.3 The variation of the force within the wall in the radial direction is assumed to be uniform. To mimic the human carotid artery, we consider cylindrical tube with a wall thickness of 1 mm, an inner radius of 3 mm. The density is assumed to be 1000 kg/m^3 for both solid and fluid media. The two viscoelastic models are considered for the wall material: (a) Voigt model with elastic modulus of 300 kPa and the damping ratio of 0.125 and (b) spring-pot model with the modulus factor at 600 Hz of 300 kPa and the fractional order, α, of 0.15. The frequency dependent shear moduli are presented in Figure.5.4. With respect to the discretization, we employ 20 linear finite elements for both solid and inside fluid and 8 PMDL divisions for outside fluid along the radial direction. As will be shown later, this discretization is shown to result in engineering accuracy of 1% based on convergence analysis presented below. The full wave results are presented in Figure.5.5.

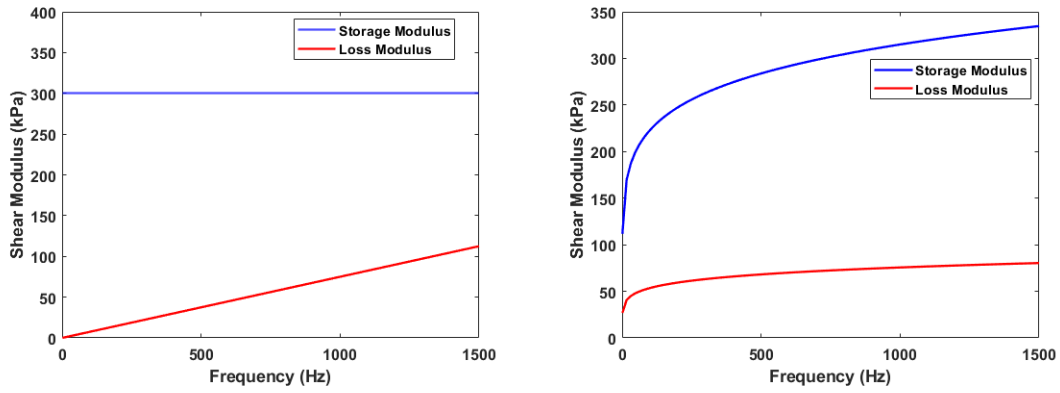

Figure.5.4 Input shear moduli corresponding to the Voigt model (left) and the spring-pot model (right).

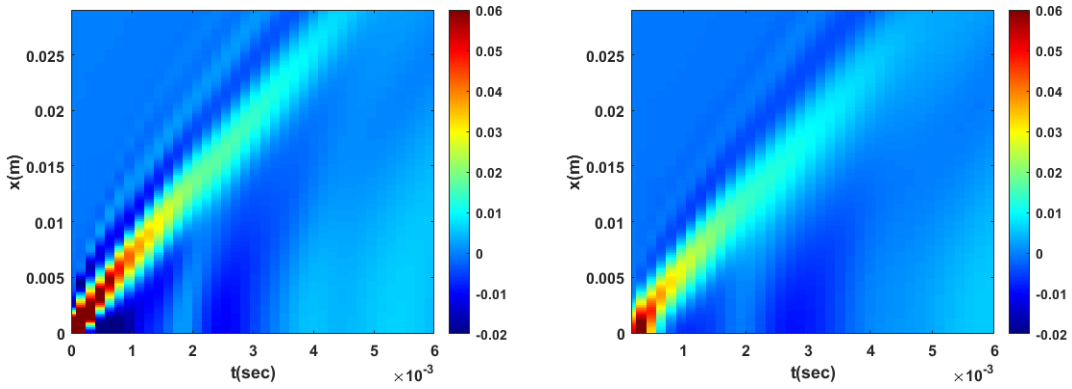

Figure.5.5 Full wave results from the Voigt model (left) and the spring-pot model (right)

Circumferential mode convergence

In Figure.5.6, the full wave results with increasing number of circumferential modes are presented. The corresponding normalized error is presented in Figure.5.7. Here the normalized error is computed as,

$$E_i^m = \frac{\| v(m=0:12) - v(m=0:i) \|_2}{\| v(m=0:12) \|_2}, \qquad (72)$$

where the i^{th} error E_i^m is the relative difference between the reference velocity $v(m=0:12)$, obtained using 12 circumferential modes, and the velocity $v(m=0:i)$ by considering the circumferential modes up to i, . As shown in Figure.5.7, with the first 10 circumferential modes, we achieve the normalized error around 1.e-4, which represents more than sufficient accuracy for all practical purposes. For an engineering accuracy of 1%, the first six modes, i.e. till n=5 appear to be sufficient.

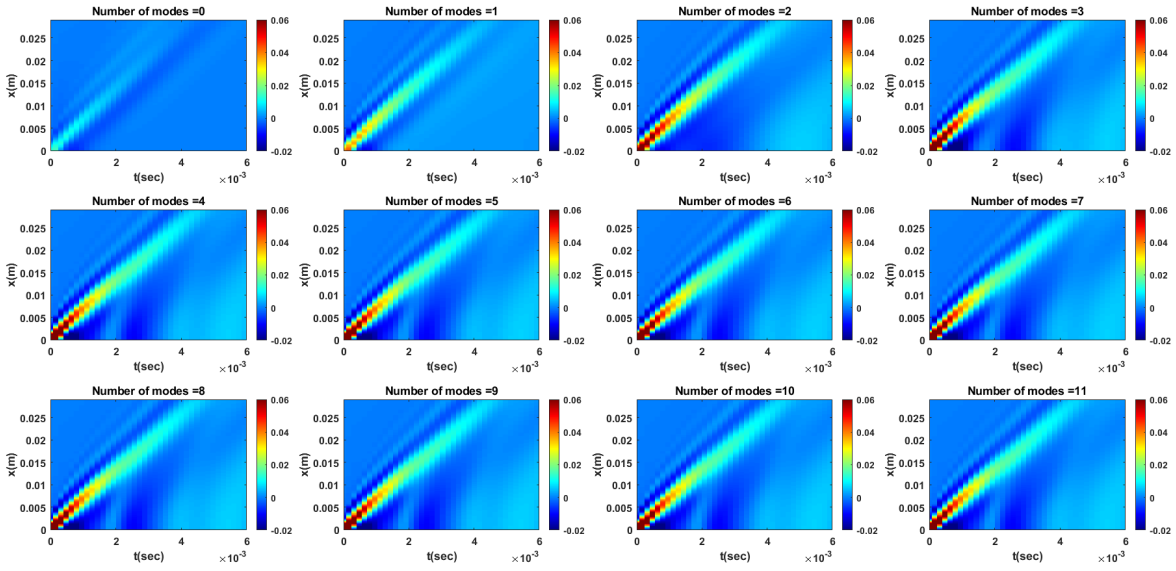

Figure.5.6 Full-wave results with increasing circumferential modes

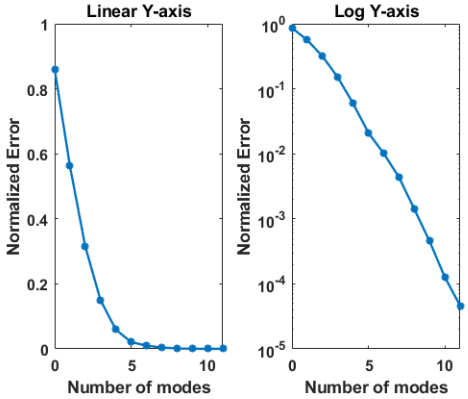

Figure.5.7 The circumferential mode convergence: (a) on linear scale; (b) on semi-log scale.

Solid domain mesh convergence

The convergence of the response due to the mesh sizes in the solid medium is presented in this section. The normalized error is,

$$E_i^d = \frac{\| v(d=28) - v(d=i) \|_2}{\| v(d=28) \|_2}, \qquad (73)$$

where d is the number of radial divisions in the solid domain, where the velocity for $d = 28$ is considered as the reference solution. The number of radial divisions for the interior and exterior fluid domains are chosen as 20 and 8 respectively. Figure.5.8 shows the velocity with

varying mesh sizes of the solid medium. The convergence result is presented in Figure5.9, which indicates that 20 radial divisions are sufficient for an engineering accuracy of 1%.

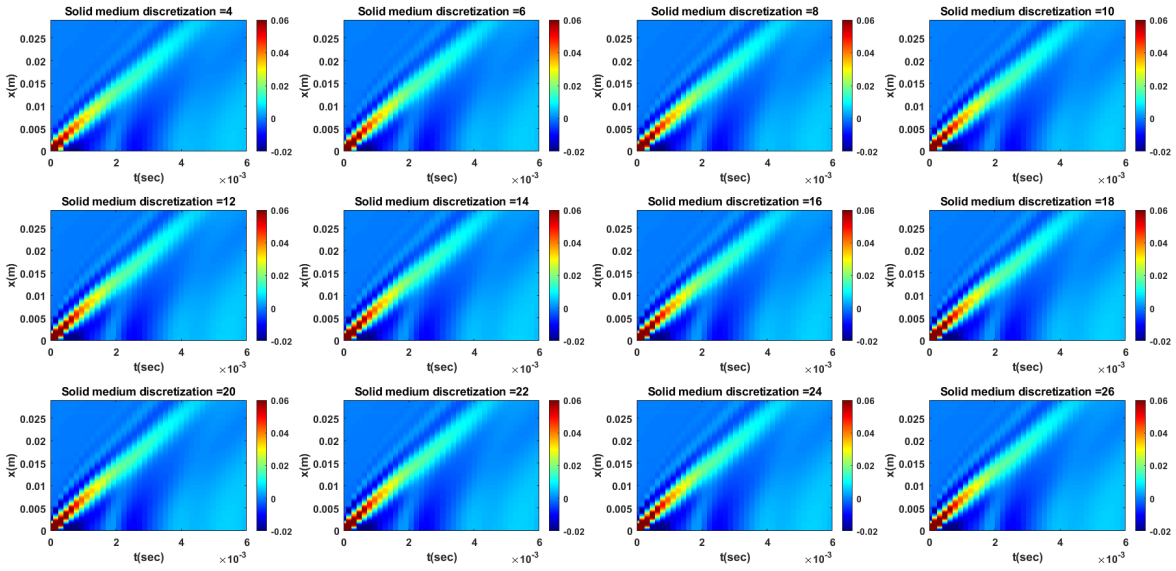

Figure.5.8 Full-wave results with varying discretization of solid medium

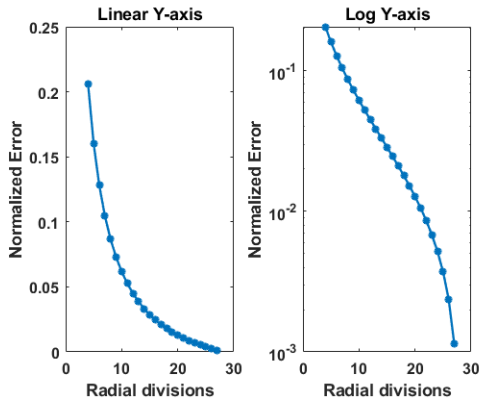

Figure5.9 The solid medium discretization convergence results - (a) on linear Y-axis; (b) on logarithm Y-axis

Inner fluid mesh convergence

The mesh convergence study is also performed for the interior fluid domain by examining the relative error,

$$E_i^d = \frac{\| v(d=27) - v(d=i) \|_2}{\| v(d=27) \|_2}, \qquad (74)$$

where d is the number of radial divisions in the interior fluid domain, where the velocity for $d = 27$ is considered as the reference solution. 20 elements are utilized for the wall and 8 elements are used for the exterior fluid domain. Figure.5.10 shows the velocity with varying mesh sizes. The convergence result is presented in Figure.5.11, indicating that 20 divisions are sufficient for the interior fluid domain, to achieve an engineering accuracy of 1%.

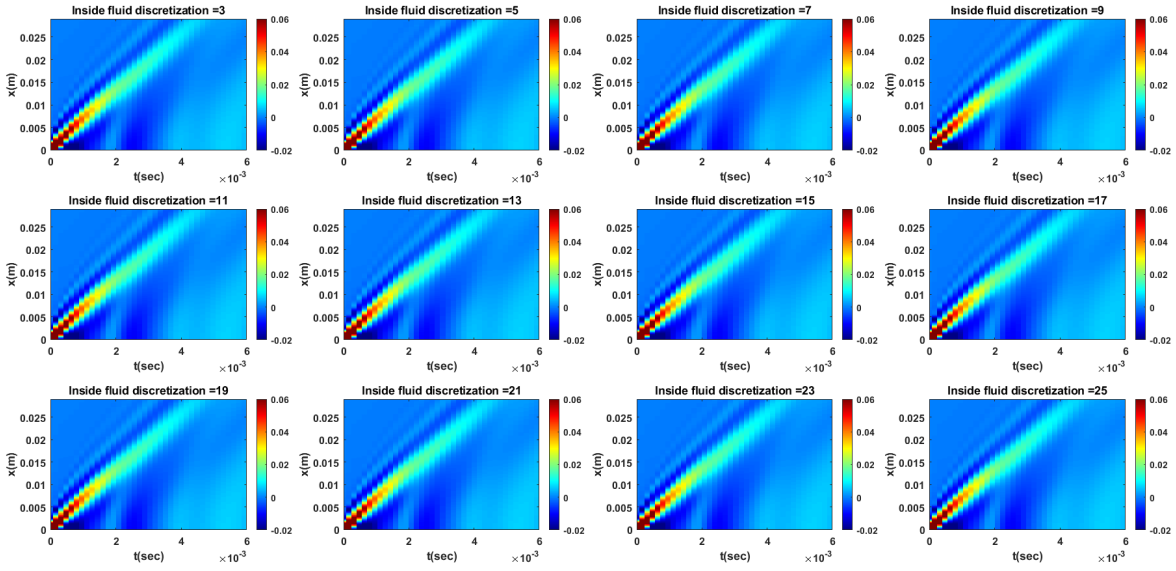

Figure.5.10 Full-wave results with varying discretization of inside fluid domain

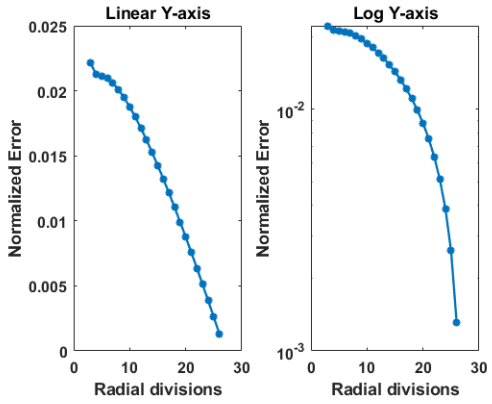

Figure.5.11 The inside fluid domain discretization convergence results - (a) on linear Y-axis; (b) on logarithm Y-axis

Outer fluid (PMDL) mesh convergence

In this section, the mesh convergence is performed only for the outside fluid domain (PMDL). Although the geometric progression ratio affects PMDL accuracy, we considered a lower progression ratio of 1.5, and considered only the effects of number of elements. The normalized error is defined as,

$$E_i^{\,d} = \frac{\| v(d=15) - v(d=i) \|_2}{\| v(d=15) \|_2} \tag{75}$$

Where d is the number of PMDL elements, with the velocity at $d=15$ is considered as the reference solution. The number of radial divisions in both solid and inside fluid mediums is chosen as 20. Figure.5.12 shows the velocity with varying mesh sizes of the solid medium. The convergence result is presented in Figure.5.13, indicating that eight PMDL elements are sufficient to achieve the engineering accuracy of 1%.

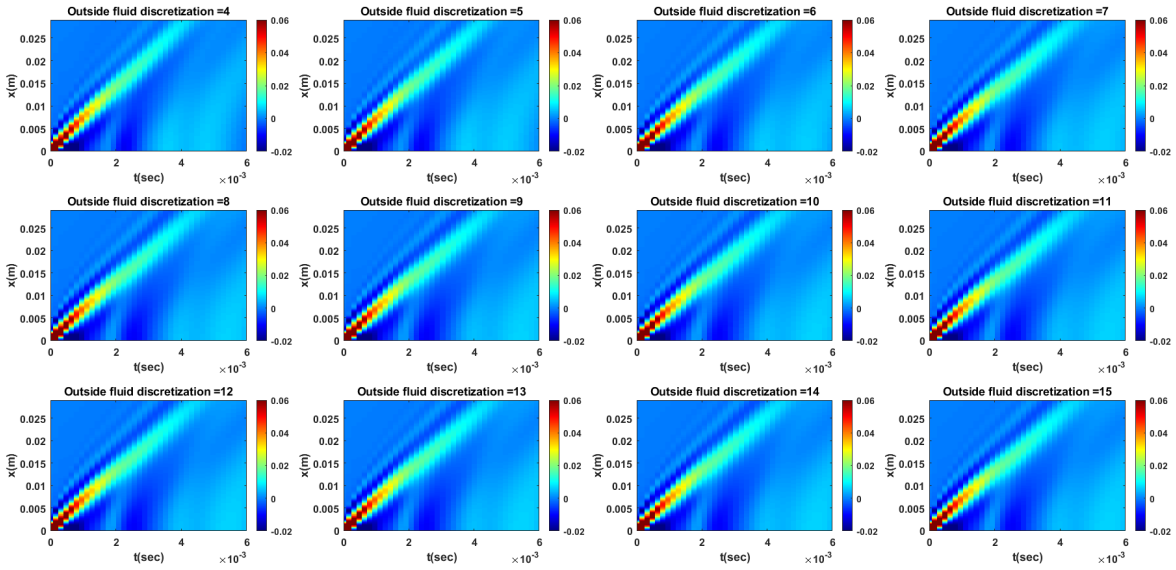

Figure.5.12 Full-wave results with varying discretization of outside fluid domain

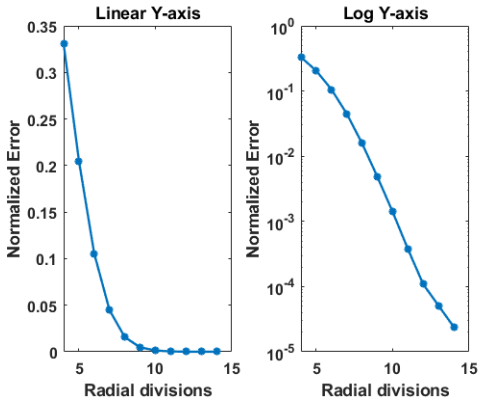

Figure.5.13 The outside fluid domain discretization convergence results - (a) on linear Y-axis; (b) on logarithm Y-axis

Normal mode convergence

In this section, we study the convergence of the normal modes considered. With respect to the reference solution, we consider all the normal modes. The number of total normal modes depend on the number of total degrees of freedom considered. The normalized error is computed using equation (76). The convergence result is presented in Figure.5.14. As observed, with first 23 modes are sufficient to satisfy the engineering accuracy of 1%.

$$E_i^{\,d} = \frac{\| v(d=62) - v(d=i) \|_2}{\| v(d=62) \|_2} \qquad (76)$$

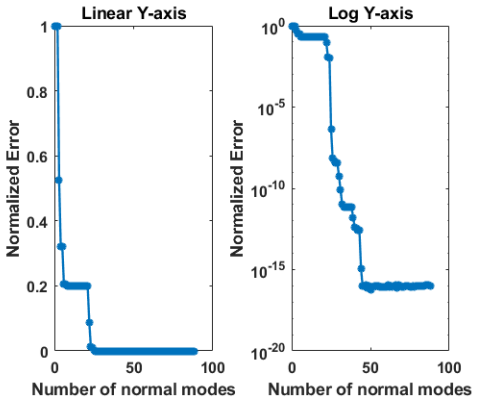

Figure.5.14 The normal mode convergence results - (a) on linear Y-axis; (b) on logarithm Y-axis.

Recommended Discretization Parameters

To summarize, based on the above convergence analyses, for an engineering accuracy of 1%, it appears sufficient to use circumferential modes 0-5, 20 elements in the solid domain, 20 elements in the fluid domain and 8 PMDL elements, with 23 normal modes to obtain the spatiotemporal representation of the wall motion.

CONCLUSIONS

In this chapter, we present a computationally efficient framework to compute the wall motion of an axisymmetric tube immersed in fluid given the applied acoustic radiation push. We utilize Semi-Analytical Finite Element framework due to its invariant geometry and material properties along the axial and azimuthal directions. In addition, given the thin-wall structure, we consider only a few initial mode contributions which allows us to employ modal analysis. For Voigt viscoelastic material model, we apply the impulse response function in time domain that further improves the computation time. For general viscoelastic models, we utilize the frequency-response-function approach to compute the response history for each mode. In the case of Voigt model, a single simulation takes less than 15 seconds with 7 parallel cores on standard desktop computer, and for the spring-pot fractional model, it takes less than 15 minutes. The computational cost can be reduced further by employing techniques such Padé approximation, which are subjects of future investigations.

CHAPTER 6: FULL WAVE INVERSION FOR ARTERIAL VISCOELASTICITY

ABSTRACT

Arterial viscoelasticity is an influential parameter towards estimation of arterial stiffness, a key biomarker for many cardiovascular diseases. In shear wave elastography (SWE) based guided wave model, phase-velocity dispersion is utilized to estimate elastic modulus. However, the phase velocity is not influenced by the viscoelasticity for this waveguide model and cannot be used to estimate viscoelasticity. In addition, existing rheological-based and model free approaches which work well for bulk organs, fail for boundary sensitive organs such as artery. To address this gap, this chapter provides a new framework to back-calculate the arterial viscoelasticity. The underlying idea is to match the SWE motion data with simulated full-wave data in space-time domain. Although this proposed framework estimates both elastic modulus (storage modulus) and viscosity (loss modulus), we recommend utilizing it only for estimating viscosity, given that the phase-velocity based approach works quite well for the elastic modulus. In this work, synthetic data is employed to verify the effectiveness of the proposed approach. We will validate the model in the future with well controlled phantom experiment and ex-vivo porcine aorta data.

INTRODUCTION

Arterial stiffness is one of the important biomarkers for many cardiovascular diseases (Cheng *et al* 2002, Laurent *et al* 2000, Kingwell and Gatzka 2002, Sutton-Tyrrell *et al* 2005, Dolan *et al* 2006). To estimate the arterial stiffness non-invasively, the standard technique is to consider the Pulse Wave Velocity (CARO and CG 1962, Asmar *et al* 1995, Van Bortel *et al* 2012). However, as mentioned in (Couade *et al* 2010), the Pulse Wave Velocity approach suffers many limitations, including the global nature of the measurement. In contrast, the local arterial stiffness measurements can be performed using Acoustic Radiation Force (ARF) based imaging. In ARF setting, ultrasound wave is propagated through the tissue material and the tissue response is analyzed spatially and temporally for characterizing the tissue locally. There are several ARF methods (Doherty *et al* 2013), among which Shear Wave Elastography (SWE) has become a promising tool. In the case of organs with confined geometry such as artery, the shear wave becomes guided and dispersive (phase velocity changes with frequency). While the dispersive nature of wave makes the problem complicated, the different wave mode sensitivities help us to characterize the organs better (Gennisson *et al* 2010, Shcherbakova *et al* 2014).

In the SWE setting, there are many waveguide models such as an immersed plate model (Couade *et al* 2010, Bernal *et al* 2011, Nguyen *et al* 2011, Widman *et al* 2015, Jang *et al* 2015, Widman *et al* 2016, Maksuti *et al* 2016, Li *et al* 2017a), annuli waveguide (Li *et al* 2017c), hollow tube waveguide (Zhang *et al* 2005, Flamini *et al* 2015), fluid-filled tube (Flamini *et al* 2015, Lin *et al* 2015), immersed fluid-filled 3D finite element model (Dutta *et al* 2015), immersed fluid-filled SAFE model (Astaneh *et al* 2017) (Roy *et al* 2021). These models can be used to estimate modulus from wave propagation measurements. The immersed plate model in (Nguyen *et al* 2011) assessed the effect of both elasticity and viscoelasticity on the phase velocity dispersions and the authors concluded that the phase velocity dispersions are not influenced by the viscosity. However, wall viscosity is often considered an important biomarker in addition to stiffness. For the bulk organs (where the shear wave propagation is not effected by the organ boundaries), there are several approaches based on Rheological model and model free approaches as elucidated in (Nenadic *et al* 2018). Two such models are Attenuation Measuring Ultrasound Shearwave Elastography, AMUSE, (Nenadic *et al* 2017) and the Two-point Frequency Shift method (Kijanka and Urban 2020). While these approaches work well for the bulk organs, they are not effective in the case of arteries due to geometric confinement drastically altering both wave speed and attenuation.

In this chapter, we propose and evaluate three approaches to estimate viscoelastic shear moduli: Approach 1 considers the phase velocity dispersion in the wavenumber-frequency domain; Approach 2 utilizes at the decay rate of the wavenumber-time domain; Approach 3 tries to match the simulated and observed motion directly in space-time domain. Based on critical analyses of the three approaches, we suggest a hybrid method combining approaches 1 and 3 to estimate the viscoelastic shear-modulus, which includes both storage and loss moduli. We verify our proposed approaches by applying to noise-laden synthetic data, leading to the conclusion that the final hybrid approach is effective in estimating the arterial viscoelasticity.

PRELIMINARIES

Problem Statement

Given the arterial wall velocity measurements, our objective is to estimate the arterial stiffness and viscosity, essentially the viscoelastic shear modulus. For this, we model the carotid artery as an axisymmetric incompressible tube. The blood in the artery as well as the surrounding

tissue is considered as inviscid fluids given that the shear wave speeds in these domains are negligible compared to the arterial wall. The schematic of the problem is shown in Figure 6.1.

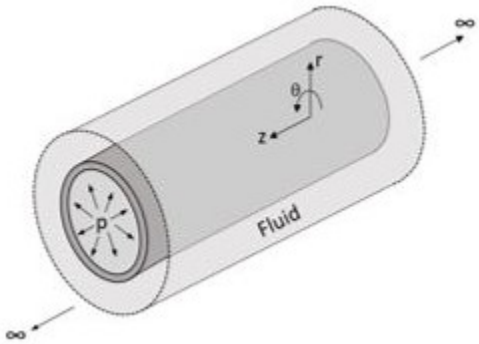

Figure 6.1 Geometry of the immersed axis-symmetric tube which mimics health human carotid artery.

The motion of the solid domain (Ω_S) can be represented by the Elastodynamic equation,

$$\mathbf{L}_\sigma^T \boldsymbol{\sigma} + \rho \frac{\partial^2 \mathbf{u}}{\partial t^2} = \mathbf{f}, \text{ in } \Omega_S \ . \tag{77}$$

The incompressible fluid domain (Ω_F) is governed by the Laplace equation:

$$\nabla^2 p = 0 \text{ in } \Omega_F . \tag{78}$$

The arterial wall motion is coupled to the interior and exterior fluid responses through interface conditions at the solid-fluid domain interface (Γ_{SF}) representing the continuity of velocity and traction:

$$\boldsymbol{\sigma} \cdot \mathbf{n}_s - p\mathbf{n}_F = 0, \text{ on } \Gamma_{SF} \ , \tag{79}$$

$$\frac{\partial^2 \mathbf{u}}{\partial t^2} \cdot \mathbf{n}_s - \frac{1}{\rho_F} \frac{\partial p}{\partial \mathbf{n}_F} = 0, \text{ on } \Gamma_{SF} \ . \tag{80}$$

For the solid medium, the primary variable is the displacement vector, $\boldsymbol{u} = \boldsymbol{u}(r, \theta, z, t)$ with 3 components namely $\boldsymbol{u} = \{u_r, u_\theta, u_z\}^T$. The stress tensor is $\boldsymbol{\sigma} = \lambda * \text{tr}(\boldsymbol{\epsilon}) I + 2G * \boldsymbol{\epsilon}$, where, $\boldsymbol{\epsilon}$ is the strain tensor (written in vector form) as $\boldsymbol{\epsilon} = \mathbf{L}_\epsilon \boldsymbol{u} = \{\epsilon_{rr}, \epsilon_{\theta\theta}, \epsilon_{zz}, \epsilon_{\theta z}, \epsilon_{rz}, \epsilon_{r\theta}\}^T$. The symbol, * is the convolution operator. In the limit of incompressibility, the Lamé operator λ approaches infinity,

while the shear modulus operator G is finite. For Voigt model, the shear modulus can be formally written in an operator form:

$$G(t) = G_0\left(1 + \beta\frac{\partial}{\partial t}\right). \tag{81}$$

For the spring-pot model, the shear modulus in operator form is,

$$G(t) = G_0\frac{\partial^\alpha}{\partial t^\alpha}. \tag{82}$$

The acoustic radiation force $\mathbf{f} = \mathbf{f}(r,\theta,z,t)$. The density of the solid medium is ρ. The 6×3 gradient operators, $\mathbf{L}_\sigma$ and $\mathbf{L}_\epsilon$ can be found in (Roy and Guddati 2021). For the fluid medium, the primary variable is the pressure $p = p(r,\theta,z,\omega)$. The Laplace operator in cylindrical coordinate system is given by $\nabla^2(\cdot) = r^{-1}\partial(r\partial(\cdot)/\partial r)/\partial r + r^{-2}\partial^2(\cdot)/\partial\theta^2 + \partial^2(\cdot)/\partial z^2$. In the interface conditions, $\mathbf{n}_s$ and $\mathbf{n}_F$ are the unit vectors for solid and fluid domain respectively (opposite vectors), and ρ_F is the fluid density.

SAFE and PMDL framework

Due to the invariant geometry and material properties along the axial and circumferential direction we utilize the Semi-Analytical Finite Element (SAFE) framework (Kausel 1986). Specifically the harmonic expansion is used in temporal, axial and circumferential directions, while we apply the finite element discretization along the radial direction. Therefore, for each wavemodes, the solutions take the form,

$$\begin{aligned}
\mathbf{u}_r(r,\theta,z,t) &= \mathbf{N}_S(r)u_r(m,k_{nm},\omega)e^{-i\omega t+ik_{nm}z}\cos(m\theta)\\
\mathbf{u}_\theta(r,\theta,z,t) &= \mathbf{N}_S(r)u_\theta(m,k_{nm},\omega)e^{-i\omega t+ik_{nm}z}\sin(m\theta)\\
\mathbf{u}_z(r,\theta,z,t) &= \mathbf{N}_S(r)u_z(m,k_{nm},\omega)e^{-i\omega t+ik_{nm}z}\cos(m\theta)
\end{aligned} \tag{83}$$

$$\mathbf{p}(r,\theta,z,t) = \mathbf{N}_F(r)\,p(m,k_{nm},\omega)e^{-i\omega t+ik_{nm}z}\cos(m\theta) \tag{84}$$

where $\mathbf{N}_S$ and $\mathbf{N}_F$ are the finite element shape functions along the radial direction for the solid and fluid domain respectively, m is the index of the azimuthal harmonic, n is the index of the normal modes due to the radial discretization, k_{nm} is the wavenumber along the axial direction,

$\omega = 2\pi f$ is the temporal frequency, and $i = \sqrt{-1}$. Substituting Equations (83) and (84) in governing equations (77) to (80), we get the discretized system:

$$\begin{bmatrix} k_{nm}^2 \mathbf{K}^{S2} + ik_{nm}\mathbf{K}^{S1} + \mathbf{K}^{S0} - {\omega_{nm}}^2 \mathbf{M}^S & -\kappa \mathbf{C}_{SF} \\ -{\omega_{nm}}^2 \mathbf{C}_{SF}^T & \kappa\left(k_{nm}^2 \mathbf{K}^{F2} + \mathbf{K}^{F0}\right) \end{bmatrix} \begin{Bmatrix} \mathbf{U}_{nm} \\ \mathbf{P}_{nm} \end{Bmatrix} = \begin{Bmatrix} \mathbf{F}_{nm} \\ \mathbf{0} \end{Bmatrix}, \quad (85)$$

where κ is the normalization factor to improve the conditioning of the system (Roy and Guddati 2021). The solid-domain contribution matrices, $\mathbf{K}^{S2}, \mathbf{K}^{S1}, \mathbf{K}^{S0}, \mathbf{M}^S$, the fluid-domain contribution matrices, $\mathbf{K}^{F2}, \mathbf{K}^{F0}$, and the fluid-structure interaction matrix, $\mathbf{C}_{SF}$ are defined in (Vaziri Astaneh and Guddati 2017b). These contribution matrices depend on the geometry (inner radius and thickness) and the material properties (densities and shear modulus). The $\mathbf{F}_{nm}$ is Fourier transform of the applied forcing $\mathbf{f}(r,\theta,z,t)$. Similarly, $\mathbf{U}_{nm}$ and $\mathbf{P}_{nm}$ are the Fourier transforms of primary variables $\mathbf{u}$ and $\mathbf{p}$ respectively.

The radial discretization, $\mathbf{N}_S$ and $\mathbf{N}_F$ includes linear finite elements for the solid and interior fluid domains, and Perfectly Matched Discrete Layers (PMDL) for the surrounding fluid (Guddati, 2020). To address the volumetric locking, we utilize selective reduced integration scheme. We analyze the above discretized system in two ways which are discussed in the following subsections.

Dispersion relation through k(ω) analysis

To get the dispersion relation, we perform modal analysis of the above dynamical system (equation (85)) for given angular frequency, ω. Specifically, we solve a the following quadratic Eigenvalue problem for the unknown k_{nm}:

$$\left[k_{nm}^2 \begin{bmatrix} \mathbf{K}^{S2} & \mathbf{0} \\ \mathbf{0} & \kappa\mathbf{K}^{F2} \end{bmatrix} + ik_{nm} \begin{bmatrix} \mathbf{K}^{S1} & \mathbf{0} \\ \mathbf{0} & \mathbf{0} \end{bmatrix} + \begin{bmatrix} \mathbf{K}^{S0} - \omega^2 \mathbf{M}^S & -\kappa \mathbf{C}_{SF} \\ -\omega^2 \mathbf{C}_{SF}^T & \kappa \mathbf{K}^{F0} \end{bmatrix} \right] \begin{Bmatrix} \boldsymbol{\phi}^S{}_{nm} \\ \boldsymbol{\phi}^F{}_{nm} \end{Bmatrix} = \begin{Bmatrix} \mathbf{0} \\ \mathbf{0} \end{Bmatrix} \quad (86)$$

Where $\boldsymbol{\phi}^S$ and $\boldsymbol{\phi}^F$ are the mode shapes corresponding to the displacements and pressure in solid and fluid domains, respectively. In (Vaziri Astaneh and Guddati 2017b), this quadratic Eigenvalue problem is transformed to a linear Eigenvalue problem by rearranging the degrees of freedom. Once we obtain the Eigenvalues, we look at the lowest real wavenumbers, k_{1m} and

compute the phase velocities as $c_{p,1m} = \omega / k_{1m}$. Then we plot the phase velocities as a function of cyclic frequency (Hz).

Full-wave simulation through ω(k) analysis

To get the full wave simulation from the equation (85), we perform a modal analysis where we consider an Eigenvalue problem for known wavenumber k and unknown frequency ω_{nm}:

$$\left[\begin{bmatrix} k^2\mathbf{K}^{S2} + ik\,\mathbf{K}^{S1} + \mathbf{K}^{S0} & -\kappa\mathbf{C}_{SF} \\ \mathbf{0} & \kappa\left(k^2\mathbf{K}^{F2} + \mathbf{K}^{F0}\right) \end{bmatrix} - \omega_{nm}^2 \begin{bmatrix} \mathbf{M}^S & \mathbf{0} \\ \mathbf{C}_{SF}^T & \mathbf{0} \end{bmatrix}\right] \begin{Bmatrix} \widetilde{\boldsymbol{\phi}_{nm}^S} \\ \widetilde{\boldsymbol{\phi}_{nm}^F} \end{Bmatrix} = \begin{Bmatrix} \mathbf{0} \\ \mathbf{0} \end{Bmatrix} \quad (87)$$

Where $\widetilde{\boldsymbol{\phi}^S}$ and $\widetilde{\boldsymbol{\phi}^F}$ are the mode shapes for the solid and fluid domain primary variables respectively. Next, we consider each of the above Eigen solutions as the uncoupled Single Degree of Freedom (SDOF) system and compute modal participation factors through utilizing the impulse response (Green's) function and the modal orthogonality. Lastly, we superimpose all the mode contributions with the participation factor,

$$\mathbf{U}_r(r = r_o, k, t) = \sum_{m=0}^{M}\sum_{n=1}^{N} v_{nm}(t)\left(\boldsymbol{\phi}_{nm}^S\right)^T \mathbf{F}_{nm}\left(\boldsymbol{\phi}_{nm}^S\right)_r (r = r_o) \quad ,(88)$$

where M is total numbers of circumferential modes considered. The total number of normal modes N depend on the number of degrees of freedom present in the discretized system. The v_{nm} is the modal participation factor. Here we are interested only in the top wall radial displacement $\mathbf{U}_r$ at the outer radius r_o in the solid domain. Lastly, we apply inverse Fourier transformation on the above radial displacement (equation (88)) in the wavenumber direction to get the full-wave response in $x-t$ domain. For the details of the above steps, the reader is referred to the Full-wave Simulation chapter.

With respect to the forcing function, we consider Gaussian functions with mean of zero and standard deviation of 2.e-4 and 0.25 in axial (x) and circumferential (θ) directions respectively as shown in Figure 6.2. In the radial direction, we consider uniform distribution through the thickness. In time, we apply square pulse as shown in Figure 6.2. This forcing function approximately represents the acoustic radiation force from a standard ultrasound transducer. With this applied force, tube wall thickness of 1 mm, inner radius of 3 mm, density of 1000 kg/m^3, and

Voigt viscoelastic model with elastic modulus of 250 kPa and damping ratio of 0.15, we get the following full wave data as shown in Figure 6.3. Note that in the actual SWE experiments, the tissue responses are recorded at the later time after applying the acoustic radiation push. Considering this fact, we shift the starting time by 0.78 ms.

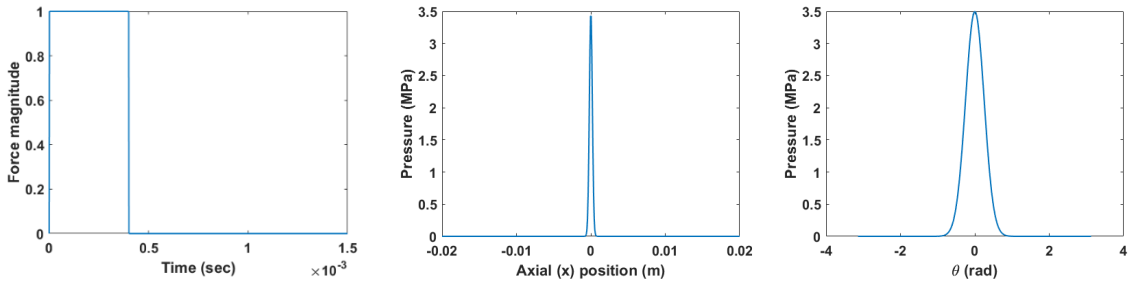

Figure 6.2 A representative applied excitation force in time (left), in axial (middle), and in circumferential (right) directions.

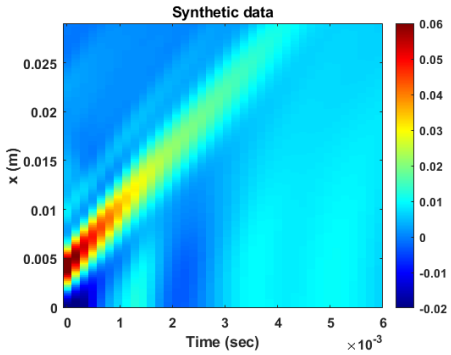

Figure 6.3 Generated full wave data with the considered excitation force, geometric and material properties.

INVERSION FRAMEWORK

Approach 1

The idea in this approach is to minimize the difference between the measured and simulated phase velocity dispersion. As mentioned in (Roy *et al* 2021), the multimodal framework in which we specifically match the measured phase velocity with the simulated phase velocity corresponding to the two circumferential modes. The objective function in the inversion analysis takes the form,

$$F_{objective} = \frac{\sum_{f_i=f_1}^{f_2}\left(c_2^s(f_i,q)-c^m(f_i)\right)^2 + \sum_{f_i=f_3}^{f_4}\left(c_1^s(f_i,q)-c^m(f_i)\right)^2}{\sum_{f_i=f_1}^{f_2}\left(c^m(f_i)\right)^2 + \sum_{f_i=f_3}^{f_4}\left(c^m(f_i)\right)^2}, \; q=[G_0,\xi] \quad (89)$$

where, c_1^s and c_2^s are the simulated phase velocities corresponding to the modes 1 and 2, respectively, and c^m is the phase velocity from the measured data. Based on the experimental observations in (Roy *et al* 2021), mode matching happens for, $f_1 = 400$ *Hz,* $f_2 = 600$ *Hz,* $f_3 = 800$ *Hz,* and $f_4 = 1200$ *Hz.* These specific frequency windows may change with the given data as they depend on the geometric and material properties of the tube.

To compute the measured dispersion, we first transform the spatiotemporal $(x-t)$ data to the Fourier space $(k-\omega)$ by applying 2D Fast Fourier transformation. We then pick the peak values in the Fourier space and plot the phase velocity, $c_p = \omega / k$ as a function of cyclic frequency (Hz). For the simulated dispersion, the steps are mentioned in section (Dispersion relation through k(ω) analysis).

With respect to inversion, the gradient-based optimization works well in this context. We employ the interior point algorithm with the BFGS Hessian approximation (MATLAB *fmincon* function), with box constraints at $\pm 30\%$ of the mean value. Given the small parameter space, gradients are computed using the finite difference technique. More details on this approach can be found in (Roy *et al* 2021).

Approach 2

The idea here is to look at the decay rate of the wavenumber-time $(k-t)$ domain response; this is based on the hypothesis that response for a given k at the top of the artery can be approximated as a single-degree-of-freedom system. The steps are thus, (1) transforming the entire $x-t$ (including both left and right propagating parts) data to the $k-t$ domain data through Fast Fourier Transform along the axial direction x, (2) for each of the wavenumbers ranging from 500 to 800 (1/m), compare it with a damped Single Degree of Freedom (SDOF) system to estimate the decay rate. These steps are highlighted in Figure 6.4. The final result is plotted as the estimated decay rate as a function of wavenumber (see e.g. Figure 6.5).

With respect to the second step of estimating the decay rate, we consider the gradient-based optimization to minimize the difference between the considered $k-t$ domain data and the damped

SDOF responses. For this minimization, MATLAB's unconstrained optimization function, *fminunc,* is employed.

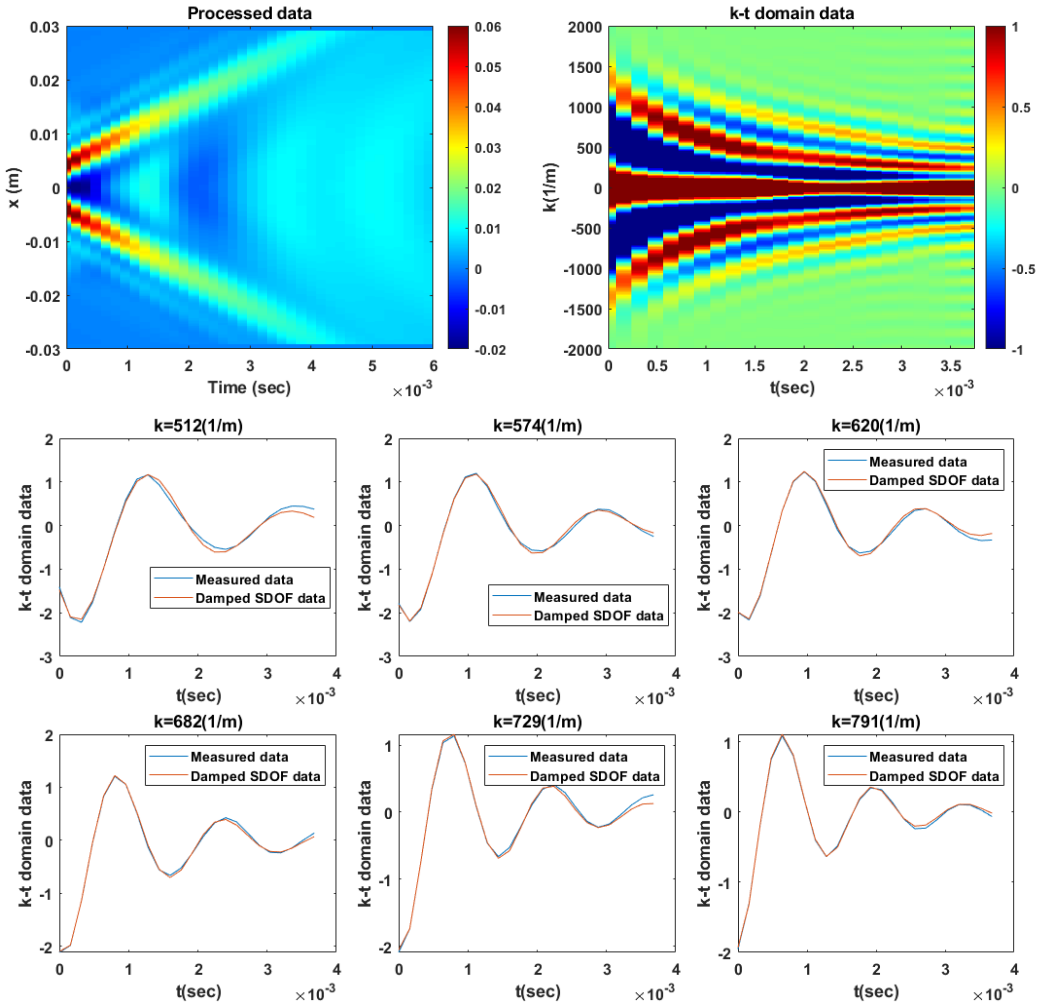

Figure 6.4 The full measured data (top-left), the corresponding k-t domain data (top-right), and the finally matching the k-t domain data with the damped SDOF system at specific k ranges (bottom).

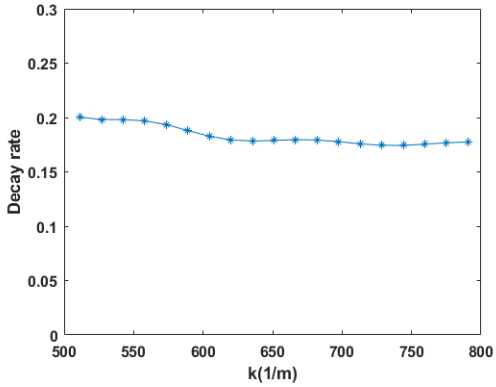

Figure 6.5 The estimated decay rate is expressed as a function of wavenumber.

Approach 3

In this approach, we directly utilize the full-wave simulation framework to estimate the viscoelasticity, my maximizing the correlation between measured and simulated wall velocity in $x-t$ domain. In addition, to focus more on higher frequency content and to correct for any bias-type of noise, we subtract both measured and simulated (spatiotemporal) data by its mean. Thus, the objective function is given by,

$$\rho(v^m, v^s) = \frac{1}{N-1}\sum_{i=1}^{N}\left(\frac{v_i^m - v_\mu^m}{v_\sigma^m}\right)\left(\frac{v_i^s - v_\mu^s}{v_\sigma^s}\right) \qquad (90)$$

Where N is the total number of data points in the $x-t$ domain. The v^m and v^s are the measured and simulated motions. The mean and standard deviation of the measured velocity are,

$$v_\mu^m = \frac{1}{N}\sum_{i=1}^{N} v_i^m, \quad v_\sigma^m = \sqrt{\frac{\sum_{i=1}^{N}\left(v_i^m - v_\mu^m\right)^2}{N}} \qquad (91)$$

Similarly, for the simulated velocity, the mean and standard deviation are,

$$v_\mu^s = \frac{\sum_{i=1}^{N} v_i^s}{N}, \; v_\sigma^s = \sqrt{\frac{\sum_{i=1}^{N}\left(v_i^s - v_\mu^s\right)^2}{N}} \qquad (92)$$

SENSITIVITY STUDY

In this section, we examine the sensitivity of the two parameters namely the elastic modulus G_0 and the damping ratio ξ for all three approaches mentioned in the previous section. Note that we perform sensitivity analysis through perturbing one parameter at a time. Figure 6.6 shows the sensitivity of the parameters for the Approach 1. As clearly observed in Figure 6.6, the only influential parameter is the elastic modulus, G_0. Therefore, this approach is well suited for the estimation of the elastic modulus (see (Roy *et al* 2021) for details), but not the attenuation.

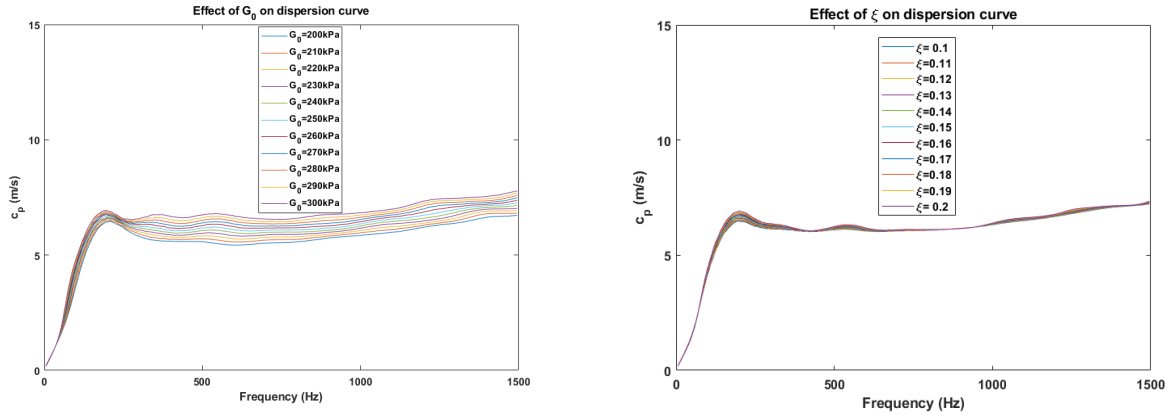

Figure 6.6 Effect of the elastic modulus keeping the damping ratio at 0.15 (left) and effect of the damping ratio keeping the elastic modulus at 250 kPa (right) on the phase velocity dispersion (approach-1).

Sensitivity study results for Approach 2 are presented in Figure 6.7. We find here that the influential parameter is the damping ratio ξ but not the modulus. Therefore, this approach can be considered to estimate viscoelasticity, if there is an alternative way to obtain the modulus.

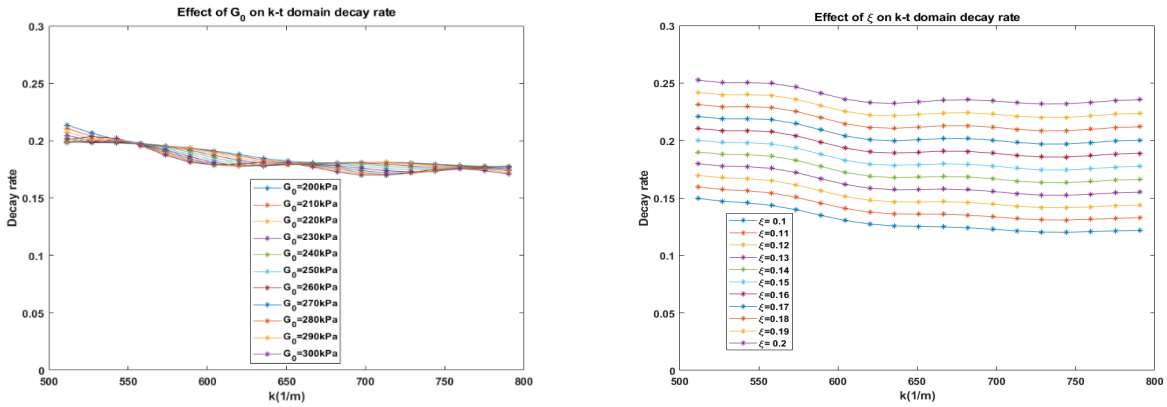

Figure 6.7 Effect of elastic modulus maintaining the damping ratio at 0.15 (left) and effect of damping ratio maintaining the elastic modulus at 250 kPa (right), on the k-t domain decay rate (Approach 2).

For Approach 3, both parameters are sensitive as shown in Figure 6.8 and Figure 6.9, which show, respectively, the effect of modulus and damping ratio. In Figure 6.8, the slope of the pulse in space-time domain changes, while in Figure 6.9, the decay rate along the direction of propagation is altered.

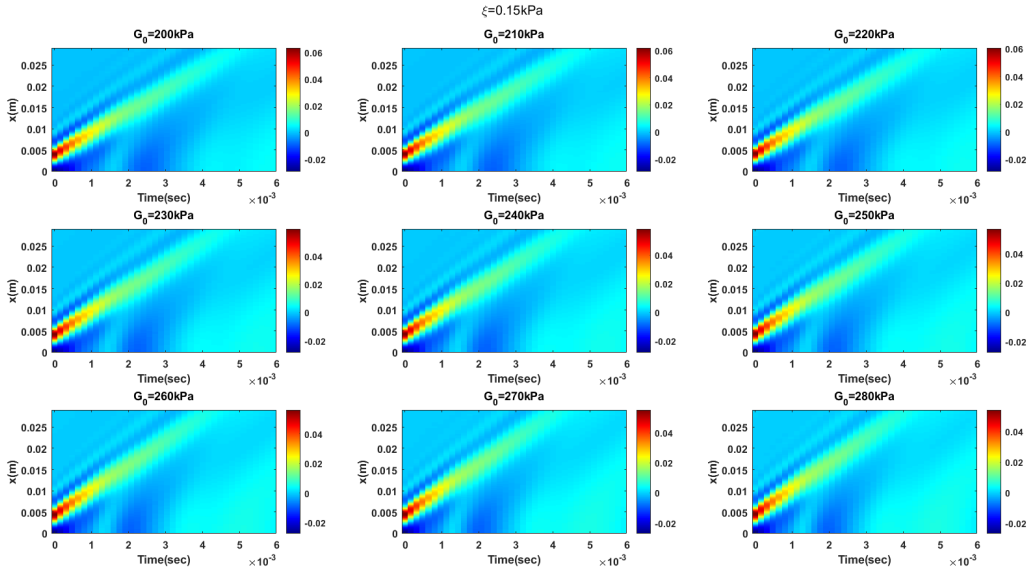

Figure 6.8 Effect of modulus keeping the damping ratio at 0.15.

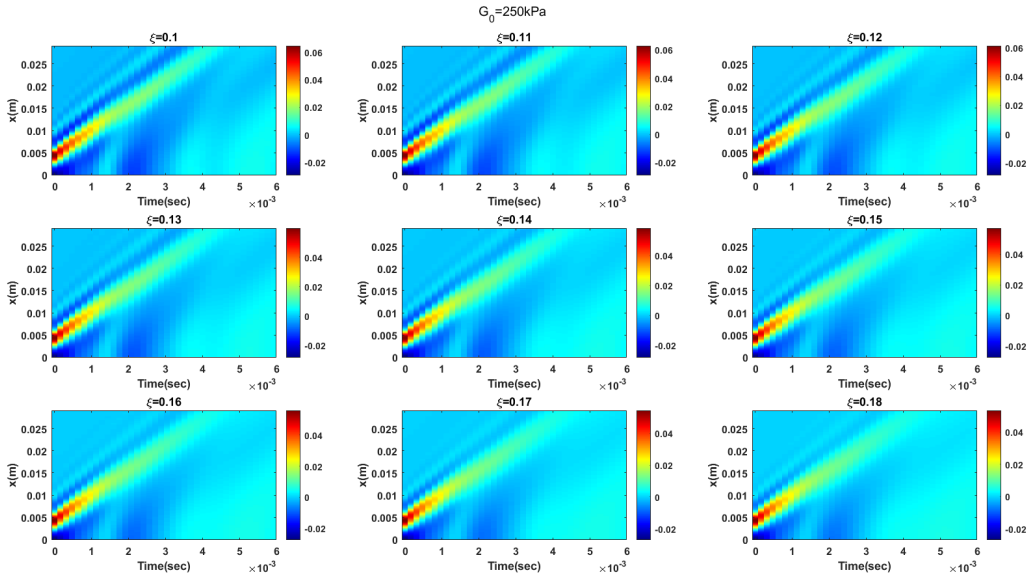

Figure 6.9 Effect of damping ratio keeping the modulus parameter of 250 kPa.

PROPOSED APPROACH

Given the modulus parameter is the only influential parameter in Approach 1, we recommend it for the modulus inversion. In fact we have observed satisfactory results for the modulus estimation with the Approach 1 not only with synthetic data, but also with real experimental data (Roy *et al* 2021). As for Approach 2, only the damping ratio is the influential parameter; thus, this approach can be considered sequentially after the approach-1 to invert damping ratio. However, if we note from Figure 6.7 that the inverted decay rate (0.18-0.20) is higher than the actual damping ratio of 0.15. The reason behind this inaccuracy is the fact that we have assumed the $k-t$ domain response at each wavenumber as the SDOF system response. However, we know this response is a superposition of several modes, and single-degree-of-freedom approximation translates to the incorrect estimation of viscoelasticity.

In Approach 3, both parameters are influential and thus this approach can be used by itself to invert for both elastic modulus and damping ratio. This is our proposed approach. In the future, given the confidence gained through validation of approach 1 (Roy *et al* 2021), a two-step process can be examined: (1) evaluate the elastic modulus from the phase velocity dispersion (approach-1), then (2) estimate complete viscoelastic parameters from the correlation between the measured velocity and the full wave data in the $x-t$ domain (Approach 3). In this work, however, we will limit to verification of Approach 3 using synthetic data, for two different models of viscoelasticity.

Verification of Approach 3 Using Synthetic Data

To examine the effectiveness of Approach 3, we first generate synthetic data from the full-wave simulation (see section Full-wave simulation through ω(k) analysis), polluted with bias and both additive noise and multiplicative noise:

$$v_{synthetic} = v_{full-wave}(1+\epsilon_{multiplicative}) + \epsilon_{additive} + b \ . \quad (93)$$

We consider two different levels of noise. For the medium noise level, the bias value, b is 0.01 and the noise distributions are taken as Gaussian: $\epsilon_{multiplicative} \sim \mathrm{N}(\mu = 0, \sigma^2 = 0.07^2)$ and $\epsilon_{additive} \sim \mathrm{N}(\mu = 0, \sigma^2 = 0.001^2)$. For higher level of noise, the bias value b is chosen as 0.02, and the noise distributions are $\epsilon_{multiplicative} \sim \mathrm{N}(\mu = 0, \sigma^2 = 0.10^2)$ and $\epsilon_{additive} \sim \mathrm{N}(\mu = 0, \sigma^2 = 0.003^2)$. Representative synthetic data for these two cases are shown in Figure 6.10, using a modulus of 250 kPa and damping ratio is 0.15.

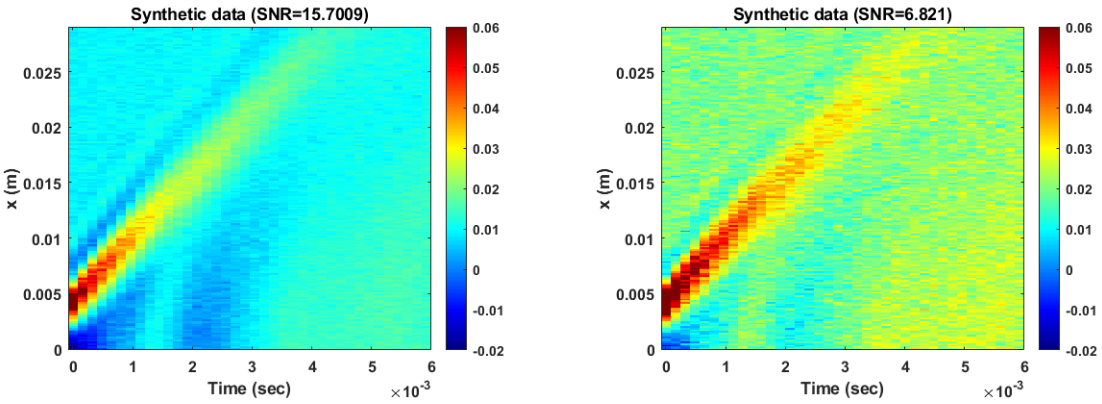

Figure 6.10 Synthetic data with noise added - medium noise level (left) and higher noise level (right)

We apply Approach 3 to the two polluted synthetic data sets from a Voigt viscoelastic model. Specifically, we examine the correlation coefficient in equation (90) between synthetic, polluted data and the predicted data from full-wave simulations for several elastic modulus and the damping ratio values. Figure 6.11 shows the variation of the correlation coefficient over the parameter space. As observed, for both polluted data sets, we get the maximum correlation which is at the expected location. In addition, we observe from the figure that the objective function is well behaving and convex near the optimal point. Encouraged by this, we utilize gradient

optimization (interior point algorithm with BFGS Hessian), for various sets of synthetic data with different combination of parameter values. In all these experiments, as shown in

Table 1, we converge to a point near the expected values, indicating the effectiveness of the proposed approach.

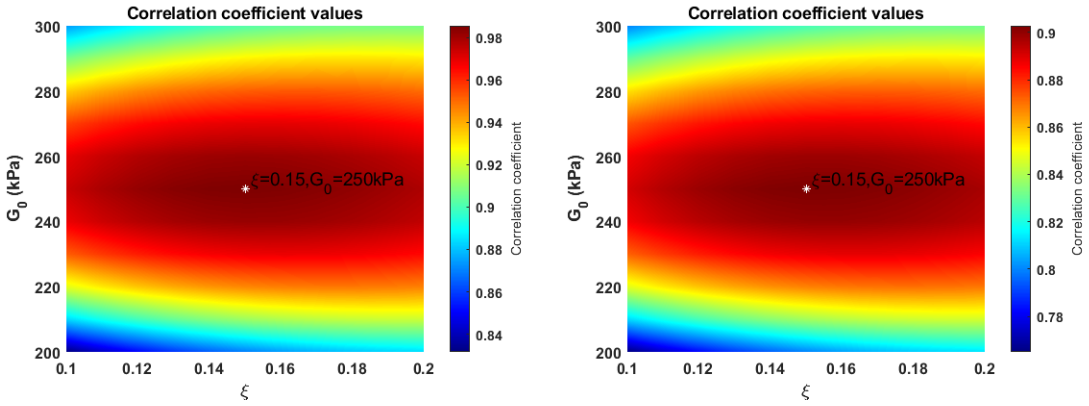

Figure 6.11 Correlation coefficients variation for Voigt viscoelastic model for synthetic data with medium noise (left) and high noise (right).

Table 1 Gradient optimization results for Voigt model.

Cases	Expected parameters		Optimal Results				Correlation coefficients	
			Medium noise level		Higher noise level			
	G_0(kPa)	ξ	G_0(kPa)	ξ	G_0(kPa)	ξ	Medium noise	Higher noise
1	250	0.15	250.34	0.15	250.75	0.152	0.9852	0.9060
2	220	0.12	219.93	0.118	220.16	0.116	0.9891	0.9249
3	220	0.17	220.1	0.17	219.74	0.169	0.9859	0.9026
4	270	0.17	270.18	0.169	269.72	0.17	0.9828	0.8824
5	270	0.12	270.32	0.119	269.71	0.115	0.9874	0.9194

We repeat the above process for the spring-pot viscoelastic model. An example objective function (correlation coefficient) variation is shown in Figure 6.12, which again indicates a well-behaving and locally convex objective function. Although the gradient-based optimization should work for this well-behaving convex objective function, we first created a database of the simulated responses with 61 fractional order, α from 0.12 to 0.18 and 21 modulus parameter, A from 290 to 310 and then performed the inversion analysis in a brute force manner at the considered parameter points. The corresponding results are shown in Table 2, which indicated the effectiveness of the proposed approach for more complicated spring-pot viscoelastic model.

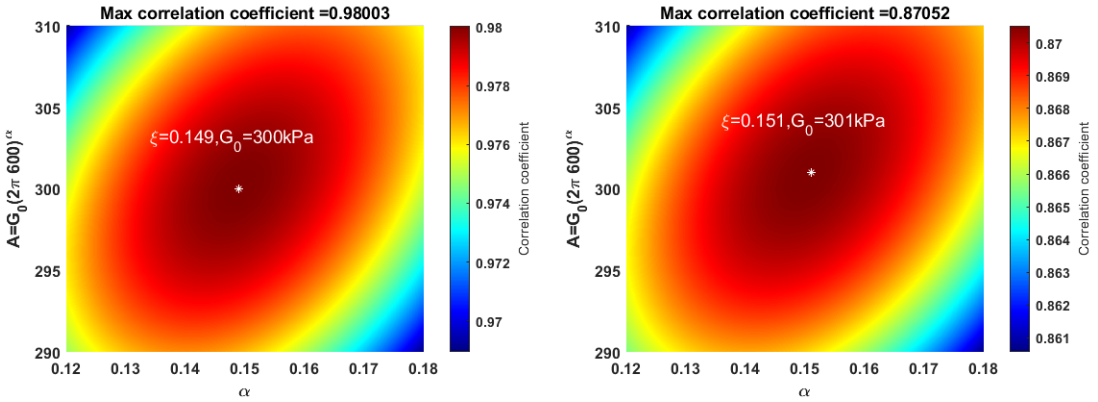

Figure 6.12 Correlation coefficients variation for spring-pot viscoelastic model for synthetic data with medium noise (left) and high noise (right).

Table 2 Brute force optimization results for spring-pot model. Here the parameters are $A=G_0(2\pi x600)^{\alpha}$ and α.

Case No.	Expected parameters		Optimal Results				Correlation coefficients	
			Medium noise level		Higher noise level			
	A	α	A	α	A	α	Medium noise	Higher noise
1	300	0.150	300	0.149	301	0.152	0.9800	0.8705
2	294	0.134	294	0.133	294	0.132	0.9817	0.8786
3	294	0.165	294	0.165	293	0.161	0.9787	0.8579
4	305	0.165	305	0.165	305	0.167	0.9783	0.8571
5	305	0.134	305	0.134	306	0.132	0.9817	0.8749

SUMMARY

In this chapter, we examined three approaches to back-calculate the viscoelastic parameters and concluded that a full-waveform correlation based inversion approach works well to estimate the arterial wall viscoelasticity from wall velocity measurements. The examined approaches perform the analysis in three different domains: Approach 1 attempts to match the dispersion curves effectively in wavenumber-frequency domain; Approach 2 matches the decay rate in

wavenumber-time domain; Approach 3 maximizes the correlation of measured and simulated space-time responses. Through sensitivity analyses, we observed that Approach 1 would work well for estimating the elastic modulus but is not sensitive for the damping parameter. On the other hand, Approach 2 is sensitive to the viscous parameter, but not to the elastic modulus. While sequential application of these two approaches could lead to viscoelastic inversion, Approach 2 overestimates the damping ratio, leading us to Approach 3, where both elastic modulus and viscosity parameter are shown to be influential parameters. In fact, the effectiveness of Approach 3 is illustrated with the help of noise laden synthetic data. In the future, we intend to explore improvements of computational cost by combining these approaches, e.g. using estimated modulus from Approach 1, and estimated viscous parameter from Approach 2 as starting points for estimating both the parameters using Approach 3. Experimental validation of the proposed approach is also a subject of future research.

CHAPTER 7: CONCLUSION

SUMMARY

Motivated with the goal of estimating the arterial stiffness in this dissertation, we approach towards our objective sequentially – (1) estimating wall thickness and elastic modulus in the frequency-wavenumber domain through the phase velocity dispersions, then (2) estimating the viscoelastic modulus in the space-time domain through the full wave simulation. To achieve these two, we first develop the mathematical model that captures the governing physics. Next, we develop an inversion algorithm to estimate the modulus (and thickness) and validate using phantom experiments. Noting that inversion for both modulus and thickness is not as reliable as inverting for modulus alone, it would be beneficial to inform the inversion with prior thickness information from B-mode images. To eventually facilitate this, and quantify the uncertainty in the inverted parameters, we develop a mixed-mode Frequentist inversion of modulus (and thickness). Towards the second goal of viscoelastic inversion, we take a two-step approach of (a) developing a fast simulation approach to compute full wave response of the arterial wall, and (b) a spatiotemporal correlation-based inversion approach that can perform inversion of both storage and loss moduli; the approach is verified with the help of noise-laden synthetic data.

RECOMMENDATIONS FOR FUTURE WORK

While the work presented in this dissertation takes us closer to more reliable arterial stiffness estimation, several additional steps remain to be done:

- Development of a Bayesian inversion framework that can effectively take the prior information on thickness from B mode images.
- Expansion of the above approach to full viscoelastic inversion by combining with the current contribution on viscoelastic inversion. The objective would be to utilize the wall data and B-mode images to obtain probabilistic representation of thickness and various viscoelastic parameters.
- Validation of viscoelastic inversion using well-controlled phantom experiments and potentially *ex vivo* porcine aortas.
- *In vivo* application, including correlation of the estimated parameters with age, gender, and disease, which could help delineate the most influential biomarkers.

REFERENCES

Amador C, Urban M W, Chen S and Greenleaf J F 2011 Shearwave dispersion ultrasound vibrometry (SDUV) on swine kidney *IEEE Trans. Ultrason. Ferroelectr. Freq. Control* **58** 2608–19

Anon NOMAD - A blackbox optimization software Online: https://www.gerad.ca/nomad/

Asmar R, Benetos A, Topouchian J, Laurent P, Pannier B, Brisac A M, Target R and Levy B I 1995 Assessment of arterial distensibility by automatic pulse wave velocity measurement: Validation and clinical application studies *Hypertension* **26** 485–90

Astaneh A V, Urban M W, Aquino W, Greenleaf J F and Guddati M N 2017 Arterial waveguide model for shear wave elastography: implementation and in vitro validation *Phys. Med. Biol.* **62** 5473–94

Barbosa J M de O, Park J and Kausel E 2012 Perfectly matched layers in the thin layer method *Comput. Methods Appl. Mech. Eng.* **217**–**220** 262–74

Bercoff J, Tanter M and Fink M 2004 Supersonic shear imaging: A new technique for soft tissue elasticity mapping *IEEE Trans. Ultrason. Ferroelectr. Freq. Control* **51** 396–409

Berliner M J and Solecki R 1996 Wave propagation in fluid-loaded, transversely isotropic cylinders. Part I. Analytical formulation *J. Acoust. Soc. Am.* **99** 1841–7

Bernal M, Nenadic I, Urban M W and Greenleaf J F 2011 Material property estimation for tubes and arteries using ultrasound radiation force and analysis of propagating modes *J. Acoust. Soc. Am.* **129** 1344–54

Van Bortel L M, Laurent S, Boutouyrie P, Chowienczyk P, Cruickshank J K, De Backer T, Filipovsky J, Huybrechts S, Mattace-Raso F U S, Protogerou A D, Schillaci G, Segers P, Vermeersch S and Weber T 2012 Expert consensus document on the measurement of aortic stiffness in daily practice using carotid-femoral pulse wave velocity *Journal of Hypertension* vol 30 pp 445–8

Boutouyrie P, Laurent S, Benetos A, Girerd X J, Hoekst A P G and Safar M E 1992 Opposing effects of ageing on distal and proximal large arteries in hypertensives *J. Hypertens.* **10** S87–92

Brum J, Bernal M, Gennisson J L and Tanter M 2014 In vivo evaluation of the elastic anisotropy of the human Achilles tendon using shear wave dispersion analysis *Phys. Med. Biol.* **59** 505–23

Bussy C, Boutouyrie P, Lacolley P, Challande P and Laurent S 2000 Intrinsic stiffness of the carotid arterial wall material in essential hypertensives *Hypertension* **35** 1049–54

CARO and CG 1962 Observations on pulse wave velocity and pulsatile blood pressure in the human pulmonary circulation *Clin Sci* **23** 317–29

Chen S, Urban M W, Pislaru C, Kinnick R, Zheng Y, Yao A and Greenleaf J F 2009 Shearwave dispersion ultrasound vibrometry (SDUV) for measuring tissue elasticity and viscosity *IEEE Trans. Ultrason. Ferroelectr. Freq. Control* **56** 55–62

Cheng K S, Baker C R, Hamilton G, Hoeks A P G and Seifalian A M 2002 Arterial elastic properties and cardiovascular risk/event *Eur. J. Vasc. Endovasc. Surg.* **24** 383–97

Chew W C and Weedon W H 1994 A 3D perfectly matched medium from modified maxwell's equations with stretched coordinates *Microw. Opt. Technol. Lett.* **7** 599–604

Chirinos J A, Segers P, Hughes T and Townsend R 2019 Large-Artery Stiffness in Health and Disease: JACC State-of-the-Art Review *J. Am. Coll. Cardiol.* **74** 1237–63

COCKCROFT J, WILKINSON I, EVANS M, MCEWAN P, PETERS J, DAVIES S, SCANLON M and CURRIE C 2005 Pulse Pressure Predicts Cardiovascular Risk in Patients With Type 2 Diabetes Mellitus *Am. J. Hypertens.* **18** 1463–7

Couade M, Pernot M, Messas E, Bel A, Ba M, Hagege A, Fink M and Tanter M 2011 In Vivo quantitative mapping of myocardial stiffening and transmural anisotropy during the cardiac cycle *IEEE Trans. Med. Imaging* **30** 295–305

Couade M, Pernot M, Prada C, Messas E, Emmerich J, Bruneval P, Criton A, Fink M and Tanter M 2010 Quantitative Assessment of Arterial Wall Biomechanical Properties Using Shear Wave Imaging *Ultrasound Med. Biol.* **36** 1662–76

Currie J and Wilson D I 2012 *Opti: Lowering the Barrier Between Open Source Optimizers and the Industrial MATLAB User* ed N Sahinidis and J Pinto (Savannah, Georgia, USA: Foundations of Computer-Aided Process Operations)

Datta S K, Bratton R L, Chakraborty T and Shah A H 1988 Wave propagation in laminated composite plates *J. Acoust. Soc. Am.* **83** 2020–6

Demidenko E 2013 *Mixed Models: Theory and Applications with R* (Germany: Wiley)

Doherty J R, Trahey G E, Nightingale K R and Palmeri M L 2013 Acoustic radiation force elasticity imaging in diagnostic ultrasound *IEEE Trans. Ultrason. Ferroelectr. Freq. Control* **60** 685–701

Dolan E, Thijs L, Li Y, Atkins N, McCormack P, McClory S, O'Brien E, Staessen J A and Stanton A V 2006 Ambulatory arterial stiffness index as a predictor of cardiovascular mortality in the Dublin Outcome Study. *Hypertens. (Dallas, Tex. 1979)* **47** 365–70

Dutta P, Urban M W, Le Maître O P, Greenleaf J F and Aquino W 2015 Simultaneous identification of elastic properties, thickness, and diameter of arteries excited with ultrasound radiation force *Phys. Med. Biol.* **60** 5279–96

Flamini V, Creane A P, Kerskens C M and Lally C 2015 Imaging and finite element analysis: A methodology for non-invasive characterization of aortic tissue *Med. Eng. Phys.* **37** 48–54

Foti S, Lai C, Rix G and Strobbia C 2014 *Surface wave methods for near-surface site characterization* (CRC Press, London)

Gavrić L 1995 Computation of propagative waves in free rail using a finite element technique *J. Sound Vib.* **185** 531–43

Gazis D C 1959a Three-Dimensional Investigation of the Propagation of Waves in Hollow Circular Cylinders. I. Analytical Foundation *J. Acoust. Soc. Am.* **31** 568–73

Gazis D C 1959b Three-dimensional investigation of the propagation of waves in hollow circular cylinders. ii. numerical results *J. Acoust. Soc. Am.* **31** 573–8

Gennisson J L, Deffieux T, Macé E, Montaldo G, Fink M and Tanter M 2010 Viscoelastic and anisotropic mechanical properties of in vivo muscle tissue assessed by supersonic shear imaging *Ultrasound Med. Biol.* **36** 789–801

Ghibril R N 1992 *On the partial discretization of coupled plane stratified systems.* (Massachusetts Institute of Technology)

Glasser S P, Arnett D K, McVeigh G E, Finkelstein S M, Bank A J, Morgan D J and Cohn J N 1997 Vascular compliance and cardiovascular disease: A risk factor or a marker? *Am. J. Hypertens.* **10** 1175–89

Gry L 1996 Dynamic modelling of railway track based on wave propagation *J. Sound Vib.* **195** 477–505

Guddati M 2020 Perfectly matched discrete layers for modeling unbounded domains *J. Acoust. Soc. Am.* **148** 2452

Guddati M, Lim K and Zahid M A 2008 Perfectly matched discrete layers for unbounded domain modeling *Computational Methods for Acoustics Problems* ed F Magoulès (Stirlingshire, UK: Saxe-Coburg Publications) pp 69–98

Guddati M N, Druskin V and Vaziri Astaneh A 2016 Exponential convergence through linear finite element discretization of stratified subdomains *J. Comput. Phys.* **322** 429–47

Guddati M N and Lim K-W 2006 Continued fraction absorbing boundary conditions for convex polygonal domains *Int. J. Numer. Methods Eng.* **66** 949–77

Guerin A P, Blacher J, Pannier B, Marchais S J, Safar M E and London G M 2001 Impact of aortic stiffness attenuation on survival of patients in end-stage renal failure *Circulation* **103** 987–92

Hadj Henni A, Schmitt C, Tremblay M É, Hamdine M, Heuzey M C, Carreau P and Cloutier G 2011 Hyper-frequency viscoelastic spectroscopy of biomaterials *J. Mech. Behav. Biomed. Mater.* **4** 1115–22

Han X, Liu G R, Xi Z C and Lam K Y 2001 Transient waves in a functionally graded cylinder *Int. J. Solids Struct.* **38** 3021–37

Haskell N A 1953 *The Dispersion of Surface Waves in Multilayered Anisotropic Media* vol 43

Hayashi T, Kawashima K, Sun Z and Rose J L 2003 Analysis of flexural mode focusing by a semianalytical finite element method *J. Acoust. Soc. Am.* **113** 1241–8

Helfenstein-Didier C, Andrade R J, Brum J, Hug F, Tanter M, Nordez A and Gennisson J L 2016 In vivo quantification of the shear modulus of the human Achilles tendon during passive loading using shear wave dispersion analysis *Phys. Med. Biol.* **61** 2485–96

Hirai T, Sasayama S, Kawasaki T and Yagi S 1989 Stiffness of systemic arteries in patients with myocardial infarction. A noninvasive method to predict severity of coronary atherosclerosis. *Circulation* **80** 78–86

Hughes T J R 2012 *The Finite Element Method: Linear Static and Dynamic Finite Element Analysis* (Dover Publications)

Jang J K, Kondo K, Namita T, Yamakawa M and Shiina T 2015 Comparison of techniques for estimating shear-wave velocity in arterial wall using shear-wave elastography - FEM and phantom study *2015 IEEE International Ultrasonics Symposium, IUS 2015* (Institute of Electrical and Electronics Engineers Inc.)

Kanai H 2005 Propagation of spontaneously actuated pulsive vibration in human heart wall and in vivo viscoelasticity estimation *IEEE Trans. Ultrason. Ferroelectr. Freq. Control* **52** 1931–42

Karageorgos G M, Apostolakis I Z, Nauleau P, Gatti V, Weber R, Connolly E S, Miller E C and

Konofagou E E 2020 Arterial wall mechanical inhomogeneity detection and atherosclerotic plaque characterization using high frame rate pulse wave imaging in carotid artery disease patients in vivo *Phys. Med. Biol.* **65**

Kasai C, Namekawa K, Koyano A and Omoto R 1985 Real-Time Two-Dimensional Blood Flow Imaging Using an Autocorrelation Technique *IEEE Trans. SONICS Ultrason.* **32**

Kausel E 2018 Can a discrete dynamic model ever perfectly simulate a continuum? *Soil Dyn. Earthq. Eng.* **112** 53–7

Kausel E 1986 Wave propagation in anisotropic layered media *Int. J. Numer. Methods Eng.* **23** 1567–78

Kausel E and de Oliveira Barbosa J M 2012 PMLs: A direct approach *Int. J. Numer. Methods Eng.* **90** 343–52

Kausel E and Peek R 1982 DYNAMIC LOADS IN THE INTERIOR OF A LAYERED STRATUM: AN EXPLICIT SOLUTION *Bull. Seismol. Soc. Am.* **72** 1459–1481

Kennedy J and Eberhart R 1995 Particle swarm optimization *Proceedings of ICNN'95 - International Conference on Neural Networks* vol 4 (IEEE) pp 1942–8

Kijanka P, Qiang B, Song P, Amador Carrascal C, Chen S and Urban M W 2018 Robust Phase Velocity Dispersion Estimation of Viscoelastic Materials Used for Medical Applications Based on the Multiple Signal Classification Method *IEEE Trans. Ultrason. Ferroelectr. Freq. Control* **65** 423–39

Kijanka P and Urban M W 2021a Dispersion curve calculation in viscoelastic tissue-mimicking materials using non-parametric, parametric, and high-resolution methods *Ultrasonics* **109** 106257

Kijanka P and Urban M W 2021b Phase Velocity Estimation with Expanded Bandwidth in Viscoelastic Phantoms and Tissues *IEEE Trans. Med. Imaging* **40** 1352–62

Kijanka P and Urban M W 2020 Two-Point Frequency Shift Method for Shear Wave Attenuation Measurement *IEEE Trans. Ultrason. Ferroelectr. Freq. Control* **67** 483–96

Kingwell B A and Gatzka C D 2002 Arterial stiffness and prediction of cardiovascular risk *J. Hypertens.* **20**

Knopoff L. 1964 *A MATRIX METHOD FOR ELASTIC WAVE PROBLEMS* vol 54

Kokossalakis G 2006 *Acoustic data communication system for in-pipe wireless sensor networks* (Massachusetts Institute of Technology)

Korteweg D J 1878 Ueber die Fortpflanzungsgeschwindigkeit des Schalles in elastischen Röhren *Ann. der Phys. und Chemie* **241** 525–42

Kullo I J and Malik A R 2007 Arterial Ultrasonography and Tonometry as Adjuncts to Cardiovascular Risk Stratification *J. Am. Coll. Cardiol.* **49** 1413–26

Kumar J and Naskar T 2017 A fast and accurate method to compute dispersion spectra for layered media using a modified Kausel-Roësset stiffness matrix approach *Soil Dyn. Earthq. Eng.* **92** 176–82

Kundu T 2003 *Ultrasonic nondestructive evaluation: engineering and biological material characterization* ed T Kundu (CRC Press, UK)

Lagarias J C, Reeds J A, Wright M H, Wright P E and Optim S J 1998 CONVERGENCE PROPERTIES OF THE NELDER-MEAD SIMPLEX METHOD IN LOW DIMENSIONS *SIAM J. Optim.* **9** 112–47

Laurent S, Boutouyrie P, Asmar R, Gautier I, Laloux B, Guize L, Ducimetiere P and Benetos A 2000 Aortic stiffness is an independent predictor of all-cause mortality in hypertensive patients *J. Hypertens.* **18**

Laurent S, Cockcroft J, Van Bortel L, Boutouyrie P, Giannattasio C, Hayoz D, Pannier B, Vlachopoulos C, Wilkinson I and Struijker-Boudier H 2006 Expert consensus document on arterial stiffness: Methodological issues and clinical applications *Eur. Heart J.* **27** 2588–605

Li G Y, He Q, Jia L, He P, Luo J and Cao Y 2017a An Inverse Method to Determine Arterial Stiffness with Guided Axial Waves *Ultrasound Med. Biol.* **43** 505–16

Li G Y, He Q, Mangan R, Xu G, Mo C, Luo J, Destrade M and Cao Y 2017b Guided waves in pre-stressed hyperelastic plates and tubes: Application to the ultrasound elastography of thin-walled soft materials *J. Mech. Phys. Solids* **102** 67–79

Li G Y, He Q, Xu G, Jia L, Luo J and Cao Y 2017c An ultrasound elastography method to determine the local stiffness of arteries with guided circumferential waves *J. Biomech.* **51** 97–104

Lin S M, Wang W R, Lee S Y, Chen C W, Hsiao Y C and Teng M J 2015 Wave modes of a pre-stressed thick tube conveying blood on the viscoelastic foundation *Appl. Math. Model.* **39** 466–82

Lowe M J 1995 Matrix Techniques for Modeling Ultrasonic Waves in Multilayered Media *IEEE Trans. Ultrason. Ferroelectr. Freq. Control* **42** 525–42

Luo J, Fujikura K, Tyrie L S, Tilson M D and Konofagou E E 2009 Pulse wave imaging of normal and aneurysmal abdominal aortas in vivo *IEEE Trans. Med. Imaging* **28** 477–86

Luo J, Li R X and Konofagou E E 2012 Pulse wave imaging of the human carotid artery: An in vivo feasibility study *IEEE Trans. Ultrason. Ferroelectr. Freq. Control* **59** 174–81

Maksuti E, Bini F, Fiorentini S, Blasi G, Urban M W, Marinozzi F and Larsson M 2017 Influence of wall thickness and diameter on arterial shear wave elastography: a phantom and finite element study *Phys. Med. Biol.* **62** 2694–718

Maksuti E, Widman E, Larsson D, Urban M W, Larsson M and Bjällmark A 2016 Arterial Stiffness Estimation by Shear Wave Elastography: Validation in Phantoms with Mechanical Testing *Ultrasound Med. Biol.* **42** 308–21

Marais L, Pernot M, Khettab H, Tanter M, Messas E, Zidi M, Laurent S and Boutouyrie P 2019 Arterial Stiffness Assessment by Shear Wave Elastography and Ultrafast Pulse Wave Imaging: Comparison with Reference Techniques in Normotensives and Hypertensives *Ultrasound Med. Biol.* **45** 758–72

McGarry M, Li R, Apostolakis I, Nauleau P and Konofagou E E 2016 An inverse approach to determining spatially varying arterial compliance using ultrasound imaging *Phys. Med. Biol.* **61** 5486–507

Mitra M and Gopalakrishnan S 2016 Guided wave based structural health monitoring: A review *Smart Mater. Struct.* **25**

Mitri F G, Urban M W, Fatemi M and Greenleaf J F 2011 Shear wave dispersion ultrasonic vibrometry for measuring prostate shear stiffness and viscosity: An in vitro pilot study *IEEE Trans. Biomed. Eng.* **58** 235–42

Mookerjee A, Al-Jumaily A M and Lowe A 2010 Arterial pulse wave velocity measurement: Different techniques, similar results-implications for medical devices *Biomech. Model. Mechanobiol.* **9** 773–81

Nelson R B, Dong S B and Kalra R D 1971 Vibrations and waves in laminated orthotropic circular cylinders *J. Sound Vib.* **18** 429–44

Nenadic I, Urban M, Greenleaf J, Gennisson J L, Bernal M and Tanter M 2018 *Ultrasound Elastography for Biomedical Applications and Medicine* ed I Nenadic, M Urban, J Greenleaf, J-L Gennisson, M Bernal and M Tanter (Chichester, UK: John Wiley & Sons, Ltd)

Nenadic I Z, Qiang B, Urban M W, De Araujo Vasconcelo L H, Nabavizadeh A, Alizad A, Greenleaf J F and Fatemi M 2013 Ultrasound bladder vibrometry method for measuring viscoelasticity of the bladder wall *Phys. Med. Biol.* **58** 2675–95

Nenadic I Z, Qiang B, Urban M W, Zhao H, Sanchez W, Greenleaf J F and Chen S 2017 Attenuation measuring ultrasound shearwave elastography and in vivo application in post-transplant liver patients *Phys. Med. Biol.* **62** 484–500

Nenadic I Z, Urban M W, Pislaru C, Bernal M and Greenleaf J F 2011 In vivo open and closed chest measurements of myocardial viscoelasticity through a heart cycle using Lamb wave Dispersion Ultrasound Vibrometry (LDUV) *IEEE International Ultrasonics Symposium, IUS* pp 17–20

Nguyen T M, Aubry J F, Touboul D, Fink M, Gennisson J L, Bercoff J and Tanter M 2012 Monitoring of cornea elastic properties changes during UV-A/riboflavin-induced corneal collagen cross-linking using supersonic shear wave imaging: A pilot study *Investig. Ophthalmol. Vis. Sci.* **53** 5948–54

Nguyen T M, Couade M, Bercoff J and Tanter M 2011 Assessment of viscous and elastic properties of sub-wavelength layered soft tissues using shear wave spectroscopy: Theoretical framework and in vitro experimental validation *IEEE Trans. Ultrason. Ferroelectr. Freq. Control* **58** 2305–15

Oliver J J and Webb D J 2003 Noninvasive assessment of arterial stiffness and risk of atherosclerotic events. *Arterioscler. Thromb. Vasc. Biol.* **23** 554–66

Paini A, Boutouyrie P, Calvet D, Tropeano A-I, Laloux B and Laurent S 2006 Carotid and aortic stiffness: determinants of discrepancies. *Hypertens. (Dallas, Tex. 1979)* **47** 371–6

Palombo C and Kozakova M 2016 Arterial stiffness, atherosclerosis and cardiovascular risk: Pathophysiologic mechanisms and emerging clinical indications *Vascul. Pharmacol.* **77** 1–7

Parameswaran P K, Dai D, Ding Y H, Urban M W, Manlove L, Sathish V, Cebral J R, Kallmes D F and Kadirvel R 2019 Downstream vascular changes after flow-diverting device deployment in a rabbit model *J. Neurointerv. Surg.* **11** 523–7

Pislaru C, Urban M W, Pislaru S V., Kinnick R R and Greenleaf J F 2014 Viscoelastic properties of normal and infarcted myocardium measured by a multifrequency shear wave method: Comparison with pressure-segment length method *Ultrasound Med. Biol.* **40** 1785–95

Pruijssen J T, de Korte C L, Voss I and Hansen H H G 2020 Vascular Shear Wave Elastography

in Atherosclerotic Arteries: A Systematic Review *Ultrasound Med. Biol.* **46** 2145–63

Randall M J 1967 *FAST PROGRAMS FOR LAYERED HALF-SPACE PROBLEMS* vol 57

Rose J L 2011 The upcoming revolution in ultrasonic guided waves *SPIE 7983, Nondestructive Characterization for Composite Materials, Aerospace Engineering, Civil Infrastructure, and Homeland Security* p 31

Rose J L 2014 *Ultrasonic Guided Waves in Solid Media* (Cambridge University Press)

Roy T and Guddati M N 2021 Shear wave dispersion analysis of incompressible waveguides *J. Acoust. Soc. Am.* **149** 972–82

Roy T, Urban M W, Xu Y, Greenleaf J F and Guddati M N 2021 Multimodal guided wave inversion for arterial stiffness: methodology and validation in phantoms *Phys. Med. Biol.* **66** 115020

Saltelli A, Ratto M, Andres T, Campolongo F, Cariboni J, Gatelli D, Saisana M and Tarantola S 2007 *Global Sensitivity Analysis. The Primer* (Chichester, UK: John Wiley & Sons, Ltd)

Sarvazyan A, J. Hall T, W. Urban M, Fatemi M, R. Aglyamov S and S. Garra B 2011 An Overview of Elastography-An Emerging Branch of Medical Imaging *Curr. Med. Imaging Rev.* **7** 255–82

Sarvazyan A P, Urban M W and Greenleaf J F 2013 Acoustic Waves in Medical Imaging and Diagnostics *Ultrasound Med. Biol.* **39** 1133–46

Sato H and Ogiso H 2013 Analytical method for guided waves propagating in a fluid-filled pipe with attenuation *Jpn. J. Appl. Phys.* **52** 7

Savadatti S and Guddati M N 2010a A finite element alternative to infinite elements *Comput. Methods Appl. Mech. Eng.* **199** 2204–23

Savadatti S and Guddati M N 2010b Absorbing boundary conditions for scalar waves in anisotropic media. Part 1: Time harmonic modeling *J. Comput. Phys.* **229** 6696–714

Segers P, Rietzschel E R and Chirinos J A 2020 How to Measure Arterial Stiffness in Humans *Arterioscler. Thromb. Vasc. Biol.* **40** 1034–43

Shcherbakova D A, Debusschere N, Caenen A, Iannaccone F, Pernot M, Swillens A and Segers P 2017 A finite element model to study the effect of tissue anisotropy on ex vivo arterial shear wave elastography measurements *Phys. Med. Biol.* **62** 5245–75

Shcherbakova D A, Papadacci C, Swillens A, Caenen A, De Bock S, Saey V, Chiers K, Tanter M, Greenwald S E, Pernot M and Segers P 2014 Supersonic Shear Wave Imaging to Assess

Arterial Nonlinear Behavior and Anisotropy: Proof of Principle via *Ex Vivo* Testing of the Horse Aorta *Adv. Mech. Eng.* **6** 272586

Smith R C 2014 *Uncertainty quantification : theory, implementation, and applications* (SIAM, Philadelphia, PA)

Su Z, Ye L and Lu Y 2006 Guided Lamb waves for identification of damage in composite structures: A review *J. Sound Vib.* **295** 753–80

Sun Z 2015 Aging, arterial stiffness, and hypertension *Hypertension* **65** 252–6

Sutton-Tyrrell K, Najjar S S, Boudreau R M, Venkitachalam L, Kupelian V, Simonsick E M, Havlik R, Lakatta E G, Spurgeon H, Kritchevsky S, Pahor M, Bauer D, Newman A and Health ABC Study 2005 Elevated aortic pulse wave velocity, a marker of arterial stiffness, predicts cardiovascular events in well-functioning older adults. *Circulation* **111** 3384–90

Tanter M, Touboul D, Gennisson J L, Bercoff J and Fink M 2009 High-resolution quantitative imaging of cornea elasticity using supersonic shear imaging *IEEE Trans. Med. Imaging* **28** 1881–93

Tassoulas J L and Kausel E 1983 Elements for the numerical analysis of wave motion in layered strata *Int. J. Numer. Methods Eng.* **19** 1005–32

Taweel H, Dong S B and Kazic M 2000 Wave reflection from the free end of a cylinder with an arbitrary cross-section *Int. J. Solids Struct.* **37** 1701–26

Thomson W T 1950 Transmission of elastic waves through a stratified solid medium *J. Appl. Phys.* **21** 89–93

Tran T N H T, Nguyen K C T, Sacchi M D and Le L H 2014 Imaging Ultrasonic Dispersive Guided Wave Energy in Long Bones Using Linear Radon Transform *Ultrasound Med. Biol.* **40** 2715–27

Urban M W, Pislaru C, Nenadic I Z, Kinnick R R and Greenleaf J F 2013 Measurement of viscoelastic properties of in vivo swine myocardium using Lamb Wave Dispersion Ultrasound Vibrometry (LDUV) *IEEE Trans. Med. Imaging* **32** 247–61

Vappou J, Luo J and Konofagou E E 2010 Pulse Wave Imaging for Noninvasive and Quantitative Measurement of Arterial Stiffness In Vivo *Am. J. Hypertens.* **23** 393–8

Vaziri Astaneh A and Guddati M N 2016 Improved inversion algorithms for near-surface characterization *Geophys. J. Int.* **206** 1410–23

Vaziri Astaneh A and Guddati M 2017a Dispersion analysis software for immersed and

embedded waveguides Online: http://wavedisp.com

Vaziri Astaneh A and Guddati M N 2017b Dispersion analysis of composite acousto-elastic waveguides *Compos. Part B Eng.* **130** 200–16

Vaziri Astaneh A and Guddati M N 2016 Efficient computation of dispersion curves for multilayered waveguides and half-spaces *Comput. Methods Appl. Mech. Eng.* **300** 27–46

Vlachopoulos C, Aznaouridis K and Stefanadis C 2010 Prediction of Cardiovascular Events and All-Cause Mortality With Arterial Stiffness. A Systematic Review and Meta-Analysis *J. Am. Coll. Cardiol.* **55** 1318–27

Waltz R A, Morales J L, Nocedal · J and Orban · D 2006 An interior algorithm for nonlinear optimization that combines line search and trust region steps *Math. Program., Ser. A* **107** 391–408

Wang Y and Lee W-N 2020 Non-invasive Estimation of Localized Dynamic Luminal Pressure Change by Ultrasound Elastography in Arteries with Normal and Abnormal Geometries *IEEE Trans. Biomed. Eng.* **9294** 1–1

Widman E, Maksuti E, Amador C, Urban M W, Caidahl K and Larsson M 2016 Shear Wave Elastography Quantifies Stiffness in Ex Vivo Porcine Artery with Stiffened Arterial Region *Ultrasound Med. Biol.* **42** 2423–35

Widman E, Maksuti E, Larsson D, Urban M W, Bjällmark A and Larsson M 2015 Shear wave elastography plaque characterization with mechanical testing validation: A phantom study *Phys. Med. Biol.* **60** 3151–74

Willberg C, Duczek S, Vivar-Perez J M and Ahmad Z A B 2015 Simulation Methods for Guided Wave-Based Structural Health Monitoring: A Review *Appl. Mech. Rev.* **67(1)** 20

Yeh C L, Kuo P L, Gennisson J L, Brum J, Tanter M and Li P C 2016 Shear Wave Measurements for Evaluation of Tendon Diseases *IEEE Trans. Ultrason. Ferroelectr. Freq. Control* **63** 1906–21

Zhang X, Kinnick R R, Fatemi M and Greenleaf J F 2005 Noninvasive method for estimation of complex elastic modulus of arterial vessels *IEEE Trans. Ultrason. Ferroelectr. Freq. Control* **52** 642–51